In-Source Laser Resonance Ionization at ISOL Facilities

A thesis submitted to the University of Manchester for the degree of Doctor of Philosophy in the Faculty of Science and Engineering

2007

Bruce A. Marsh

School of Physics and Astronomy

Contents

List of Figures

LIST OF FIGURES

Abstract

Resonance ionization laser ion source development has been carried out at two radioactive ion beam facilities: ISOLDE (CERN, Switzerland) and the IGISOL facility (Jyväskylä, Finland). The scope of the Resonance Ionization Laser Ion Source has been extended to 27 elements with the development of new three-step ionization schemes for Sb, Sc, Dy, Y and Au. The efficiencies were determined to be in the range of 2 - 20 %. Additionally, a new two-step ionization scheme has been developed for bismuth in an off-line atomic beam unit. The scheme relies on ionization via a strong and broad auto-ionizing resonance at an energy of 63196.79 cm^{-1}. This scheme may offer an improvement over the existing RILIS efficiency and will be more convenient for use during resonance ionization spectroscopy of Bi isotopes.

The RILIS can be used as a spectroscopic tool to probe features such as the hyperfine structures and the isotope-shifts of radioisotopes with low production rates. By coupling a laser scanning process that directly influences the initial ion creation with a detection method involving a nuclear tag, such as alpha or gamma emission, an extremely high degree of sensitivity has been achieved. A recent ^{104}Ag ground-state and isomer measurement is presented and is an example of RILIS spectroscopy combined with gamma detection. This measurement clarifies an unusual feature observed in the hyperfine spectra during a previous study of this isotope.

Recent technical improvements in the ISOLDE RILIS selectivity, laser operation and data acquisition have improved this spectroscopic technique. A description of the experimental methods and the first results of a study of the alpha emitting neutron-deficient ^{189,191}Bi isotopes by simultaneous atomic and nuclear spectroscopy are presented.

Concerning the compatibility of the IGISOL front end with the new FURIOS laser ion source, the gas flow dynamics outside the gas cell have been investigated off-line, leading to an adaptation of the radio frequency sextupole ion guide which forms the laser/atom interaction region. The outcome of initial testing of this device is discussed.

Declaration

No portion of the work referred to in this thesis has been submitted in support of an application for another degree or qualification of this or any other university or other institute of learning.

Notes on copyright and the ownership of intellectual property rights

1. Copyright in text of this thesis rests with the Author. Copies (by any process) either in full, or of extracts, may be made **only** in accordance with instructions given by the Author and lodged in the John Rylands University Library of Manchester. Details may be obtained from the Librarian. This page must form part of any such copies made. Further copies (by any process) of copies made in accordance with such instructions may not be made without the permission (in writing) of the Author.
2. The ownership of any intellectual property rights which may be described in this thesis is vested in the University of Manchester, subject to any prior agreement to the contrary, and may not be made available for use by third parties without the written permission of the University, which will prescribe the terms and conditions of any such agreement.

Further information on the conditions under which disclosures and exploitation may take place is available from the Head of the Department of Physics and Astronomy.

Acknowledgements

My time spent as a PhD student in the Nuclear Physics Group at Manchester University has been extremely eventful, rewarding and overall, a very enjoyable period of my life. I have many people to thank for this but primarily I am grateful to Jon Billowes for taking me on as a member of the group and for his encouragement and help. His relentless creation of plans and concepts has made the last four years continually challenging and exciting. I must also thank Paul Campbell for being a very patient and approachable source of information and advice, and also for his regular demonstrations of the latest in high tech gadgetry. It has been a pleasure to work with the other members of Manchester laser spectroscopy collaboration: Ayad, Ben, Bradley, Ernesto, Kieran, Mahmoud and Tania. My extended visits to work at Jyväskylä's IGISOL facility have been unforgettable. Thanks to Juha and Matti for being so welcoming and helpful. I greatly appreciated the supervision of Arto and Iain, both in the lab and on the ice skating track.

Working at ISOLDE RILIS, I have had the pleasure to get to know a huge range of experimentalists from all areas of RIB related research and have greatly enjoyed the diversity and interactions with them on the countless shifts we have endured together! I really appreciate the huge amount of help and advice that has been so readily offered by Valentin Fedosseev as my supervisor at ISOLDE. It has been great getting to know the growing list of RILIS team mates: Elisabeth, Sasha, Victor, Pallav, Ernesto, Yuri, Maxim, Dima, Sergei, Thomas and Fabian and I look forward to continuing working with Valentin and the rest of the RILIS and the ISOLDE collaboration as a new phase in the development of RILIS begins.

Finally, I want to thank my family and friends who have been affected to various degrees by the unusual time schedules, awkward travel and living arrangements and my slightly traumatic Finland incident that were all side effects of the last four years work.

And, here it is in writing: Sophie, I promise to start doing the washing up once this is handed in.

Chapter 1

Introduction

The field of nuclear physics emerged at the start of the last century with Ernest Rutherford's theories about the nature of the atomic nucleus. Strong evidence for Rutherford's 'solar system' model of the atom was provided by the experiments in Manchester of his post-doctoral researcher, Hans Geiger [1] and one of his undergraduate students, Ernest Marsden. They studied the motion of alpha particles impinging on a gold foil and observed an influence on the trajectory of only a small proportion of the particles, and for these scattered particles, the scattering angle was large. The alpha particles were acting as if they were incident upon an array of small, dense and widely spaced impenetrable objects, the atomic nuclei.

For the next 50 years, progress in this field was rapid: Rutherford's transmutation of nitrogen to oxygen [2], Dirac's prediction of antimatter [3], Chadwick's observation of the neutron [4] and Frederic Joliot and Irene Curie's production of the world's first artificial radioactive isotope, phosphorus-30 [5], all occurring before 1940. For the next two decades, the use of atomic nuclei as a power source dominated nuclear research but with building of nuclear reactors came the widespread availability of previously unseen, artificially produced exotic nuclei. The production and separation of these radioactive isotopes became key to the study of fundamental nuclear properties such as masses, half lives, and decay schemes. Due to their unstable nature, the scope for study of radio-nuclides is limited by their transport time to an experimental setup. During the 1960s, this problem was addressed with the development of methods to couple the production and

transport of the nuclides within a single piece of apparatus, now known as an isotope separator facility.

Radioactive Ion Beam (RIB) facilities aim to achieve almost immediate transport and isotope separation of nuclear reaction products and therefore enable the detection and study of short-lived isotopes. With the use of these facilities, the nuclear chart has been extended further toward the proton and neutron drip lines and now includes over 3000 isotopes. Furthermore, by supplying isotopes as an energetic beam, the applications of RIB facilities have extended beyond the study of nuclear properties and into related fields such as fundamental interactions and nuclear astrophysics. Today, state of the art RIB facilities are distinguishable by their ability to provide a very high level of selectivity and produce clean beams of a chosen isotope or isomer. One of the most significant developments in this respect was the implementation of the Laser Ion Source. Through the process of step-wise resonance photo-ionization, laser ion sources exploit the uniqueness of the electronic energy level structure of an element to provide an extremely selective means of ionization of reaction products. The improvement of beam purity has drastically increased the scope of application of RIBs, generating interest from fields such as solid-state physics, life sciences and materials science.

This thesis presents work carried out at two facilities which are at the forefront of research using radioactive ion beams: the ISOLDE facility at CERN, Geneva, and the IGISOL facility at JYFL, Jyväskylä, Finland. Some discussion of the facilities themselves will follow but suffice to say, these two facilities have been somewhat pioneering in their field, with each adopting their own highly successful, and respectively highly complementary approach to RIB production.

In discussing work carried out as part of the development of the laser ion sources at these facilities, this thesis presents the key considerations and requirements for laser ion sources in general and also illustrates the specific challenges and requirements presented by these two contrasting facilities.

At the ISOLDE facility, where the Resonance Ionization Laser Ion Source (RILIS) had been in operation since 1992 [6], the focus of recent work has been the improvement of performance and scope of the system. Specifically, details of new ionization schemes for scandium, antimony, yttrium, dysprosium, mercury

and gold are presented here. At Jyväskylä's IGISOL facility, their Fast Universal Resonance Ion Source (FURIOS) is a new project, only recently constructed. Within the scope of this thesis, development work reported for FURIOS is on a more fundamental level and brings into discussion the choice of the laser system itself, the optimization of the laser interaction region and the delivery of radioactive atoms to this interaction region.

In the field of atomic spectroscopy, precision measurements of electronic energy level structures can resolve features such as the isotope-shift and hyperfine structure. An understanding of these small effects as a consequence of the interactions between the atomic nucleus and the orbiting electrons has enabled the extraction of nuclear properties (size, shape, spin and moments). The use of tunable laser light revolutionized this type of measurement and, combined with the fast delivery of exotic nuclei in the form of an ion beam, the potential for this research has extended to the far reaches of the nuclear chart. Nuclear properties of hundreds of isotopes across the nuclear chart have been measured by laser spectroscopy. These measurements are the product of a plethora of experimental techniques and innovations at many facilities worldwide [7].

Resonance Ionization Spectroscopy (RIS) is regarded as one of the most sensitive of these techniques as it involves detection of the ion itself, either directly, or via its characteristic radiative decay. RIS studies require the sample in atomic form, and since the process results in the creation of singly-charged ions, the laser ion source is an ideal tool for this purpose. In-source RIS was first demonstrated by Vladilen Letokhov and colleagues at PNPI, St Petersburg [8]. The ISOLDE RILIS was established in close collaboration with this group and as such, its power as a spectroscopic tool was anticipated. Not long after its installation, the first RILIS in-source RIS study was performed [9]. The importance of this technique as a probe of nuclear parameters, and also as a means of carrying out nuclear isomer separation will be discussed in detail. A measurement of the hyperfine structure of the ^{104}Ag ground-state and isomer is presented as an example of in-source RIS combined with gamma spectroscopy.

To meet the demands of the ISOLDE experiment number IS407: *'Study of the neutron-deficient Pb and Bi isotopes by simultaneous atomic and nuclear spectroscopy'*, the RILIS RIS technique has been subject to some refinement and to

date the IS407 collaboration has had two successful experimental beam-time periods, both taking place during the course of this PhD program. With its high inherent sensitivity, and the favorable ISOLDE yields in the region of interest, measurements have been made over 20 isotopes from the line of stability into the neutron-deficient region. Of these, the isotope-shift and hyperfine structure measurements of ^{189,191}Bi will be discussed.

Chapter 2

Radioactive Ion Beam Facilities

2.1 Introduction

The various RIB facilities operating around the globe all share strong similarities. However the design and construction of such a facility is by no means standardized, with each new facility bringing varying degrees of innovation. An overview of the current status and diversity of these facilities is provided in reference [10] and, in general, they fall into one of two categories: Isotope Separator On-Line (ISOL) and In-Flight Fragment Separators. Common to all RIB facilities is the need for a primary (driver) projectile beam and a target. What separates them in to one of the two categories is their method of beam preparation in terms of radionuclide extraction, isotope separation and acceleration. In-flight facilities rely on the fragmentation of a heavy projectile as it is incident on a thin target. The projectile fragments continue on with a largely unperturbed forward velocity and enter the mass separator directly. A thorough description of projectile fragmentation facilities can be found in [11], along with a summary of the typical yields that can be obtained. The use of a thin target and the large diversity of reaction products mean that the total beam flux at such facilities is often lower than can be achieved at ISOL facilities. On the other hand, on account of the immediate extraction of reaction products, the yield of very exotic or short-lived species can be many orders-of-magnitude greater and the high beam energy gives immediate compatibility with some colliding beam experiments or storage ring

systems. Additionally, the nature of the extraction process removes any chemical dependance, enabling the production of RIBs of even the most refractory elements.

At ISOL facilities, a slower and more modular approach is adopted for RIB production. Reaction products are stopped at, or close to the point of creation, ionized in an ion source, accelerated and then mass separated. The result is a clean, low emittance beam which is easy to manipulate. The work described in this thesis was carried out at two very different but complimentary ISOL facilities, the JYFL IGISOL and the CERN ISOLDE facility.

The operating principles of these two facilities are described briefly here.

2.2 The Isotope Separator On-line

As the name suggests, ISOL facilities add a degree of selectivity to the radionuclide production and transport processes and do this by exploiting the charge-to-mass ratio of differences between isotopes during their flight to the experimental set-up.

The preparation of an ISOL beam takes place under high vacuum conditions, typically 10^{-7} Torr and is comprised of the following key stages: *production, ionization, extraction* and *mass separation.*

For any ISOL facility, the combined efficiency of these key stages is both element and isotope dependent. Chemical properties influence the delivery of the reaction product to the ion source, the ionization process itself, and the ion survival/extraction efficiency whilst, for radioactive isotopes, decay losses are incurred during each stage of their delivery to the experimental set-up.

A common example of the production stage is an energetic proton beam incident on a uranium target. With the occurrence of spallation, fragmentation and fission, this production process is fairly non-selective and a wide spectrum of isotopes is typically produced. Extraction of the reaction products relies on electrostatic acceleration, hence the need for an ionization stage. The efficiency of the isotope-separation stage relies on the availability of the reaction products in a single charge state (usually 1^+).

The lifetime of the radio-nuclides produced is not the only limiting factor on the feasibility of their extraction for experimental study. Chemical properties such as reactivity and vapour pressure play a role and, for some elements, a degree of ingenuity is required to ensure their delivery.

The remainder of this chapter discusses the details of the two ISOL facilities at which the work presented in this thesis was carried out.

2.3 ISOLDE at CERN

At ISOLDE isotopes are produced by fission, fragmentation or spallation reactions which occur when high energy (1.4 GeV) protons are incident upon a thick target. Generally speaking, for a given reaction channel, the production rate is proportional both to the primary beam flux and the number of target atoms within this beam and so ISOLDE's thick target can be advantageous and enable high yields to be produced. In practice, the reaction rate varies across the target material as a function of primary beam attenuation and isotope production by secondary reactions also plays an important role. The production cross section for secondary neutrons is particularly high and since neutrons are able to penetrate further into the target matrix than primary reaction products or charged particles, a significant portion of the isotope yield comes from neutron induced reactions. The high production cross section for neutrons can be exploited through the use of a neutron convertor target. Here the primary beam is directed onto a tantalum rod adjacent to the ISOLDE target. In this configuration, isotopes are produced in the target as a result of reactions induced by the neutrons emitted from the convertor. This greatly enhances the fission cross section relative to spallation or fragmentation, hence introducing an increased level of selectivity at the production stage. The reaction products emerge from the target material as an atomic vapour. This diffusion and effusion process is relatively slow and as such, a thick target can be become prohibitive for the release of very short-lived nuclei ($<$0.1 s). The study and optimization of ISOL target production rates and yields forms the foundation of the EU-funded TARGISOL project [12].

2.3.1 The CERN Proton Synchrotron Booster

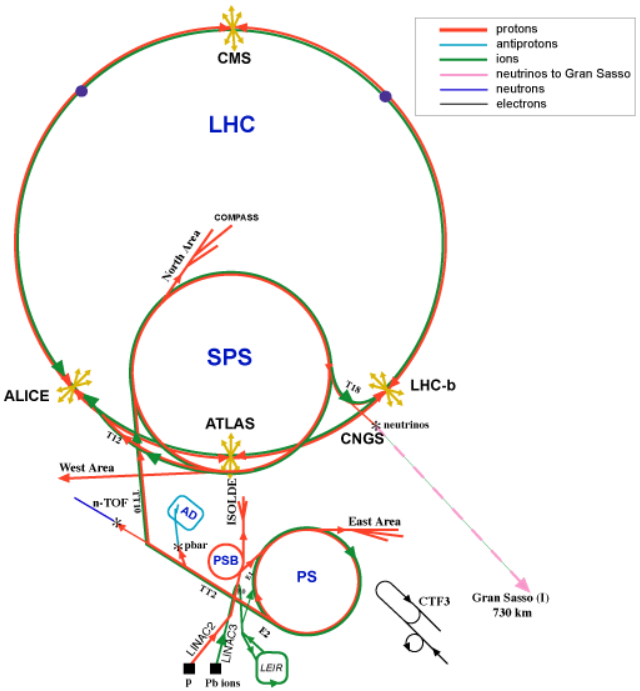

Figure 2.1: CERN's accelerators.

The projectile beam for the ISOLDE targets is provided by the CERN PS Booster (PSB) which is a 50 m diameter proton synchrotron accelerator. 50 MeV protons are injected into the PSB from CERN's LINAC 2. Protons are accelerated to an energy of 1.0 or 1.4 GeV in the PSB and are released as ~2.4 μs pulses with an intensity of up to 3×10^{13} protons per pulse. Typically 12 proton pulses form CERN's 16.8 s accelerator super-cycle (one pulse every 1.2 s) and ISOLDE shares these pulses with other CERN facilities, receiving typically 5-10 pulses per super-cycle. Figure 2.1 shows the location of the PSB within the CERN accelerator network.

2.3.2 The target

For any given isotope, the production rate in the target is the product of the projectile beam flux, the quantity of target particles within the path of the projectile

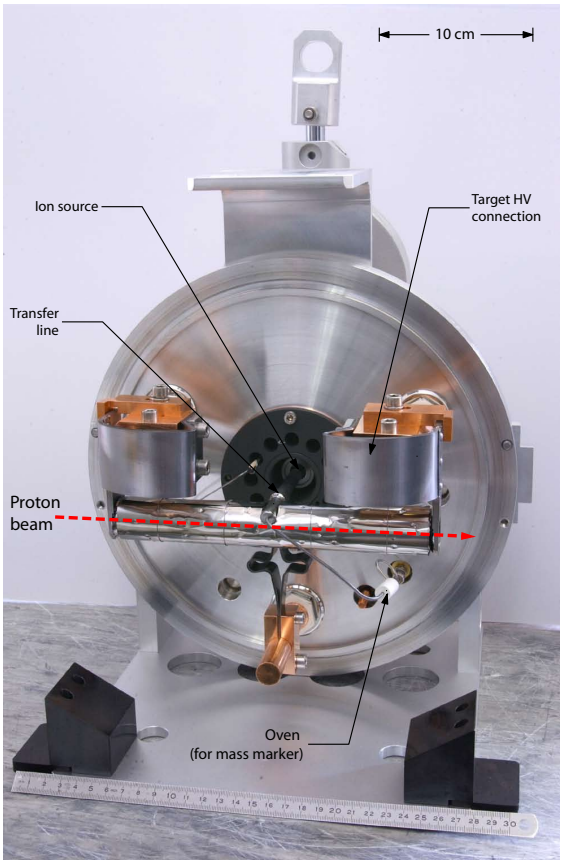

Figure 2.2: An ISOLDE target ion source unit.

beam, and the production cross section for the isotope. Many different targets have been developed for use at ISOLDE in order to maximize these parameters for isotopes of interest. As such, the choice of target specification (material, thickness, geometry) provides the first stage of selectivity in the production of the RIB.

The transport of the reaction products from the target by diffusion and effusion is both a chemical and a temperature dependent processes. Losses are incurred due to poor release from the target material itself, wall sticking within the target container and the transfer line or radioactive decay of the isotope of interest. By heating the target and transfer line to around 2300 K the wall sticking

and diffusion and effusion times are reduced.

More than ten ion-source and target combinations are commonly used at ISOLDE and close to 20 targets are used each year. A typical target unit with its integral hot cavity surface ion source is shown in Figure 2.2.

The target and ion source are held at a potential of 60 kV which is used to accelerate ions upon creation along the beamline towards the mass separator. The front end high voltage is operated in a pulsed mode, asynchronous with the proton pulse arrival. This precaution is necessary to avoid sparking that could otherwise be triggered by ionization of the air through which the proton beam travels before entering the target unit.

2.3.3 Ionization and isotope separation

Isotope separation of the ionized reaction products is done by sending the ion beam into a mass separator. This mass selection does not distinguish between isobars of different elements and a large background of unwanted isobaric contaminants can be prohibitive for the study of certain atomic species and in particular low-yield exotic isotopes. During the ionization process it is possible to exploit the chemical or physical properties of either the element of interest or the likely isobaric contaminants to provide a purer beam after mass separation. The three ionization processes used at ISOLDE are described in the following subsections.

2.3.3.1 The surface ion source

Surface ionization can occur when an atom comes into contact with a hot metal surface. The process of positive surface ionization, the transfer of a valence electron from the atom to the metal surface is energetically favorable for elements with an ionization potential lower than the work function of the metal. At a temperature T, the probability of ionization, $\frac{X^+}{X^0}$, due to collision with the metal surface is given by the Langmuir equation [13],

$$\frac{X^+}{X^0} = \frac{g^+}{g^0} e^{-\frac{\Psi - W_i}{kT}}. \tag{2.1}$$

Ψ is the work function of the metal, W_i is the ionization potential of the atom and k is Boltzmann's constant. g^0 and g^+ are the statistical weights (2J+1) of the atomic and first ionic ground-states.

At ISOLDE the surface ion source is a metal tube which is the only outlet for the reaction products from the target. In this long, narrow cavity it has been observed that the actual ionization efficiency can be far greater than that predicted by Equation 2.1. Electrons emitted from the hot metal surface give rise to a space-charge potential in the cavity. A neutral plasma is maintained by the production of surface ions at the cavity walls. In the hot cavity the Langmuir equation still holds for the probability of surface ionization in the event of an atom-wall collision but a prediction of the actual ionization efficiency must now take into account this plasma effect. The Saha Equation 2.2, derived by Saha in 1924 [14] to describe the degree of ionization in the solar chromosphere is a better representation of the actual degree of ionization. The Saha equation is given by

$$\frac{X^+}{X^0} = \frac{2g^+}{g^0}\left(\frac{2\pi m}{h^2}\right)^{\frac{3}{2}}\frac{1}{p}(kT)^{\frac{5}{2}}e^{-\frac{W_i}{kT}} \tag{2.2}$$

where p is the pressure in the cavity and m is the atomic mass. In the hot cavity the ionization efficiency is not dependent on the work function of the metal provided that the work function is greater than the ionization potential of the element: a metal with lower work function emits more thermionic electrons into the cavity; the effect of the lower ionization efficiency for atom/wall collisions is suppressed by the higher plasma potential which reduces the probability of ions neutralizing by further wall collisions. For alkalis and some rare earth elements high ionization efficiencies can be achieved. The range of elements that are ionized is limited by the work function of the metal used and hence some degree of chemical selectivity can be achieved by the selection of a cavity material with a low work function.

2.3.3.2 The plasma ion source

Electron impact ionization is capable of ionizing any element provided the incident electron energy is in excess of the ionization potential of the atom. ISOLDE uses a Forced Electron Beam Arc Discharge (FEBIAD) type plasma ion source.

Electrons emitted from a hot cathode are accelerated into a plasma chamber approximately 1 cm^3 in volume. With electron impact energies of between 100 and 200 eV, elements with very high ionization potentials are efficiently ionized. In fact, the FEBIAD can also be used for the production of multi-charged ions. Although advantageous if some post acceleration of the ion beam is intended, the production of multi-charged ions at the ISOLDE ion source can make it difficult to obtain pure beams at a given mass from the separator magnets. The limited selectivity offered by this process can be improved by exploiting the chemical or physical properties of the atoms as they are released from the target. Molecule formation, for instance, can greatly improve the probability of release for some refractory elements. This has been demonstrated for hafnium, where fluoridation of the target resulted in the release of HfF_2. The use of a plasma ion source ensured efficient dissociation of the molecule and the production of an Hf^+ beam [15].

2.3.3.3 Resonance Ionization Laser Ion Source

Many experimental efforts at ISOLDE have been hampered by the presence of a large isobaric background within the ion beam emerging from the ISOLDE separators [16]. This background stems from a combined effect of the diversity of isotope production within the target and the subsequent universal nature of standard ionization techniques. This issue was the motivation for the development of an ionization process that will distinguish between chemical species, complementing the mass separation stage to provide isotopic beam purity.

Using tunable lasers it is possible to match the photon energy of the laser light to an electronic transition of a particular element. If this light is incident on an atomic vapour of many atomic species, photons will be resonantly absorbed by an electron occupying a suitable energy level. The precision with which the photon energy is defined determines the degree of element dependence on this absorption. If the photon flux is sufficient and a series of laser frequencies are used (each precisely tuned so that the respective photon energies match transitions between successive electron energy levels within a particular atomic species), the valence electron will be promoted through the energy level structure towards

the ionization potential. Since, for each element the energy level structure is discernibly different, the step-wise resonant nature of the process ensures a high degree of Z-selectivity. If the valence electron of the selected element is excited to an energy level close to the ionization potential, its ionization by electric fields, atomic collisions or in the presence of an additional laser beam is vastly enhanced. This is illustrated in Figure 2.3.

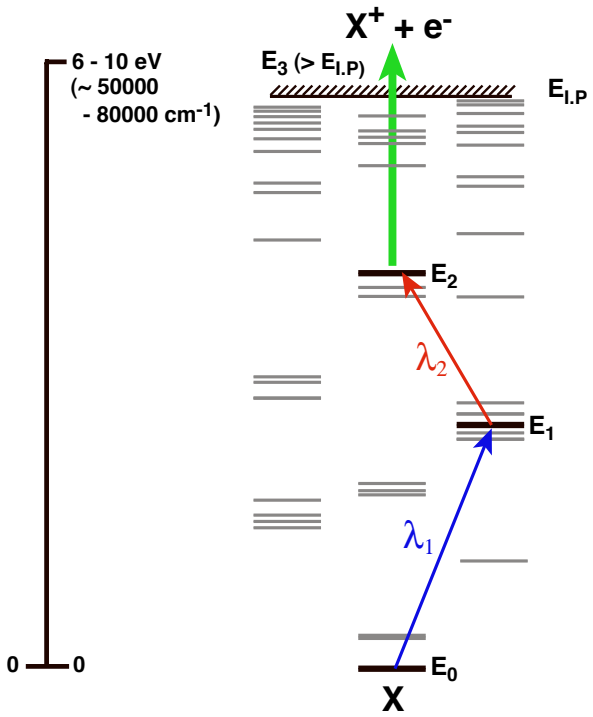

Figure 2.3: Step-wise laser resonance ionization using two resonant photon absorption steps followed by a non-resonant photon absorption ionization stage.

The Resonance Ionization Laser Ion Source (RILIS) is based upon this principle of step-wise photo-ionization, which is described in detail by Lethokov [17]. The technical details for RILIS itself are given in [6]. The ionization efficiency is heavily reliant on the saturation of the resonant photon absorption steps and the compatibility of the laser system with the physical parameters of the atomic sample released from the target. The laser beams are directed through a window in the ion beam-line at the mass separator and focussed into the cavity of a standard surface ion source. Figure 2.4 compares the measured efficiencies of the

various ion sources, showing that the typically achieved RILIS efficiencies of 5 – 10% are good compared to those of other ionization methods. What sets RILIS apart is its unrivaled level of selectivity. Further details of RILIS are given in Chapter 5.

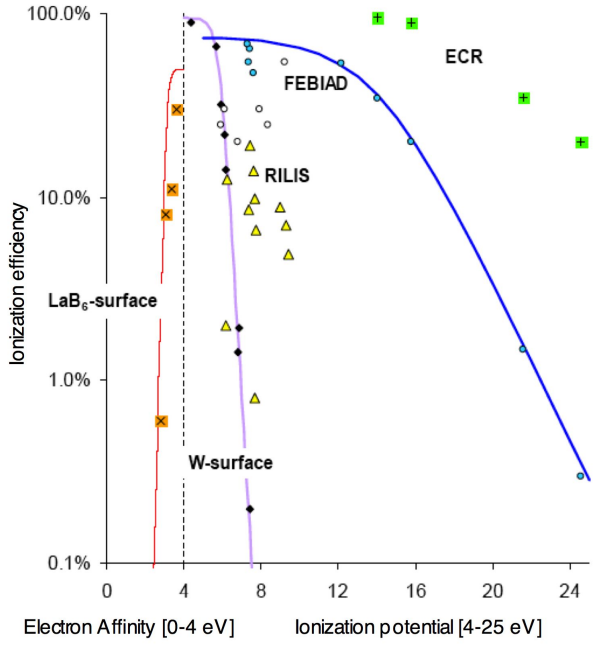

Figure 2.4: ISOLDE ion source efficiencies.

2.4 The IGISOL facility at Jyväskylä

A detailed overview of the IGISOL facility is given by J. Äysto [18]. The IGISOL front end with a typical gas cell is shown in Figure 2.5. In standard operation, where reaction products are required in a 1^+ charge state, helium gas at a pressure of typically 200 mbar is extracted through the nozzle at a rate of > 0.1 l/s by differential pumping, carrying singly-charged reaction products to the skimmer electrode.

The IGISOL relies on an alternative method for the production of radioactive ion beams. A thin target, placed inside a high pressure gas cell, is bombarded by a light ion (p, d, ^{3}He, ^{4}He) beam from the cyclotron accelerator and the

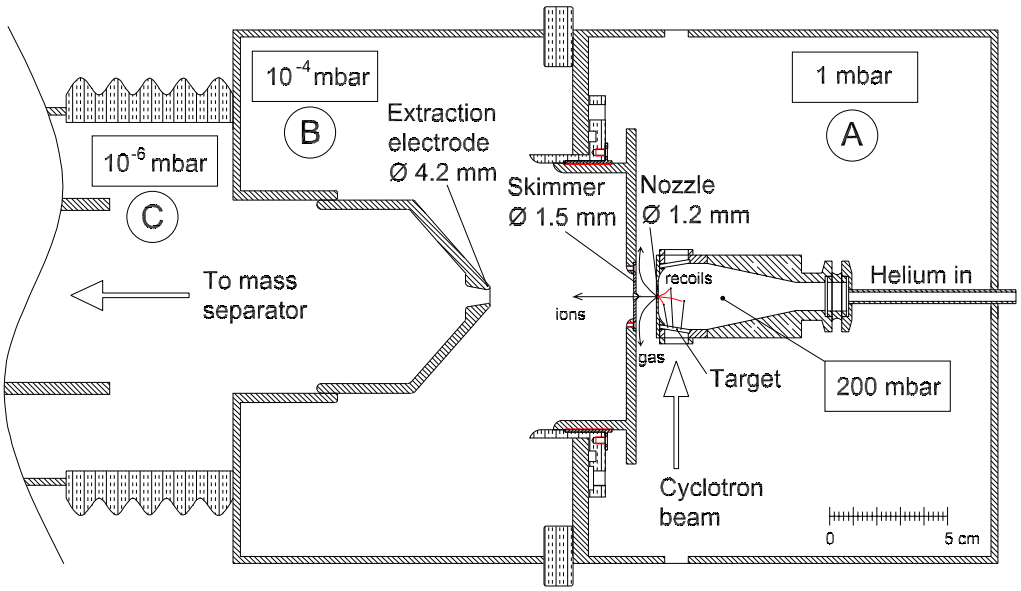

Figure 2.5: Schematic of the IGISOL front end.

recoiling reaction products are stopped in the gas cell. A high proportion of these exist as singly-charged ions as the gas flow transports them in to the lower pressure environment outside the gas cell where they are accelerated towards the mass separator by a 40 kV potential. A detailed description of this technique is given in Reference [19]. The thin target, and hence elimination of the slow diffusion stage required at the ISOLDE facility, make the IGISOL a fast ($\sim$ 1 ms) and chemically blind process capable of producing ion beams of even the most refractory elements.

As with many of the ion sources used at ISOLDE, the ion-production method employed at the IGISOL is not element selective and the subsequent magnetic mass selection stage does not guarantee pure beams of a chosen isobar. The thin target and lower projectile beam intensity means that the total production yield is often three or four orders-of-magnitude lower than can be achieved at ISOLDE. A greater flexibility in terms of projectile and target selection often compensates for this by allowing a particular reaction channel to be targeted, e.g (p, xn).

In the standard IGISOL operation, the vacuum chamber outside the gas cell is divided into three pressure regions:

i) Between the nozzle and skimmer electrode a rough vacuum (∼1 mbar) is maintained by Roots pumps. Within this region, most of the buffer gas is extracted. Ion transport to the skimmer is by gas flow and by the weak electric field of ∼100 V/cm.

ii) After the skimmer the ions travel through a medium vacuum of $\sim 10^{-4}$ mbar for a distance of ∼60 mm to the extraction electrode. In this region the ion motion is governed by the acceleration due to the extraction electrode potential (∼ 12 kV).

iii) The lowest pressure region is the separator section where the ions have been subject to the main separator acceleration potential (40 kV) and the transport efficiency of the ions is inversely proportional to the vacuum pressure. Beyond the extraction region, for the rest of the beam line, high vacuum conditions of $< 10^{-6}$ mbar are maintained and the ion trajectory determined by electric and magnetic fields only.

Chapter 3

Key aspects of laser resonance ionization

In this chapter an overview of the key aspects of laser resonance ionization is given. To maintain relevance with the work carried out, the discussion is limited to areas that are of particular importance to the application of laser ionization as an efficient method of ion production at the IGISOL and ISOLDE facilities.

A thorough discussion of the subject of laser resonance ionization, with particular emphasis on its use for in-source resonance ionization spectroscopy is presented by V. Letokov in [17].

3.1 Excitation of atomic transitions

3.1.1 Spectroscopic notation and selection rules

In an atom, the electron/nucleus Coulomb interaction gives rise to an electronic energy level structure in which different energy levels are denoted by the principal quantum number n. For a single electron in an atom, the atomic state is defined by the quantum numbers $nljm_j$, where n is the principal quantum number and l is the electron orbital angular momentum. n can be any positive integer and $l = 0, 1, 2, \ldots, n-1$. The total electronic angular momentum j, $j = l + s$, is given by coupling the orbital angular momentum with the intrinsic electronic spin s to

give, $j = l \pm \frac{1}{2}$. The magnetic quantum number m_j is the projection of the orbital angular momentum along its quantization axis.

Under the $L - S$ coupling regime, the spin-orbit interaction and relativistic contributions are assumed to have much smaller scale influence on the energy level structure. In this case, the total electronic orbital angular momentum, L is given by $\mathbf{L} = \sum_i \mathbf{l}_i$ and the total spin, S is given by $\mathbf{S} = \sum_i \mathbf{s}_i$. The total angular momentum, J of an atomic energy level is given by coupling these two terms, $\mathbf{J} = \mathbf{L} + \mathbf{S}$. These quantum numbers give the necessary parameters to characterize an atomic level in standard spectroscopic notation: ${}^{2S+1}L_J$.

For electric dipole transitions between atomic energy levels conservation of angular momentum and parity demands that the condition $\Delta l = \pm 1$ is met. Where $L-S$ coupling holds, further rules apply: $\Delta S = 0$ (not strict), $\Delta L = 0, \pm 1$, $\Delta J = 0, \pm 1$ except for $J = 0 \rightarrow J = 0$ transitions. Additionally $\Delta m_J = 0, \pm 1$ and $\Delta m_J = 0$ is forbidden if $\Delta J = 0$.

3.1.2 Spectral linewidth

As a consequence of the uncertainty principle $\Delta E \cdot \Delta t \geq \frac{1}{2}\hbar$, the atomic spectral line has a natural linewidth resulting from the finite lifetime τ of the excited state:

$$\Delta\nu_{nat} = \frac{1}{4\pi\tau}. \tag{3.1}$$

The resulting spectral line has a Lorentz profile:

$$k_\nu = \frac{1}{2} k_0 \Delta\nu_{nat} / [(\tfrac{1}{2}\Delta\nu_{nat})^2 + (\nu - \nu_0)^2]. \tag{3.2}$$

For a two-level system the natural linewidth of the transition is simply related to the atomic transition probability, A_{ki} using:

$$\tau = 1/A_{ki}. \tag{3.3}$$

For the purposes of resonance ionization and optical spectroscopy, the broadening due to the following further effects must also be considered since they are commonly greater than $\Delta\nu_{nat}$:

- *Doppler broadening.*

- *Power broadening.*

- *Collisional (pressure) broadening.*

These aspects are discussed in the subsequent sections where the neccessity to consider their effects is illustrated by practical examples of their effect.

3.2 Ionization of excited atoms

3.2.1 Non-resonant laser photo-ionization

A commonly utilized route to the continuum is via a non-resonant transition to the continuum from a suitably high-lying excited state.

The low cross section for this type of transition (10^{-19} cm^{-2} – 10^{-17} cm^{-2}) necessitates the use of a large amount of laser power. This is usually supplied with the use of a portion of the beam from the laser used for pumping the tunable laser system. Currently operating laser ion sources use either frequency-doubled Nd:YAG lasers (532 nm) or copper vapour lasers (511 nm and 578 nm) and so for non-resonant ionization, an energy level within 17300 cm^{-1} of the continuum must be populated. The photon absorption cross section for excitation above the ionization potential falls with increasing energy although, within an energy interval close to but above the ionization potential, small fluctuations and even clear resonances (auto-ionizing states) for this transition are often observed. For this reason, for a certain ionizing laser wavelength the effectiveness of this means of ionization is optimized by the careful selection of the energy for the lower level of the transition.

3.2.2 Auto-ionizing levels

As mentioned, for many elements a complex energy level structure exists above the ionization potential. Excited states within this region are known as auto-ionizing states (AIS). They involve the simultaneous excitation of more than one

electron, with the total excitation energy greater than the ionization potential of the element.

Auto-ionizing states can have a short natural lifetime and so are characteristically broad. The decay of these states occurs as a non-radiative process in which the excitation energy is transferred to one of the valence electrons, resulting in ionization.

It has been observed that these states are more abundant for transitions from excited states with a complex electronic configuration involving inner shell electron excitations.

A transition to an auto-ionizing state can exhibit a cross section one or two orders-of-magnitude higher than for non-resonant transitions [20]. In practice, this benefit can be lost due to the lower laser power provided by the tunable laser. The importance of these states is very much laser system or application dependent. In Chapter 6, the added efficiency brought about by the use of an auto-ionizing state is shown in the discussion of the new scheme for gold. Additionally, for spectroscopy purposes, the convenience of the use of a broad auto-ionizing state as the final step in the ionization of bismuth is discussed.

3.2.3 Rydberg state

The photon absorption cross section for transitions to the high-lying and abundant Rydberg levels can be large (10^{-14} cm^{-2}). The Rydberg levels are a series of electronic states with high n. Since the atomic radius is approximately proportional to n^2, an electron occupying one of these levels has a binding energy of the order of tens of meV, minute compared to a typical transition energy of $\sim$ 3eV. As a result, the delicate atomic system is extremely sensitive to external effects such as collisions (collisional ionization) with other atoms or changes in the local electric or magnetic field (field ionization).

Field ionization

If an atom is subject to a sufficiently intense electric field, its high-lying discrete states within the Rydberg series will merge with the ionization continuum. An electron occupying one of these states will can a high cross section for dissociation which is dependent on the electric field strength and its principal quantum

number. If a transition to a high n state is used, the ionization efficiency can be high in even a weak electric field ($< 2000 V cm^{-1}$). This was been demonstrated by Letokhov et al. [21] during a resonance ionization spectroscopy (RIS) study of the Fr Rydberg levels.

Collisional ionization For an electron in a state of high n, the collisional ionization probability can be extremely large on account of three contributing effects. The first is a simple geometric contribution; the n^2 dependence of the atomic radius translates to a collision probability proportional n^4. Secondly, the state lifetimes are usually long ($\sim \mu s$) so the probability of an atom collision before the spontaneous decay of the state can be high. Finally, the states are characteristically weakly bound so the probability of ionization in the event of a collision is also high.

3.2.4 Frequency Multiplication

At the fundamental frequency, the spectral range of tunable laser systems is not sufficient to enable their application for efficient resonant ionization of a wide range of elements. In fact, for many elements, suitable first excited states lie at an energy that is far into the UV region, corresponding to a wavelength less than half of that achievable at the short wavelength end of the tuning range of a dye-laser system.

These transitions are, however, accessible if the second or third-harmonic of the fundamental emission frequency is generated. For laser light, the generation of multiple harmonics within certain optical materials is possible due to the non-linear effects resulting from the characteristically high electromagnetic fields that can be generated.

When light passes through an optical material, a polarization response to the electric field occurs. At low laser intensity the polarization of transparent materials can be considered to vary linearly with the applied field:

$$\mathbf{P} = \chi \varepsilon_0 \mathbf{E} \tag{3.4}$$

where χ is the electric susceptibility and $\mathbf{P}$ is the polarization vector (the dipole moment per unit volume that is induced in a material due to an applied electric field).

For optically isotropic materials, χ is constant. In a non-linear optical material (anisotropic with respect to the refractive index), χ becomes a tensor accounting for the multiple-order polarization responses of the material.

If the electric field is sufficiently high (e.g a pulsed laser beam focussed to a narrow beam waist), non-linear interactions must be considered and Equation 3.4 must be generalized to

$$\mathbf{P} = \varepsilon_0 \left(\chi_1 \mathbf{E} + \chi_2 \mathbf{E}^2 + \chi_3 \mathbf{E}^3 + \cdots + \chi_n \mathbf{E}_n \right). \tag{3.5}$$

The polarization is a consequence of charge oscillations within the material induced by the intense oscillating field generated by the laser light. The radiation of these oscillations effectively add to the electric field. The scalar quantities, χ_1, χ_2, χ_3 are the material properties of linear susceptibility and the second- and third-order non-linear susceptibilities respectively. For some materials the non-linear susceptibilities are sufficiently large for their polarization effect to be comparable to that for the linear term.

3.2.4.1 Frequency doubling

For laser light of angular frequency $\omega = 2\pi\nu_1$ the electric field, E can be described by

$$E = E_0 e^{-i\omega t} + E_0^* e^{+i\omega t}. \tag{3.6}$$

Passing through an optical material with a non-zero value of χ_2, the second-order non-linear polarization term given by $P_2 = \varepsilon_0 \chi_2 E^2$ becomes

$$P_2 = 2\varepsilon_0 \chi_2 E^* E + 2\varepsilon_0 \chi_2 E^2 e^{-i(2\omega)t} + 2\varepsilon_0 \chi_2 (E^*)^2 e^{i(2\omega)t} \tag{3.7}$$

for which the time-dependent terms have characteristic frequencies of precisely twice the frequency of the incident laser light. Under certain conditions, these terms can result in a significant conversion of the fundamental beam to a second beam with twice the original frequency. This was first demonstrated by Franken *et al* [22]. The main difficulty associated with second-harmonic generation (SHG) lies in the frequency dependence of the refractive index of the material. This results in in-coherent production of the second-harmonic beam at different

positions within the material. This can severely affect the conversion efficiency due to destructive interference of the second-harmonic beam. This can be avoided if the phase velocities of the fundamental and the second-harmonic are the same. For a uniaxial non-linear crystal it is possible to select an axis of propagation for which this is true. This technique is known as *phase matching* and it is described in some detail in [23]. The principle of second-harmonic generation can be generalized to account for two incident beams with different frequencies. If phase matching is achieved, it is possible to generate a beam at a frequency equal to the sum of the frequencies of the two incident beams. This technique is known as 'sum frequency' generation.

Chapter 4

Nuclear Properties by Laser Spectroscopy

4.1 Introduction

The finite size of the nucleus reduces the depth of the Coulomb potential within the volume of the nucleus. The binding energies of electronic states which have a finite electron density in the nucleus are therefore slightly less bound at the ppm level. The precise techniques of laser spectroscopy are sensitive to these perturbations through measurements of optical *isotope-shifts* and their measurement provides information on the nuclear size and charge distribution.

Another level of complexity is added for nuclei with non-zero spin for which, the resulting multipole moments give rise to a further splitting of the fine structure levels to give the *hyperfine structure*. These effects are collectively known as the *hyperfine interactions*. Within the scope of nuclear structure physics, the field of laser spectroscopy relies upon these minute nuclear parameter-dependent effects, the measurements of which allow determination of the nuclear spin, charge radii differences and the nuclear moments.

These perturbations to the atomic structure are incorporated into the atomic Hamiltonian through the use of a multipole expansion. The monopole term accounts for the changes in the nuclear charge distribution and so is characterized by the isotope-shift. The next two terms consider the electromagnetic interactions between the atoms and the nucleus and so are responsible for the hyperfine

structure splitting. The magnetic dipole interaction is the dominant of these, and describes the energy of the nuclear magnetic moment in the magnetic field of the electrons. The quadrupole term considers the nuclear charge distribution and its interaction with the electric field gradient produced by the orbital electrons. Perturbations associated with the higher-order terms (octupole and hexadecapole) moments are normally of considerably smaller magnitude and not experimentally observable by laser spectroscopy.

4.2 Isotope and isomer-shifts

Within the nucleus, the addition or removal of neutrons will change the mass and charge distribution. The consequential perturbation to the atomic structure can therefore be broken down into two discernible components. The mass dependent effect, (*the mass shift*), arises due to the recoil energy of a nucleus of finite mass. The electrostatic effect, (*the field shift*), arises due to the finite nuclear volume and its distribution of charge. Each of these gives rise to a systematic shift, $\delta\nu_i^{AA'}$ in a spectral line, i between two isotopes A' and A:

$$\delta\nu_i^{AA'} = \nu_i^{A'} - \nu_i^{A} \tag{4.1}$$

with A' being the heavier of the two isotopes. To a good approximation, a linear combination of these effects gives the total isotope-shift of the spectral line [24]:

$$\delta\nu^{AA'} = \delta\nu_{MS}^{AA'} + \delta\nu_{FS}^{AA'}. \tag{4.2}$$

4.2.1 Mass shift

The mass shift (MS) is apparent in the kinetic energy term of the Hamiltonian. The recoil momentum of the nucleus ($\boldsymbol{p}_n$) is equal and opposite to the total recoil momentum, $\mathcal{T}$, of the atomic electrons ($\sum_i \boldsymbol{p}_i$). Therefore, by substitution

$$\mathcal{T} = \frac{\boldsymbol{p}_n^2}{2M} + \sum_i \frac{\boldsymbol{p}_i^2}{2m_e} \tag{4.3}$$

$$= \frac{\left(\sum_i \boldsymbol{p}_i\right)^2}{2M} + \sum_i \frac{\boldsymbol{p}_i^2}{2m_e} \tag{4.4}$$

$$= \frac{\sum_i \boldsymbol{p}_i^2}{2M} + \frac{\left(\sum_{i>j} \boldsymbol{p}_i \cdot \boldsymbol{p}_j\right)}{M} + \sum_i \frac{\boldsymbol{p}_i^2}{2m_e}. \tag{4.5}$$

In an isotope-shift measurement, the experimentally observed quantity is the kinetic energy change between two isotopes, given by

$$\delta(\Delta E) = \mathcal{T}(M') - \mathcal{T}(M) = \frac{M' - M}{M'M}\frac{1}{2}\left[\sum_i \boldsymbol{p}_i^2 + 2\sum_{i>j} \boldsymbol{p}_i \cdot \boldsymbol{p}_j\right]. \tag{4.6}$$

The two terms in this linear combination can be discussed separately as the normal mass shift (NMS) (the ${p_i}^2$ term), and the specific mass shift (SMS) (the $(p_i \cdot p_j)^2$ term). For laser spectroscopy, energies are more conveniently discussed in terms of transition frequencies. Using this terminology, the change in transition frequency due to the mass shift ($\delta\nu_{MS}^{AA'}$) is simply the sum of the NMS ($\delta\nu_{NMS}^{AA'}$) and SMS ($\delta\nu_{SMS}^{AA'}$) components.

$$\delta\nu_{MS}^{AA'} = \delta\nu_{NMS}^{AA'} + \delta\nu_{SMS}^{AA'}, \tag{4.7}$$

$$= \frac{A' - A}{A'A}\left[NMS + SMS\right], \tag{4.8}$$

for which the NMS is directly calculable as $(m_e/m_p)\nu_0$ where ν_0 is the transition frequency for an infinitely heavy nucleus. On the other hand, the SMS is the result of an intricate mixture of angular momenta couplings between electron pairs and so cannot be analytically determined. The entailing uncertainty therefore limits the accuracy of the interpretation of the isotope-shift measurements.

The reliability of calculated values for SMS is questionable, but for $s \rightarrow p$ transitions one can assume a reasonably good approximation has been made. Examples of commonly quoted values taken from Reference [25] are

$$\delta\nu_{SMS}^{AA'} = 0.3 \pm 0.9\delta\nu_{NMS}^{AA'} \qquad ns - np \tag{4.9}$$

$$\delta\nu_{SMS}^{AA'} = 0.0 \pm 0.5\delta\nu_{NMS}^{AA'} \qquad ns^2 - nsnp \tag{4.10}$$

For the heavier elements, where the MS is a smaller fractional contribution to the total IS, the systematic error due to the uncertainty in SMS diminishes.

If enough experimental data are at hand, an effort can be made to extract the SMS from a comparison of the isotope-shifts for two spectral transitions using a 'King Plot' [24]. This method can be applied to non-optical measurements such as electronic X-ray scattering [26] or muonic X-ray isotope-shifts [27].

4.2.2 Field shift

First-order perturbation theory gives the energy shift of an atomic state Ψ(r) for a finite-size nucleus compared to a point nucleus as

$$\Delta E = \frac{Ze^2}{6\epsilon_0}\langle r^2\rangle|\Psi(0)|^2 \tag{4.11}$$

where $\langle r^2\rangle$ is the nuclear mean-squared charge radius and $|\Psi(0)|^2$ is the electron density at the nucleus. The small frequency shift of a spectral line in an isotope A compared to another A' is then

$$\delta\nu = \frac{Ze^2}{6\hbar\epsilon_0}\delta\langle r^2\rangle^{A,A'}\Delta|\Psi(0)|^2 \tag{4.12}$$

where $\Delta|\Psi(0)|^2$ is the change in electron density between the states involved in the optical transition and $\delta\langle r^2\rangle^{A,A'}$ is the change in the mean-squared charge radius between the isotopes.

Factors affecting $\langle r^2\rangle$ include the slight volume change of the nuclear charge as neutrons are added and shape changes which can have a substantial effect on the mean-squared charge radius. For example, an axially symmetric nucleus with a quadrupole deformation parameter β_2 has an increased mean-squared charge radius given by

$$\langle r^2\rangle = \langle r^2\rangle_0(1 + \frac{5}{4\pi}\beta_2^2) \tag{4.13}$$

where $\langle r^2 \rangle_0$ is the mean-squared charge radius for the spherical nucleus of the same volume. A full review of isotope-shift analysis and interpretation is given in [7].

4.3 Hyperfine structure

Only even-order electric and odd-order magnetic moments are present in nuclei. Of these, only the magnetic dipole, and electric quadrupole moments tend to be large enough to have a measurable effect on the hyperfine structure (HFS).

The coupling of nuclear spin and electronic angular momentum results in a total angular momentum F, which is a constant of motion and defined by,

$$\mathrm{F} = \mathrm{I} + \mathrm{J} \, . \tag{4.14}$$

For a atomic level of total electronic angular momentum $\boldsymbol{J}$, the energy splitting, ΔE_F is given by

$$\Delta E_F = \frac{A_J K}{2} + \frac{B_J}{4} \frac{[\frac{3}{2}K(K+1) - 2J(J+1)I(I+1)]}{I(2I-1)J(2J-1)} \tag{4.15}$$

where K is given by,

$$K = F(F+1) - J(J+1) - I(I+1). \tag{4.16}$$

The factors A and B are the hyperfine structure-coupling coefficients, which determine the magnitude of the hyperfine splitting. The A value is related to the nuclear magnetic moment by

$$A = \frac{\mu B}{IJ}. \tag{4.17}$$

and B is related to the electric quadrupole moment of the nucleus:

$$B = eQ_s \overline{V_{JJ}(0)}. \tag{4.18}$$

Direct calculation of B and $\overline{V_{JJ}(0)}$ is difficult and the achievable level of accuracy is often questionable. If however, the nuclear moments and spin are known for another isotope, they can be determined for other isotopes from the experimentally measured A and B coefficients using the scaling relations:

$$\mu_{A'} = \frac{A_{A'} I_{A'}}{A_A I_A} \mu_A \tag{4.19}$$

and

$$Q_{A'} = \frac{B_{A'}}{B_A} Q_A, \tag{4.20}$$

with the assumption that there is no variation of the atomic fields or the nuclear magnetization over the nuclear volume.

4.3.1 Hyperfine anomaly

The calculation of the hyperfine interaction of s and $p_{1/2}$ electrons in the field of an extended nucleus was first performed by Bohr and Weisskopf, who showed that the hyperfine A coefficient is generally smaller than expected for a point nucleus. This difference between the point nucleus A coefficient and that for an extended nuclear magnetization is commonly referred to as the Bohr-Weisskopf (BW) [28] effect.

As a result of the BW effect the ratio of magnetic moments and the ratio of hyperfine A coefficients frequently do not quite correspond as they should if Equation 4.19 holds. In order to explain these deviations a modification must be made to the equation:

$$\mu_{A'} = \frac{A_{A'} I_{A'}}{A_A I_A} \mu_A (1 + \Delta^{A',A}) \tag{4.21}$$

where

$$1 + \Delta^{A',A} = \frac{1 + \epsilon_{A'}}{1 + \epsilon_A} \simeq 1 + \epsilon_{A'} - \epsilon_A, \tag{4.22}$$

$\Delta^{A',A}$ is known as the hyperfine anomaly and arises as an effect of changes in the distribution over the nuclear volume of nuclear magnetization and the non-uniformity of the magnetic field B. ϵ_A is a correction to the hyperfine A coefficient to allow for the BW effect, and to a good approximation, the difference in these

values between two isotopes gives their hyperfine anomaly. More information on the hyperfine anomaly can be found in [29].

Chapter 5

The ISOLDE Resonance Ionization Laser Ion Source

5.1 Introduction

The RILIS system at ISOLDE is described thoroughly in References [6] and [30]. The key concepts and technical details are discussed here.

5.1.1 The hot cavity ionizer

A high photon flux is required to saturate atomic transitions. Additionally, schemes using a non-resonant laser ionization step are not feasible unless the laser power is of the order of many kW. This is only practically achievable with the use of pulsed laser systems. If a pulsed laser is used, the ionization efficiency of the ion source hinges upon the ability to ensure that each atom has a chance to interact with the laser pulse. At ISOLDE, the hot cavity of the standard surface ion source provides a convenient laser interaction region. Whilst the primary role of the cavity is to confine the atoms as they effuse from the target for enough time to ensure at least one coincidence with a laser pulse, a complex combination of additional cavity effects can be either beneficial or detrimental to the RILIS performance. It has been found that for a standard tungsten cavity, a temperature of around 2300 K gives optimum RILIS efficiency. This depends upon the specific requirements of the user and also on the element being ionized but the

choice of temperature is usually a matter of striking a balance between RILIS efficiency and selectivity and can be most easily understood by discussing these two factors separately:

5.1.1.0.1 Efficiency A high cavity temperature is needed in order to confine the reaction products without losses due to wall sticking. Optimizing the cavity temperature for RILIS creates conditions synonymous to those for standard surface ion source operation and so ions can be created with a high degree of efficiency on the surface of the cavity. The RILIS can benefit greatly from the ionizer 'cavity effect' since the resulting plasma potential in the cavity gives a degree of transverse confinement for the laser ions, greatly improving their extraction efficiency. An example of this principle is presented in Figure 6.7, where an increase in the yield for dysprosium atoms is seen as the hot cavity temperature is increased. Additionally, Doppler broadening increases the width of the resonant transitions to the order of a few GHz, therefore more laser power is required for saturation or a sufficiently broad-bandwidth laser is needed to ensure resonance with the frequency spread of the atomic spectral line across the velocity distribution. In the high-temperature RILIS cavity the thermal distribution of the atoms can result in a significant population of the higher energy components of a split ground-state. Large RILIS efficiency losses can be observed if the fine structure splitting exceeds the Doppler broadening of the atomic transition and the laser bandwidth. Atoms in these low-lying excited states may not be resonant with the laser-frequency set for a transition from the ground-state.

5.1.1.0.2 Selectivity Unfortunately, in using a standard surface ion source hot cavity for RILIS ionization, gains in efficiency can be accompanied by a loss of selectivity. If the RILIS ionized isotope of interest has an isobar neighbour that is readily produced in the target and easily surface ionized, isobaric background can form a significant proportion of the beam. Increasing the cavity temperature will often improve the surface ionization efficiency at a higher rate than the corresponding RILIS efficiency, detracting from the achievable RILIS selectivity. The extent of the problem of isobaric beam impurities and some techniques used to suppress them are discussed later in this chapter.

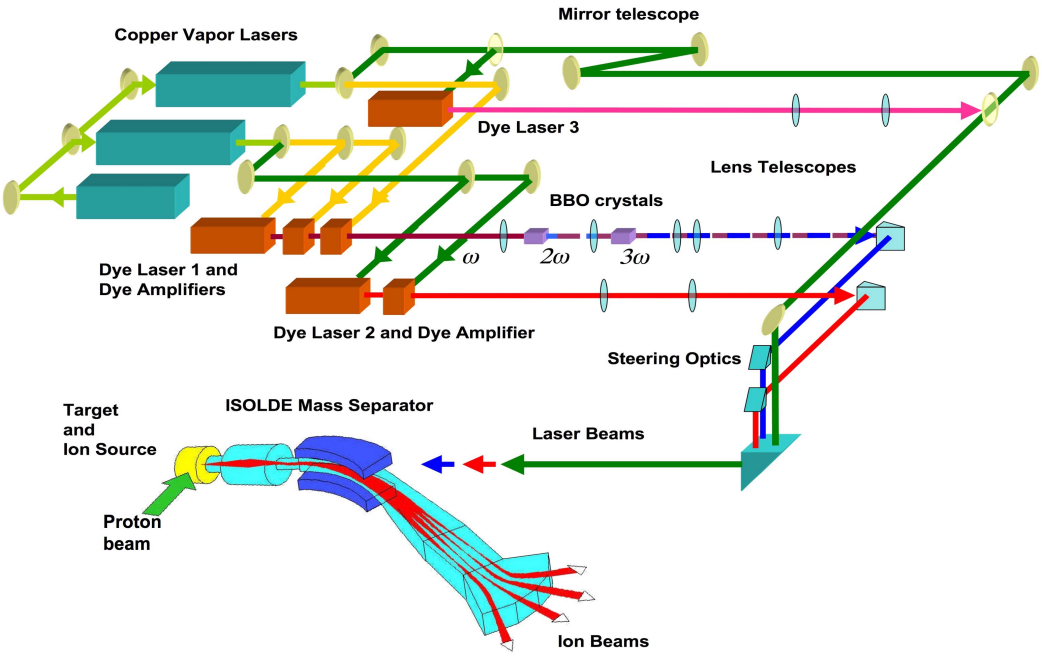

Figure 5.1: The RILIS laser system.

5.1.2 The laser system

The RILIS laser system is housed in a shielded room above the junction of the beam-lines emerging from the high resolution separator (HRS) and the general purpose separator (GPS) magnets. Figure 5.1 is a schematic of the laser setup. Three pico motor mounted mirrors send the separated beams for each transition to a series of quartz prisms which steer the beams towards the hot cavities of the GPS or HRS target units, located 18 m and 23 m away respectively. For alignment purposes a portion of the laser beams (approximately 5% of the laser power) is reflected from quartz plates which are situated approximately half way along the beam path towards the ion source. After traveling a distance approximately equal to that of the full power beam, the reflected beams meet a black metal plate back inside the laser cabin. A 3 mm diameter hole in this reference plate is representative of the hot cavity entrance dimensions and adjustment of the pico motor mirrors to maximize the transmitted beam power ensures correct alignment

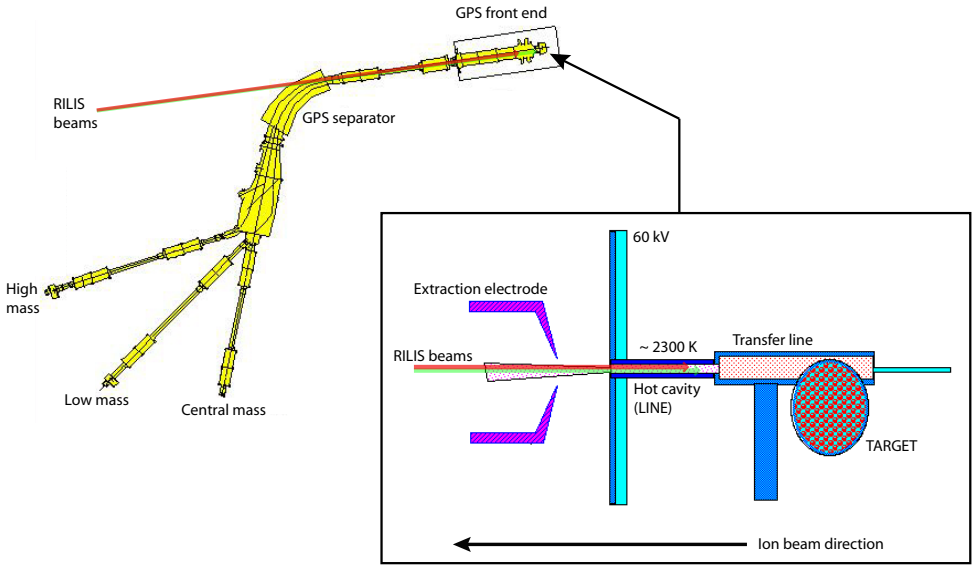

Figure 5.2: RILIS access to the ISOLDE surface ion source cavity. Ionization takes place within the surface ionizer cavity of a standard target/ion source unit (inset).

of the beams.

The laser wavelengths are read by sending a small portion of the beam through a single-mode optical fiber to an ATOS LM007 Lambdameter connected to a PC. The laser beam transport and observation system is described in detail in [31].

5.1.3 The copper vapour laser

The copper vapour laser (CVL) system is built to function with commercially available laser tubes and consists of a small laser oscillator and the two larger amplifiers. The tubes are filled with neon gas and contain copper sources. By applying fast high repetition rate electrical pulses to the tube a neon discharge is created. This heats the tube to the temperature of around 1500°C which is required to vaporize the copper. These fast pulses are achieved using hydrogen gas discharge switches known as thyratrons. These are capable of holding a potential of around 16 kV which can be released very rapidly with application of a small trigger pulse. The trigger pulses for the three laser tubes are synchronized. The

laser oscillator, the smaller of the tubes, produces 6-8W of laser light in the form of 18 ns pulses at a repetition rate of 11 kHz. The 12 mm diameter laser beam is split and passes through the two, parallel amplifier tubes. The output beams have a diameter of 20 mm and the power from each amplifier tube is approximately 35 W and contains components from two copper spectral lines: 55% green (511 nm) and 45% yellow (578 nm).

The CVLs are primarily used for the pumping of the dye lasers and amplifiers but for schemes with non-resonant ionization steps, either the green or yellow component of CVL beam is often used (or both components combined).

5.1.4 The pulsed dye lasers

Many different tunable laser systems are available for spectroscopic purposes. If we consider that, at ISOL facilities, the primary goal is the efficient ionization of all atoms of a particular element, the technical requirements of high repetition rate and power density (short pulse length) limits the range of suitable laser types to just two: the pulsed dye laser or the Ti:Sapphire laser.

A detailed description of various tunable dye-laser systems is given in [23]. Most tunable laser systems rely on the use of a gain medium with a broad band and continuous emission spectrum. The selection of the desired frequency is performed by configuring the laser cavity to support the corresponding lasing mode. In the dye laser, organic dye molecules dissolved in a polar solvent form the gain medium. Following excitation of the complex dye molecules, relaxation occurs via a multitude of vibrational and rotational transitions. Due to the abundance of these spectral lines, a continuous and extremely broad emission profile is observed. For the pulsed dye laser, the liquid dye is incorporated into the laser cavity in the form of a fast flowing sheet, typically 15 mm wide (along the length of the laser cavity) and 0.5-1.5 mm in depth. For high repetition rate (>10 kHz) systems, a flow rate of over 5 l/min ensures that, for each excitation pulse a fresh dye volume is illuminated. Most commonly, the laser cavity is a Hänsch oscillator [32], where a diffraction grating forms the rear cavity mirror and wavelength selection is achieved by precise tuning of the grating angle. A series of Brewster cut

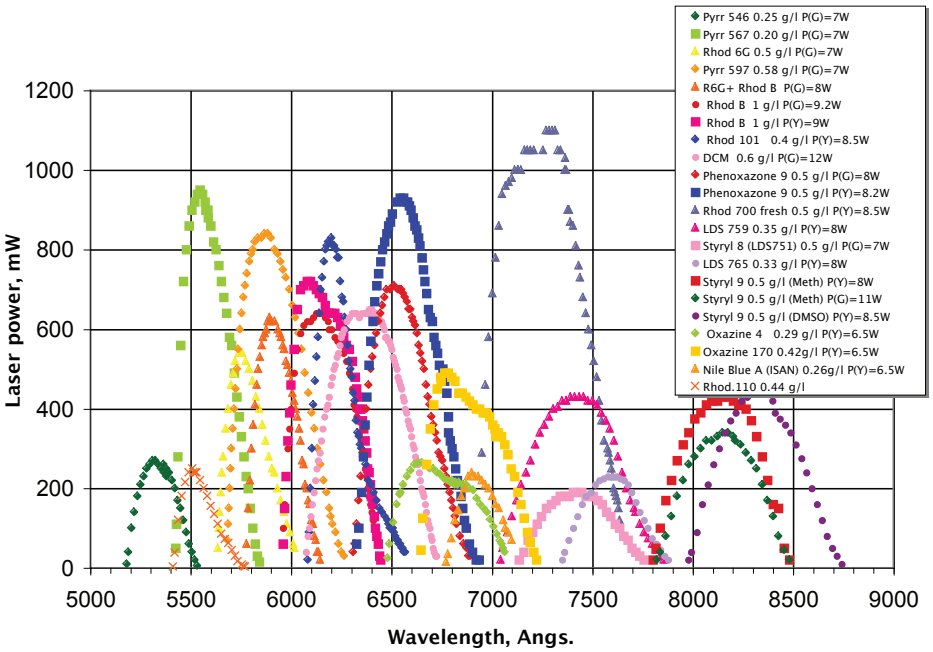

Figure 5.3: The CVL pumped pulsed dye-laser tuning range.

prisms within the cavity introduce an element of polarization selection, improving the ratio of stimulated:spontaneous emission within the output beam.

The RILIS has three dye lasers, each with up to two amplifier cells. Schemes which employ up to three resonant transitions can be used. The wavelength range of the dye lasers is 530-850 nm. Frequency doubling and summation (tripling) by non-linear BBO (beta-barium borate) crystals provides shorter wavelengths in the range 213-440 nm.

Precise tuning of the wavelength is achieved by adjusting the angle of the diffraction grating in the laser resonator. Depending on the grating used, the line-width of each dye laser is between 9 and 30 GHz.

For some atoms, atomic physics effects such as the isotope-shift and hyperfine structure can effectively broaden the width of the transition by splitting the resonance position into different hyperfine or isotopic components spread over a range of possibly tens of GHz. Provided that the transition is saturated, optimal efficiency is therefore achieved by the use of broadband lasers.

Whilst the Doppler broadening of the atomic lines in the hot cavity ionizer

sets a lower limit on the spectral resolution of RILIS (> 1.4 GHz), the laser bandwidth can be reduced to close to this limit by placing an etalon into the laser cavity. Operating in this mode, it is sometimes possible for isotopes or isomers of some elements to be selectively ionized through their differences in hyperfine structure. Using this technique, the first demonstration of isomer-selective photo-ionization in a gas cell was conducted by Dyer et al [33] for ^{197}Hg and for selective ionization of ^{141}Sm and ^{164}Tm by Mishin et al [34]. Since then it has been applied at ISOLDE for the selective ionization of copper isomers for mass measurements at ISOLTRAP [35]. More recently, the same technique was used in conjunction with the REX facility at ISOLDE to produce the first post-accelerated isomer pure ion beam for Coulomb excitation measurements using the MINIBALL array [36].

For the first-step transitions the dye laser 1 is used and wavelength adjustments are made via microprocessor control unit. For laser 2 and 3 tuning is done manually.

5.1.5 Frequency multiplication

A large proportion of the ionization schemes in use at RILIS require generation of multiple harmonics of the fundamental frequency of the dye-laser output. This process is described briefly in Section 3.2.4 and comprehensively in Reference [23]. The techniques of second-harmonic generation and sum frequency generation are used to generate light at double and triple the fundamental frequency respectively.

Several setup configuration options for the RILIS dye lasers are shown in Figure 5.4. Setup **iv** uses the new frequency tripling unit, allowing independent focussing and steering of the first and second-harmonic beams. With this unit, more stable operation and higher tripling efficiencies have been achieved. The frequency multiplication process results in an elliptical beam. Cylindrical lenses positioned within the telescope allow focussing and reshaping of the beam in two dimensions individually. Phase matching is achieved by tuning the angle of the optical axis of the crystal with respect to the direction of propagation of the incident beam. The frequency doubling and tripling efficiencies ($\xi_{2\omega}$ and $\xi_{3\omega}$) are given by

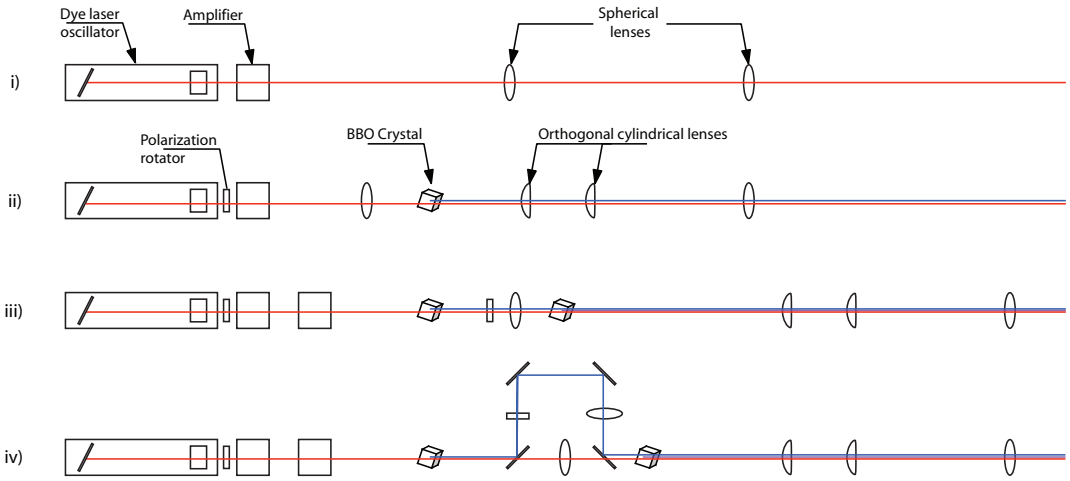

Figure 5.4: The four commonly used RILIS dye-laser configurations: **i)** Fundamental beam with standard telescope; **ii)** Second-harmonic generation with polarization rotator, tight focussing within the crystal and cylindrical beam reshaping lenses; **iii)** Old third-harmonic generation setup; **iv)**New third-harmonic generation setup with independent control of the first and second-harmonics.

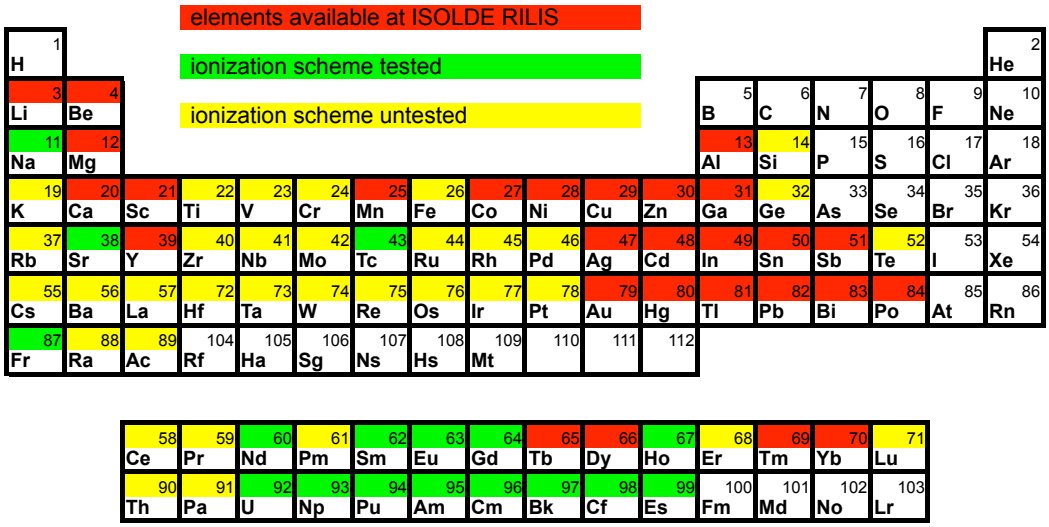

Figure 5.5: The current capability of RILIS. For the elements highlighted green, a feasible ionization scheme is known. The potential scope of RILIS is limited by the range of elements released from the ISOLDE target. The low vapour pressure elements (e.g Hf, Ta, W, Os), the release characteristics are poor.

$$\xi_{2\omega} = \frac{P_{2\omega}}{P_{\omega}} \tag{5.1}$$

and

$$\xi_{3\omega} = \frac{P_{2\omega}}{(P_{\omega} \cdot P_{2\omega})^{\frac{1}{2}}} \tag{5.2}$$

where P_{ω}, $P_{2\omega}$ and $P_{3\omega}$ are the power the fundamental, second harmonic and third harmonic beams respectively.

5.1.6 Ionization schemes

With the inclusion of the new ionization schemes presented in Chapter 6, the RILIS is currently capable of ionizing 27 of the elements. The current scope and the potential of the RILIS is shown in Figure 5.5.

It is clear that much work remains to be done to maximize the versatility of the laser ion sources. Of primary importance is extending the range of elements for

which laser ionization may be applied. In principle, multi-step photo-ionization can be used to provide an ion beam of any element provided that the atom can be transported to the laser interaction region and that the excitation scheme falls within the laser wavelength tuning range. For the ISOLDE RILIS, the first of these criteria rules out the very refractory elements (e.g Os, Re, Th) that do not escape from the target matrix. For some of the remaining elements, ionization is not currently achievable with the RILIS laser system due to the high-lying nature of the first excited states (outside the wavelength tuning range) or high ionization potentials (laser pump power limitations).

5.1.7 Background suppression

Two approaches can be taken for the suppression of unwanted isobaric contaminants; by incorporating additional selection methods which exploit physical or chemical differences between the ions and their isobars, or by increasing the efficiency of release of the isobars of interest, improving the signal/background ratio.

5.1.7.1 Ion beam gating

The diffusion and effusion times of reaction products into the ionizer cavity are largely element dependent [37]. Following the short proton pulse, the release of the various isobars can take from a few tens of ms to a few hours depending on their volatility and reactivity. The ion beam can be periodically dumped onto a catcher by electrostatic deflection, this beam gate can be opened during the optimal release time for the desired element. Alternatively, where the contamination is from a short-lived species, a delay between the proton pulse and the beam gate opening can reduce the contamination.

5.1.7.2 Temperature Optimization

A degree of chemical selectivity can be achieved by the adjustment of the transfer line temperature (the junction between the target container and the ion source). This can limit the release of contaminants provided that they are less volatile than the required element. This thermo-chromatography process is particularly

important for use in conjunction with the very non-selective plasma ion source and has resulted in effective suppression of cesium and indium to provide a clean beam of neutron-rich cadmium [38].

5.1.7.3 Cavity material and design

The efficiency of the RILIS is improved by efficient extraction of the laser-ionized atoms. This is done by increasing the potential drop along the length of the cavity. The increase in voltage and hence increase in ohmic heating of the cavity results in a greater yield of surface-ionized contaminants. A reduction in cavity wall thickness will limit the current flow, allowing a higher potential for a given cavity temperature. This is particularly visible when comparing the bunched release times of ions from a thin niobium cavity with that of a standard tungsten cavity at a higher temperature [39]. The bunch width for the thin cavity is considerably narrower, indicating that an increased signal-to-background ratio could be achieved if the ion beam was gated across a small time window ($<20\mu$s).

Chapter 6

Ionization Scheme Development for RILIS

The RILIS ionization scheme development described here has extended the number of elements than can be supplied as RILIS ionized beams from 22 to 27. The new schemes for antimony, dysprosium, scandium and yttrium were determined by means of resonance ionization spectroscopy (RIS) of a stable sample during which numerous first and second excited states were tested to produce ionization schemes that employ two resonant steps followed by non-resonant ionization with the high power CVL beam. During the RIS study of stable gold, an extensive search for auto-ionizing states was performed and an efficient three-resonance, three-step scheme has been determined. The new ionization schemes are presented in Figure 6.1.

A generalized description of the experimental procedure for this type of investigation is given in this chapter with the specific details and results of each RIS study presented in the subsequent subsections.

6.1 RILIS scheme development

Ionization scheme development at RILIS has become a well-established procedure and uses the RILIS laser system and one of the ISOLDE mass separators operating in off-line mode. The RIS study for new scheme development comprises of four key stages:

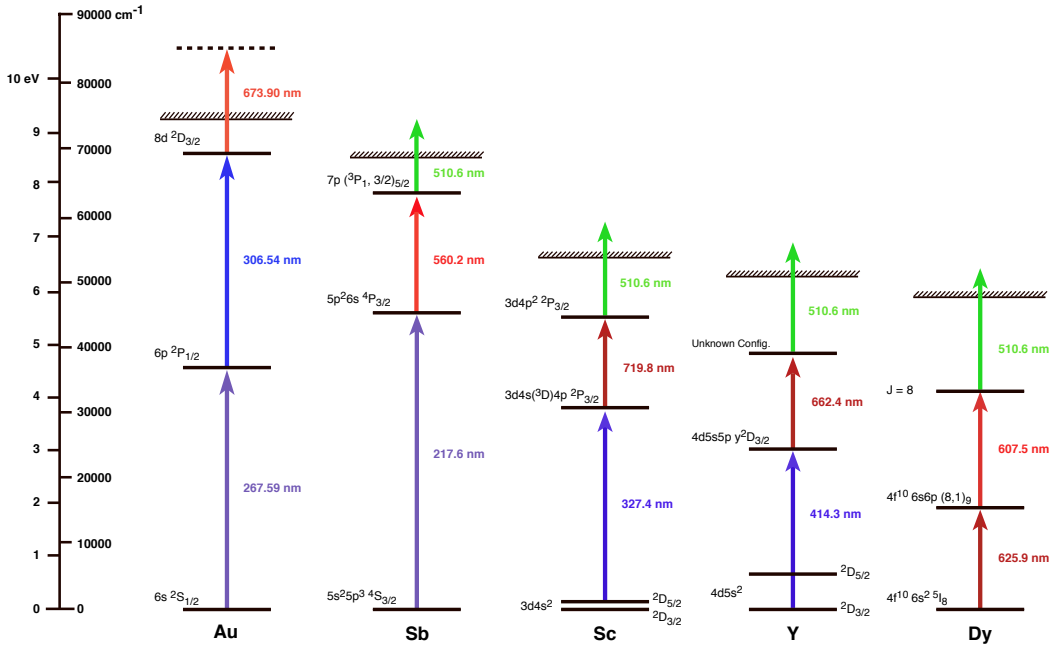

Figure 6.1: The new RILIS ionization schemes.

Literature study

After studying the various sources of atomic spectral line data, theoretical ionization schemes can be constructed. Some predictions about the relative efficiencies of the proposed schemes can be made if the data include measurements of the line strengths. The Kurucz web-based atomic spectral line database [40] and a series of resonance ionization spectroscopy data sheets by E.B. Saloman [41] have been particularly useful for this data collection procedure.

Resonance ionization spectroscopy

A small sample of the stable isotope is placed in an oven, which is attached to the target. Heating the oven releases the sample as an atomic vapour that effuses into the ionizer cavity. For the work described here, where three-step schemes are investigated, resonance ionization spectroscopy (RIS) involves scanning the second-step frequency across the range of possible transitions whilst the frequency of the first-step transition is fixed. The ion current is monitored on a Faraday cup detector to locate the resonance positions.

Saturation measurements

For selected transitions, the dependence of the ion current versus the power of the laser beam is measured. Saturation is characterized by a loss of the linear dependence of the ion current on laser power. A gradual reduction in the gradient of the saturation curve is observed and a plateau is reached. The saturation power is the laser power corresponding to the intersection of a line extrapolated from the initial linear section with a horizontal line extending from the plateau point. The experimentally measured saturation power (which is deposited within the 3 mm diameter of the ion source cavity) gives an indication of minimal required power for RILIS operation without the loss of efficiency.

Efficiency measurement

The tabulated values for the RILIS efficiency represent a measure of the combined efficiency of ionization, extraction, and release from the mass separator. A small (few μg) mass tracer of the stable isotope is placed either in an empty target container or in the oven attached to the target. After tuning the lasers to the chosen ionization scheme and setting the mass separator to transmit the most abundant stable isotope, heating of the oven begins the tracer evaporation and its release into the ion source. The transmitted ion current is monitored on a Faraday cup detector. After complete tracer evaporation, the total ion release, given by the integrated ion current is compared with the original sample size to give the RILIS efficiency. For elements that are readily surface ionized in the hot cavity (in this case Sc and Y), the RILIS efficiency ξ_{RILIS} can be measured without the need to operate the lasers. This requires the laser on/off ion current ratio $I_{laser}/I_{surface}$ to be known for the values of ion source and target heating current that are set during the evaporation. The RILIS efficiency is therefore given by:

$$\xi_{RILIS} = \frac{\frac{I_{laser}}{I_{surface}} \int I_{surface}(t)dt}{N_{mm}} \tag{6.1}$$

where N_{mm} is the mass marker sample size (in nAh). For a case where RILIS provides no enhancement, the laser on/off ratio is equal to unity and $\xi_{RILIS} = \xi_{surface}$.

6.2 Antimony

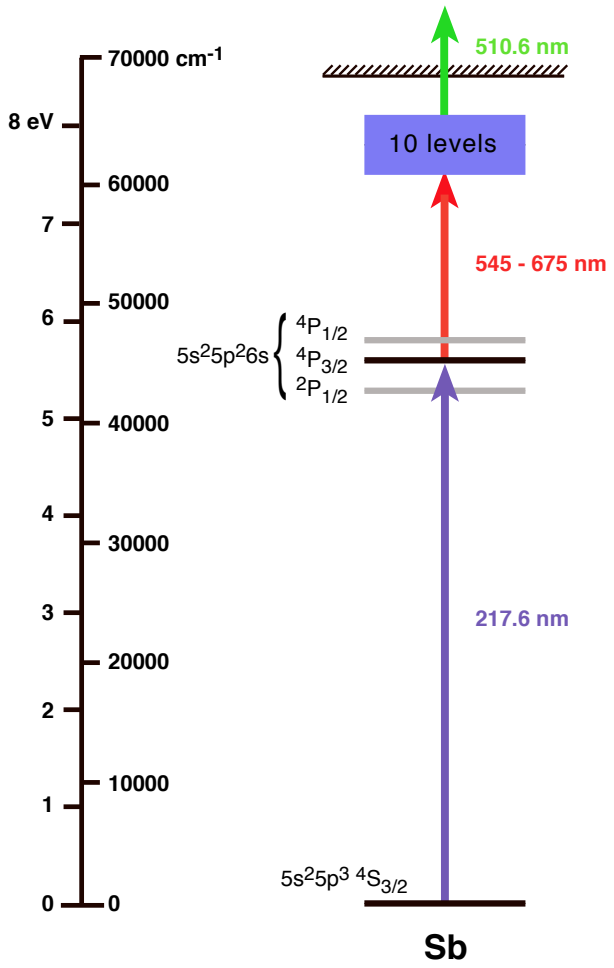

Figure 6.2: The Sb transitions and scanning range studied during the ionization scheme development.

Antimony has a ground-state configuration of $5s^25p^3\ {}^4S_{3/2}$ and three known excited states accessible by photon absorption lie between 43000 and 47000 cm^{-1}. The transition to the $5s^25p^26s{}^4P_{3/2}$ level at 45945.3 4 cm^{-1} was chosen due to the abundance of known second-step transitions from this level and, since this level shares the same multiplicity, *2S + 1*, as the ground-state, the transition was expected to be relatively strong. An energy of 45945.34 cm^{-1} corresponds

to a wavelength of 217.58 nm. This is at the short wavelength end of the RILIS tuning range and is produced by third-harmonic generation using the frequency summing technique described in Section 3.2.4. Using Equation 5.2, the efficiency of third-harmonic generation was determined to be 5 % for the 5 W fundamental beam and 800 mW of laser power in the second harmonic. The 652.77 nm fundamental beam was produced by pumping the DCM dye with the 511 nm component of the CVL beam.

Table 6.1: Summary of Sb spectroscopy. The text displayed in bold face corresponds to the optimal RILIS ionization scheme.

E_2 cm^{-1}	State II[b]	ν_2 cm^{-1}	λ_2 nm	Ion current (relative)	Power, mW[a] 1	2
60765.29	6p $(^3P_0, 1/2)_{1/2}$	14819.95	674.58	0.015	85	100
61000.30	6p $(^3P_0, 3/2)_{3/2}$	15054.96	664.05	0.12	110	300
62462.41	4f $(^3P_0, 3)_{5/2}$	16517.07	605.27	0.01	100	230
63606.31	7p $(^3P_1, 1/2)_{1/2}$	17660.97	566.06	0.3	-	240
63790.95	**7p $(^3P_1, 3/2)_{5/2}$**	**17845.61**	**560.21**	**1**	**60**	**300**
63798.45	7p $(^3P_1, 1/2)_{3/2}$	17853.11	559.97	0.88	-	-
63900.53	7p $(^3P_1, 3/2)_{3/2}$	17955.19	556.79	0.58	-	800
64098.36	8p $(^3P_0, 1/2)_{1/2}$	18153.02	550.72	0.14	-	600
64209.43	7p $(^3P_1, 3/2)_{1/2}$	18264.09	547.37	0.16	-	120
64273.86	8p $(^3P_0, 3/2)_{3/2}$	18328.52	545.45	0.08	-	90

$E_0 = 5s^25p^3\ ^4S_{3/2}$, 0 cm^{-1}; $E_1 = 5s^25p^26s(^3P)\ ^4P_{3/2}$, 45945.34 cm^{-1}

[a] The laser power values given in the tables are as measured on the laser table. Transmission to the ion source is approximately 20 % for the first-step, 50 % for the second-step and 50 % for the CVL beam (third-step). The power of the CVL beam used for the non-resonant ionization step was 18 W.

[b] $L_2 - j$ notation.

Ten transitions from the $5p^26s(^3P)\ ^4P_{3/2}$ excited state to known higher atomic levels (60765-64274 cm^{-1} [42]) were observed in the wavelength range of 545 - 675 nm. The remainder of the 511 nm component of the CVL beam was transferred to the ion source for the ionization step. The measurement of the ion current determined the optimal second-step transition of 17845.61 cm^{-1} to

the $5s^25p^27p(^3P_1,\ 3/2)_{5/2}$ level at 63790.95 cm^{-1}. The laser power generated at this wavelength was between 200 and 300 mW, at least two times greater than the saturation power of approximately 100 mW (Figure 6.3). With an ionization potential of 8.61 eV, surface ionized antimony is not produced within the hot cavity and so the lasers remained on during the mass marker evaporation. From the evaporation of the mass marker the RILIS efficiency was measured to be 2.7 %.

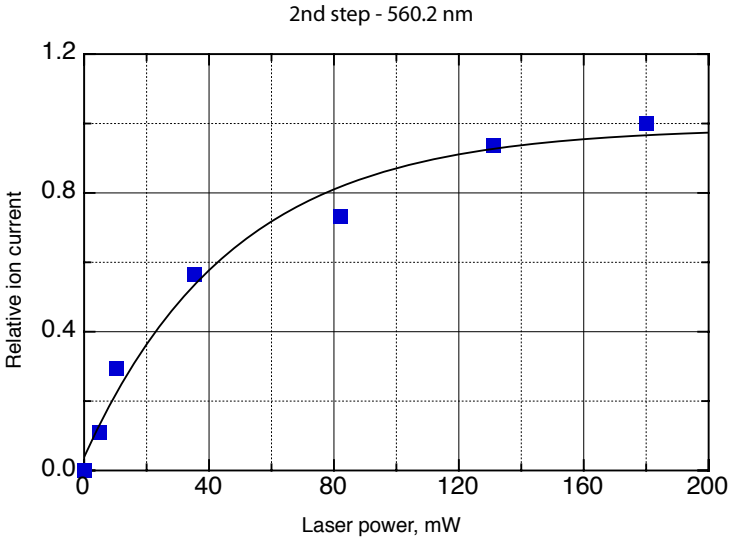

Figure 6.3: Saturation of the second-step transition for the new Sb scheme.

6.3 Dysprosium

The $4f^{10}\ 6s^2\ ^5I_8$ ground-state of Dy is 93 % populated in the ionizer cavity at 2300 K and 12 accessible excited states exist between 13500 and 18500 cm^{-1}, corresponding to a photon transition in the visible region, within the tuning range of the fundamental beam from the dye laser. Using the Phenoaxazone 9 dye pumped with the 578 nm component of the CVL beam, schemes using three of these levels close to 15500 cm^{-1} were tested. For transitions from these levels, 88 second excited states are documented. Using the 511 nm component

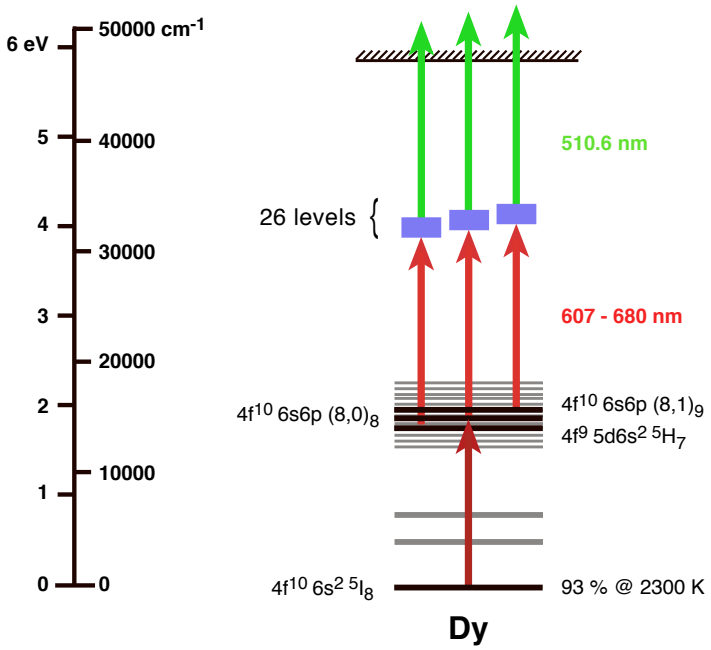

Figure 6.4: Extent of the Dy RIS study.

of the CVL beam for non-resonant ionization and by scanning the second-step frequency over the spectral range of the Phenoaxazone 9 and DCM dyes (607 - 680 nm), measurements of the relative performance of schemes using 19 of the known second excited states, and also seven new levels, were carried out. In total, 35 ionization schemes were studied, the details of which are given in Table 6.2. Saturation of the three first-step and four of the second-step transitions corresponding to the strongest schemes was confirmed (Figure 6.6). The optimal scheme (shown in Figure 6.1) gave a laser/surface ion ratio of close to 60 with the target and line heating at 500 A and 310 A respectively. These measurements were carried out for the isotope ^{162}Dy.

Dy has seven stable isotopes from mass 156 - 164 and readily forms an oxide (DyO) or a fluoride (DyF). The corresponding isotope and molecular masses were selected in turn at the GPS separator and the relative yields of each were measured (Figure 6.5). Measurements of the relative yield of each isotope show

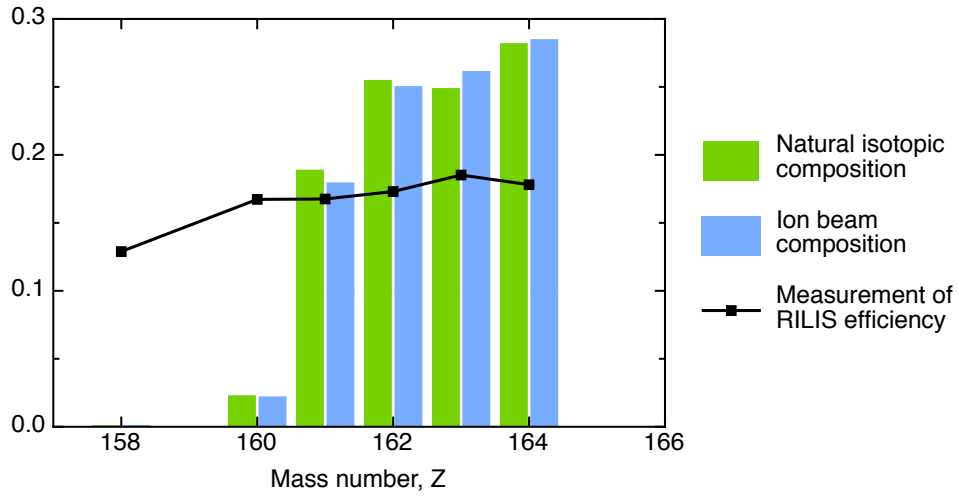

Figure 6.5: The relative RILIS efficiency across the Dy stable isotope chain.

a close agreement with the natural isotopic composition of dysprosium. It may therefore be inferred that the isotope-shift of the atomic transition is not large enough to necessitate an adjustment of the laser-frequency across the isotope chain. A drop in the measured laser/surface ion ratio for ^{158}Dy is seen but can be attributed to the low yield for this less abundant isotope, where a small positive offset in the ion current measurement can form a significant portion of the signal size.

For the efficiency measurement a 300μg Dy sample (12.62 μAh ^{162}Dy) was evaporated at a line heating of 300 A and with the lasers turned off. During the evaporation the target heating current was increased from 500 to 820 A. The corresponding increase in target temperature not only results in a greater vapour pressure of Dy, but can also give rise to significant secondary heating of the ion source cavity (line). As has been discussed, the surface ionization efficiency and the RILIS ion extraction efficiency are both proportional to the line temperature. This effect must be considered and can be quantified by measuring the $I_{laser}/I_{surface}$ as a function of target and line heating current. Such measurements are shown in Figure 6.7.

Figure 6.8 shows the ionic charge accumulation by surface ionization during the sample evaporation. Also shown is a plot of the expected charge accumulation by laser ionization, calculated by multiplication of the surface ion current by a

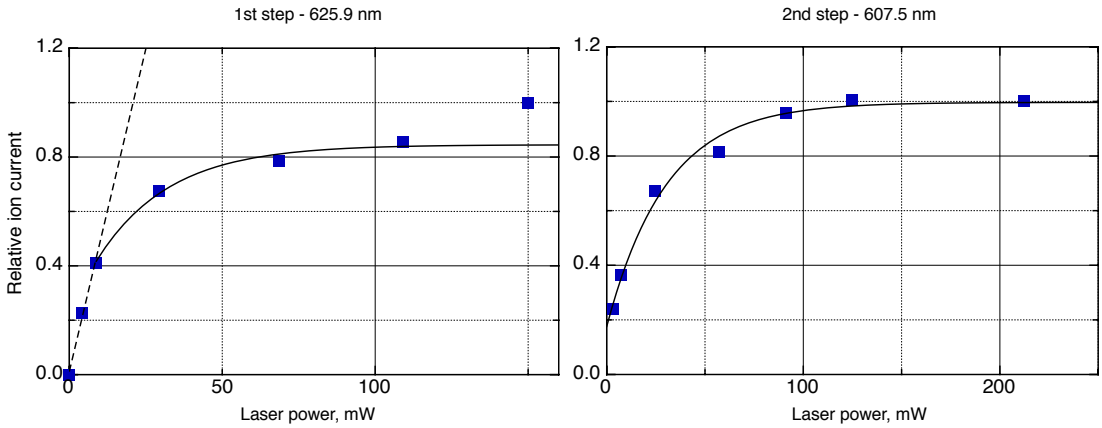

Figure 6.6: Saturation of the first- and second-step transitions for the new Dy scheme.

Table 6.2: A - Three-step ionization schemes for Dy.

E_2 cm^{-1}	State II	ν_2 cm^{-1}	λ_2 (air) nm	Laser power, mW 1	2	Las/Surf Ion Ratio
30979.48	$4f^{10}$ $6s7s(8, 1)_8$[a]	15784.70	633.35	200	300	0.51
30988.16	J=6	15793.42	633.00	200	300	1.21
31180.01	J=6	15985.18	625.41	200	600	0.27
31362.62	J=7	16167.79	618.34	200	1000	7.82
31423.04	J=7	16228.21	616.04	200	950	0.83
31469.00	J=8	16274.17	614.30	200	1100	8.8
31471.44	new	16276.61	614.21	200	1000	6.4
31509.07	$4f^{10}$ $6s7s(8, 1)_7$[a]	16314.24	612.79	200	950	2.98
31544.68	new	16349.85	611.46	900	1000	16.45
31619.03	new	16424.20	608.69	200	800	8.8
31654.20	new	16459.37	607.39	200	650	0.29
31674.01	J=7	16479.18	606.66	200	550	5.86
31684.36	new	16489.53	606.28	200	500	9.78

$E_0 = 4f^{10}\ 6s^2\ {}^5I_8$, 0 cm^{-1}; $E_1 = 4f^9\ 5d6s^2\ {}^5H_7$, 15194.83 cm^{-1}

[a] $j-j$ notation.

varying laser/surface ion ratio appropriate to the target and line temperature at each stage of the evaporation. 0.4 % of the sample was collected after surface

Table 6.2: B - Three-step ionization schemes for Dy.

E_2 cm^{-1}	State II	ν_2 cm^{-1}	λ_2 (air) nm	Laser power, mW 1	2	Las/Surf Ion Ratio
31362.62	J=7	15795.24	632.93	1100	300	4.19
31423.04	J=7	15855.66	630.52	1100	450	6.16
31469.00	J=8	15901.62	628.69	1100	520	3.46
31509.12	$4f^{10}$ 6s7s(8, 1)$_7$[a]	15941.74	627.11	1100	600	7.93
31654.34	new	16086.96	621.45	1100	900	0.22
31674.08	J=7	16106.70	620.69	1100	950	0.91
31694.88	new	16127.50	619.89	1100	1000	0.47
31775.65	J=9	16208.27	616.80	1100	1000	26.27
31820.28	J=8	16252.90	615.10	1100	1100	2.11
32036.51	J=7	16469.13	607.03	1100	600	13.42

$E_0 = 4f^{10}\ 6s^2\ {}^5I_8$, 0 cm^{-1}; $E_1 = 4f^{10}$ 6s6p $(8,0)_8$, 15567.38 cm^{-1}

[a] $j-j$ notation.

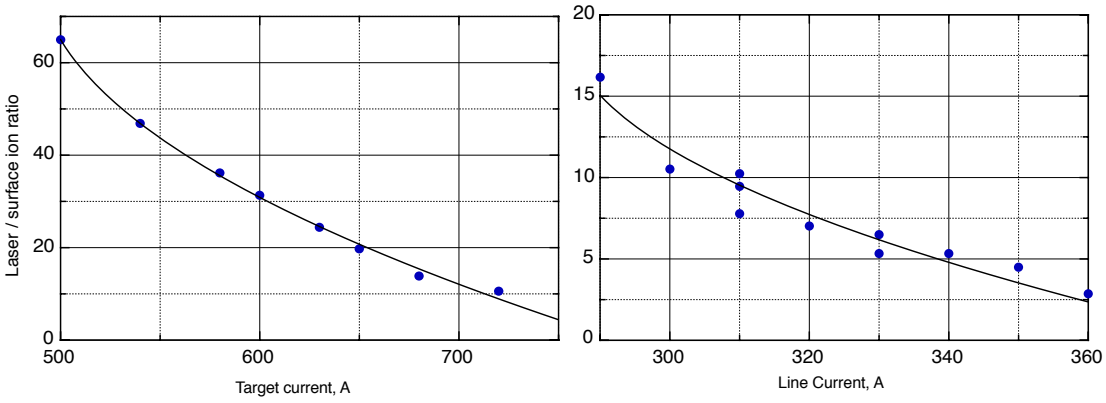

Figure 6.7: Effect of the target and line heating on the RILIS performance.

ionization and the RILIS efficiency was evaluated as 20 % using Equation 6.1.

6.4 Gold

For this work, a standard ISOLDE target was used with a tungsten surface ionizer cavity. The target/ion source unit was equipped with two ovens. A large Au sample was placed in one of these for use during the initial spectroscopy study and

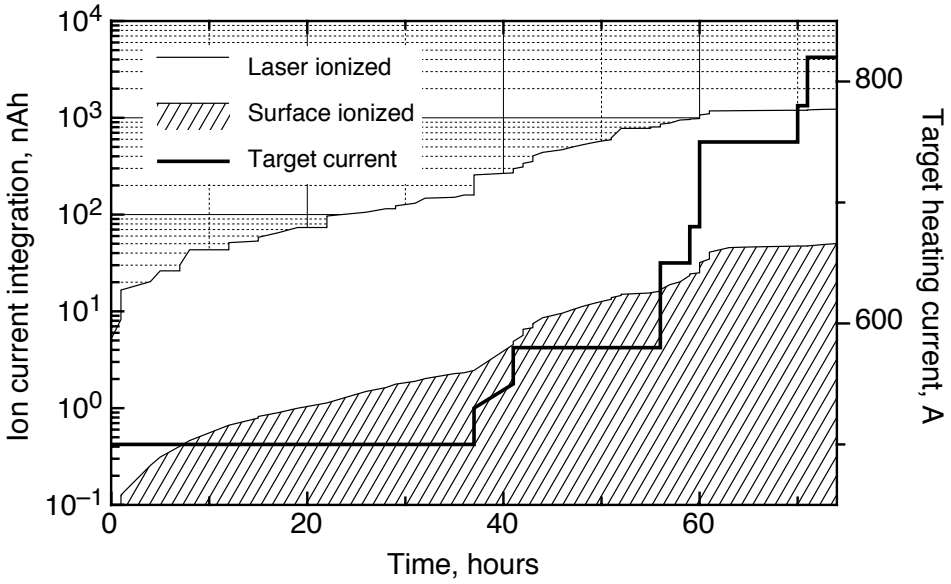

Figure 6.8: The Dy mass marker evaporation during the efficiency measurement.

ionization scheme search. The second oven was loaded with a precise 3000 nAh Au sample, for use during the final efficiency measurement. The mass separator was tuned to the mass of ^{197}Au and the transmitted ion current was monitored on a Faraday cup detector.

Data on atomic lines and energy levels for Au are taken from the Kurucz atomic line database [40]. The ionization potential for gold (9.23 eV) is high with respect to the photon energy-range attainable with RILIS ($\sim$ 1.7 - 5 eV). As a result, ionization schemes using three excitation steps were investigated. For the first-step, the transitions from the ground-state 6s $^2S_{1/2}$ level to the 6p $^2P_{1/2}$ and 6p $^2P_{3/2}$ levels at 37358.991 cm^{-1} and 41174.613 cm^{-1} respectively are the only known transitions that can be reached with the RILIS laser system. Both transitions are strong and of similar strength ($A_k = 1.65\times 10^8$ s^{-1} and 1.96×10^8 s^{-1} [40]). Frequency tripling is required to generate the 242.9 nm light required to populate the 41174.61 cm^{-1} level. Due to the low conversion efficiency of third-harmonic generation, a large proportion of the CVL pump beam power would be required in order to attain the dye-laser power required at the fundamental

frequency. The transition to the lower-lying, $^2P_{1/2}$ level is preferable since the transition energy, 37358.991 cm^{-1}, corresponds to that of a 267.673 nm photon, accessible by second-harmonic generation of light at 535.198 nm. This falls within the emission range of the Pyrromethene 546 dye, which is pumped with the 511 nm component of the CVL beam. Measurements were carried out using only this transition for the first-step in the excitation scheme.

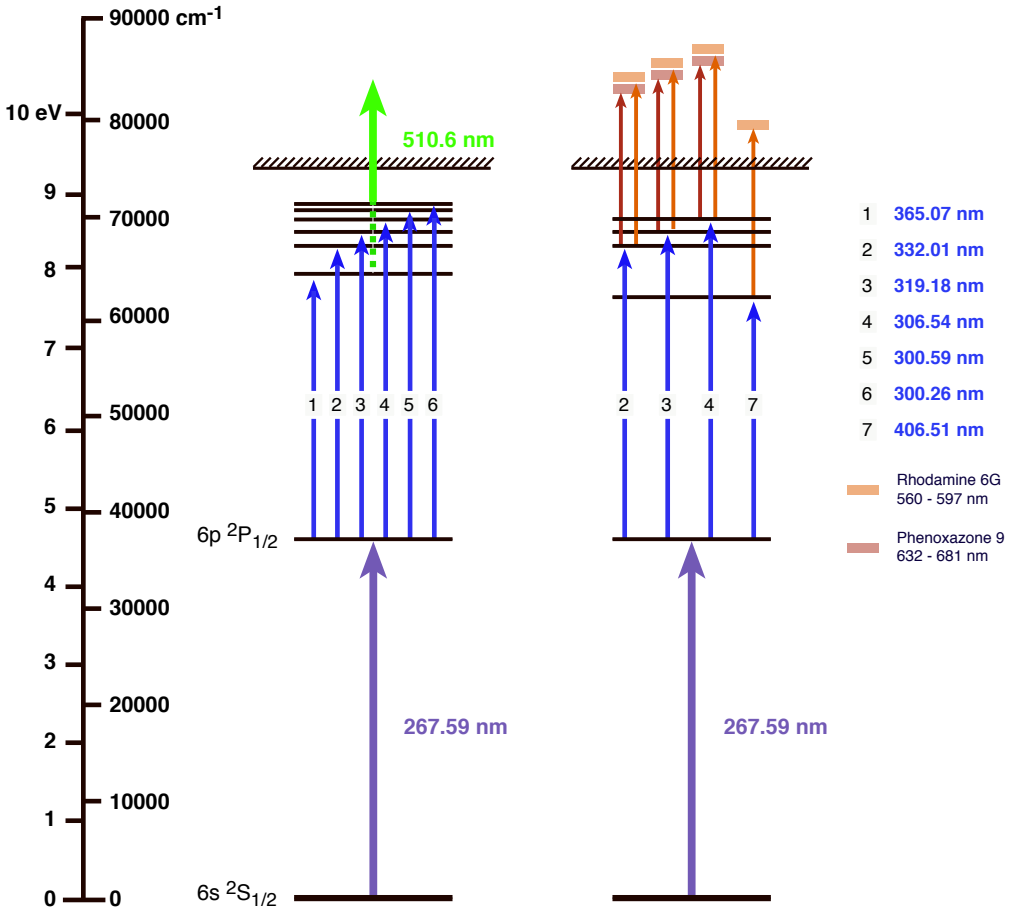

Figure 6.9: Extent of the Au RIS study.

From this first excited state, 11 potential second excited states from 54485 cm^{-1} to 72164 cm^{-1} are documented [40]. All but the lowest lying of these excited states exist at an energy of less than 19581 cm^{-1} below the continuum, meaning that ionization from these levels is possible via non-resonant absorption of a 511

nm photon, provided by the CVL. Accessing any of these ten transitions requires second-harmonic generation of the fundamental dye-laser output, and hence, a significant proportion of CVL pump power. It is preferable to use all of the CVL pump power at 511 nm for the generation of the frequency for the first transition and for the final ionization stage, leaving only the 578 nm component for the second-step. Therefore, we have limited our study to the group of six second-step transitions (Figure 6.9), which are accessible with a frequency-doubled dye laser pumped with light at 578 nm. The pumping requirements of the dye lasers and amplifiers for the first- and second-step transitions were met using the total output from one of the two CVL amplifiers after separation of the 578 nm and 511 nm components. Typical values of the average power for this CVL beam were 22 W and 20 W at 511 nm and 578 nm respectively. The second CVL amplifier output power was 27 W (in both components), all of which was used for the last excitation step.

As the first stage of this study, schemes using three-step ionization with a non-resonant transition to the continuum (induced by both components of the CVL beam) were studied. An ion current of gold was observed in the presence of only the beam for the first-step in the excitation scheme. Since the ionization threshold of Au (74409.0(2) cm^{-1} [43]) is slightly less than the sum of the energies of two photons at 267.673 nm, this ion current is attributed to the occurrence of two-step ionization via a transition to the continuum from the first excited state by non-resonant absorption of second photon from the first-step beam, The presence of this laser-ionized ion signal facilitated a reliable optimization of the beam focusing and positioning. In addition, the measurements of the ion current produced by the first-step transition beam provided a useful reference point for use in the evaluation of the relative efficiencies of ionization schemes. The ratio of ion current produced with three laser beams versus ion current produced by the first-step beam $\mathbf{R} = \mathbf{I}_{1+2+3}/\mathbf{I}_{1+3}$ is taken as an efficiency parameter of the ionization scheme. In order to keep thermal conditions of laser beam transport optics constant these measurements were carried out whilst blocking only the beam of second-step laser, leaving the most powerful laser beam (from the second CVL amplifier) propagating toward the ion source. This beam did not participate

in the ionization process because its photon energy was less than is required for transition from the first excited state to the ionization continuum.

For the second phase of the study a search for auto-ionizing states (AIS) was conducted. The CVL power used for the ionization stage was diverted to pump a third dye laser and dye amplifier. Ethanol solutions of the laser dyes Rhodamine 6G and Phenoxazone 9 were used in this laser, the wavelength was scanned across the ranges 560-597 nm and 632-681 nm respectively. When an observable increase of the ion current was detected, scanning was stopped and the wavelength was optimized to the maximal value of the ion current. Its peak value, corresponding transition frequency, and values of laser power for each of three beams were recorded. Measurements of the laser frequency were made using a HighFinesse / Ångstrom model WS/7 wavemeter. The accuracy of the transition frequency measurements was defined by the width of resonance and laser line width ($\sim$ 0.6 cm^{-1}). For narrow AIS it was possible to define the peak position with an accuracy of close to 0.1 cm^{-1}. Energy regions above the ionization threshold for the transitions from the second excited states corresponding to the four strongest second-step transitions were studied.

A summary of these measurements is given in Table 6.3. Within the energy intervals that were studied, five auto-ionizing states (AIS) had been previously observed [44],[45], but not as resonant transitions from the excited states measured during this study. Three of the known AIS were confirmed and 27 new AIS were observed. Figure 6.10 shows the profiles of the resonances for the two strongest AIS, at 84806.3 cm^{-1}(a) and 84880.4 cm^{-1}(b).

Of particular interest was the measurement of a previously applied ionization scheme for Au [41]. This scheme, shown in italics in Table 6.3, was one of the more efficient schemes previously documented however our new optimal scheme, shown on the right-hand side of Figure 6.1, gives a factor of 4-5 increase in the efficiency parameter **R**. The saturation measurements for the first- and second-steps in this scheme are presented in Figure 6.11, they confirm that the saturation points for the transitions are exceeded with the laser power available.

For the measurement of the absolute value of ionization efficiency, some experimental difficulties were encountered, limiting the reliability of the assessment

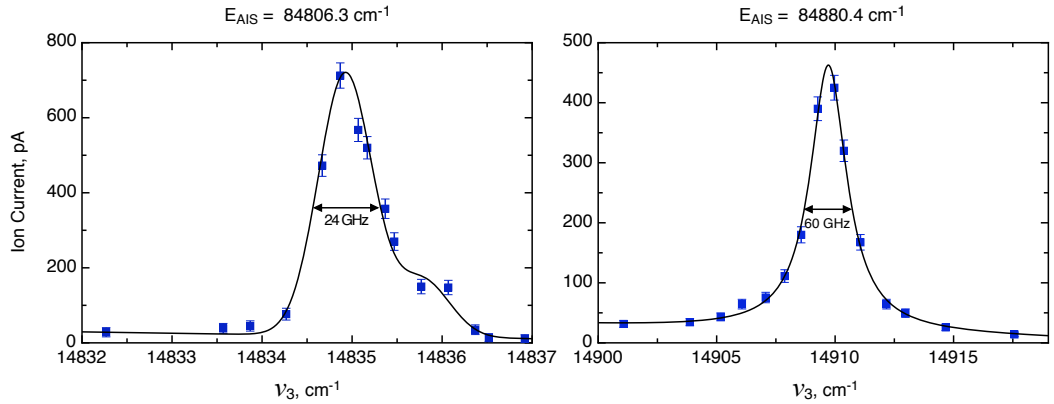

Figure 6.10: The two strongest AIS observed during the Au study.

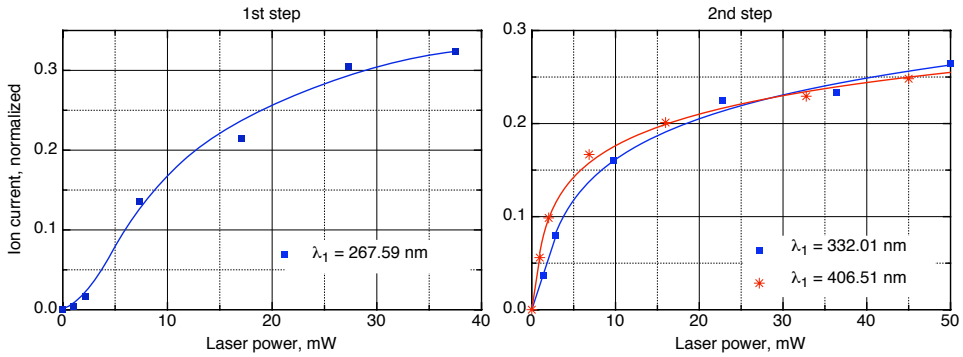

Figure 6.11: Saturation curves for the resonant transitions of the most efficient Au schemes.

of the mass marker evaporation. During the initial search for a resonance ionization signal, a large quantity of the Au sample was evaporated from the first oven. After detection of the ion signal, the subsequent tests were carried out without the need to heat the mass marker itself, evaporation of the gold that had condensed in the target container provided a sufficient and steady supply of gold vapor for the duration of the spectroscopic work. An attempt was made to extinguish this supply by gradually increasing the target heating from 570 - 700 A. A small decrease in the ion current was observed after some hours. The evaporation of the 3000 nAh mass marker was then carried out with the target heating kept at 700 A. For improved laser ionization stability and experimental ease, only the first-step laser was used for ionization during the efficiency mea-

surement. The ionization efficiency of the Au scheme presented in Figure 6.1 was estimated to be over 3% by comparing the product of the ion current integration and the parameter **R** of the most efficient ionization scheme with the original sample size.

6.5 Scandium

Scandium has a 3d 4s^2 ^{2}D$_{3/2}$ ground-state and a low-lying ^{2}D$_{5/2}$ excited state at 168.34 cm^{-1}. In the ionizer cavity at a temperature of 2300 K, the excited state is 57.4% populated and so the spectroscopy study considered first-step transitions from this level only. Due to the abundance of second-step transitions and for convenience in terms of wavelength tuning, a first-step transition to the 3d4s(^{3}D)4p^{2}P$_{3/2}$ state at 30706.66 cm^{-1} was chosen. The transition wavelength required (327.36 nm) was generated by frequency-doubling of the fundamental laser-frequency output from the dye laser using Phenoaxazone 9 dye pumped by the 578 nm component of the CVL beam.

The RIS work involved scanning the second-step frequency to study the energy level range 44030 - 49210 cm^{-1}. Five laser dyes (DCM, R110, R700, Pyyromthene 597 and Phenoaxazone 9) were required and within this region 30 new transitions were observed and 27 of the 39 documented transitions [40] from the ^{2}P$_{3/2}$ level were also seen. A summary is given in Table 6.4. Highlighted in bold is the most efficient scheme, as judged by the laser on/laser off ion ratio and corresponding to a second-step transition to the 3d4p^2 ^{2}P$_{3/2}$ level at 44594.57 cm^{-1}. The saturation measurements for the first and second-steps (Figure 6.15) show that the transitions are saturated, confirming that the greatest RILIS efficiency can be achieved with the Sc scheme shown in Figure 6.1 which gives a $I_{laser}/I_{surface}$ value of 400 at typical target and line temperatures.

For the efficiency measurement the lasers were not used and the sample was surface ionized in the hot cavity. The complete sample evaporation required a large increase in the target temperature (from 500 A to 830 A) and almost 0.1 % of the 1650 nAh sample was collected. Due to secondary heating of the ionizer cavity (by conduction and radiation from the target), the $I_{laser}/I_{surface}$ value of 400 (Table 6.4), measured at a target current of 570 A, is not a reliable

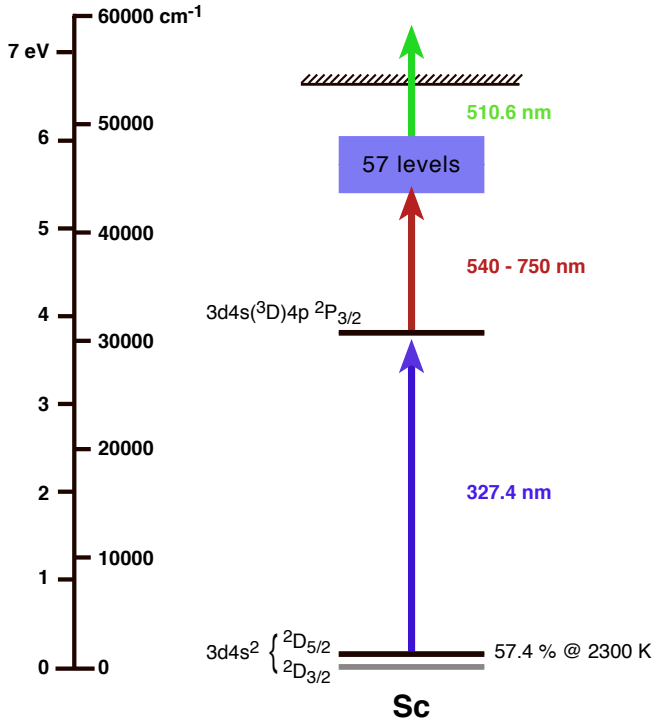

Figure 6.12: Extent of the Sc RIS study.

factor for use in calculating the RILIS efficiency. Although the dependence of the $I_{laser}/I_{surface}$ on the target temperature was not measured for scandium, this effect was measured as part of the off-line spectroscopy work for dysprosium (Figure 6.7). A 50 % reduction in the $I_{laser}/I_{surface}$ was observed with a 150 A increase in the target temperature.

In Figure 6.13 the estimated target-temperature-dependent $I_{laser}/I_{surface}$ values for Sc are plotted. These values were calculated by an adjusting the measured $I_{laser}/I_{surface}$ of 400 given in Table 6.4 using the exponential dependence on the target heating current that was observed for Dy. Until a more thorough investigation is carried out, the RILIS efficiency for Sc is determined using these values. Also shown in Figure 6.13 is the fluctuation of the ion current by surface ionization during the sample evaporation. Figure 6.14 shows the surface ion current integration and the final efficiency, given as a percentage of the original sample

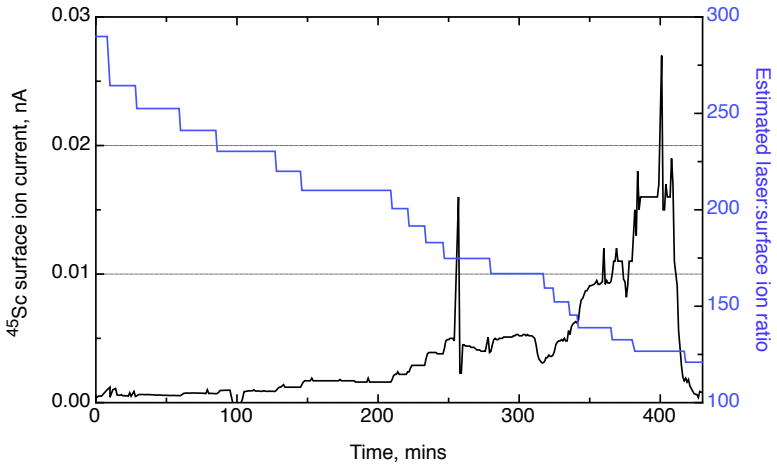

Figure 6.13: Sc mass marker evaporation plot showing also the estimated $I_{laser}/I_{surface}$ values.

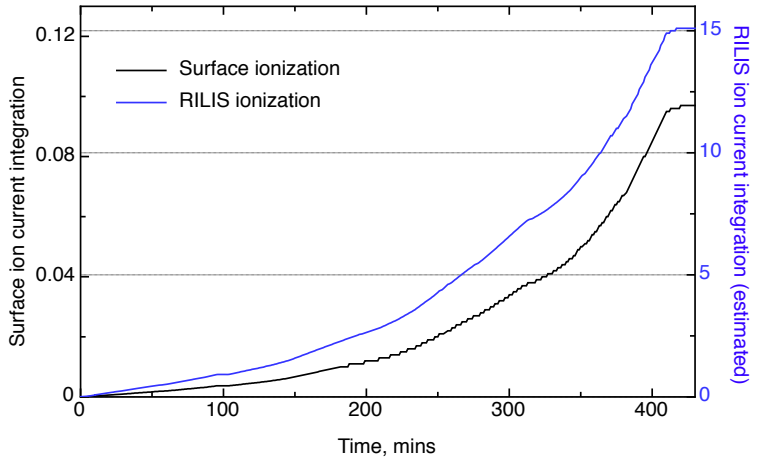

Figure 6.14: Ion current accumulation as a percentage of the original sample size. The RILIS ion current integration was calculated using the variable laser/surface ion ratio shown in Figure 6.13.

size. The second line in the figure shows the estimate of the RILIS efficiency calculated using the variable laser/surface ion ratio from Figure 6.13. The RILIS efficiency is estimated to be 15 %.

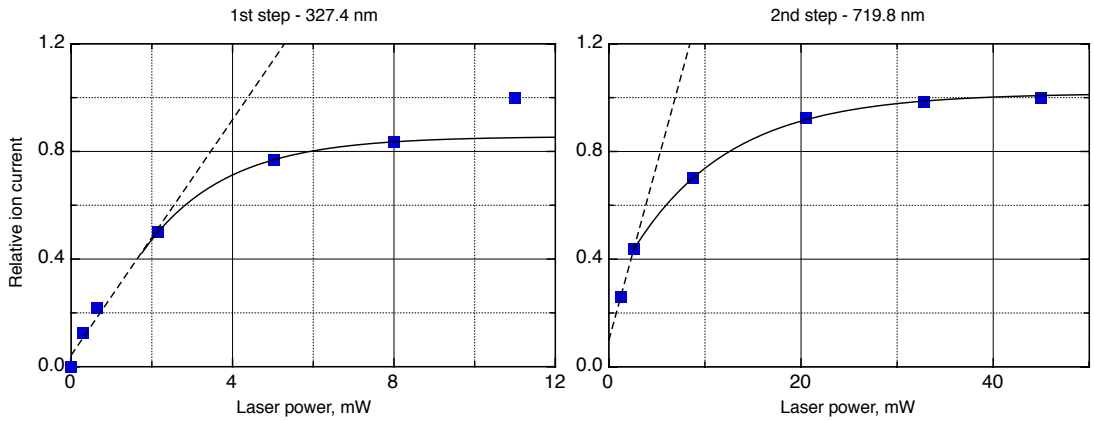

Figure 6.15: Saturation of the first- and second-step transitions for the new Sc scheme. The final datum in the plot on the left is dismissed in the fit since it represents the ion current with the laser beam attenuator completely removed and so the beam shape is slightly altered.

6.6 Yttrium

The structure of atomic levels of yttrium is similar to that of scandium as both belong to the same group of the periodic table of elements. The ground-state of Y $4d5s^2\ ^2D$ is split on two levels with J=3/2 and 5/2, where the $4d\ 5s^2\ ^2D_{5/2}$ excited state, lies at an energy of 530.36 cm^{-1} above the zero energy level and is 52% populated. The available data on the atomic transition probabilities of yttrium [46] presents a choice of first-step transitions for the resonance ionization. Schemes using relatively strong transitions from each of these levels to five first excited states with the electronic configuration 4d5s5p between 24100 and 25000 cm^{-1} (407 - 415 nm) were tested during the RIS study. By scanning the second-step within the wavelength range of 565 - 617 nm, 45 highly excited states were observed in the energy range of 39000 - 43400 cm^{-1}. Only eight of these levels were documented in the atomic energy level tables [47].

Laser ion/surface ion ratios were measured for 72 schemes, details of which are given in Tables 6.5A - 6.5E. The saturation power for the chosen first-step transition was approximately 10 mW, an order of magnitude lower than the power available during the measurements.

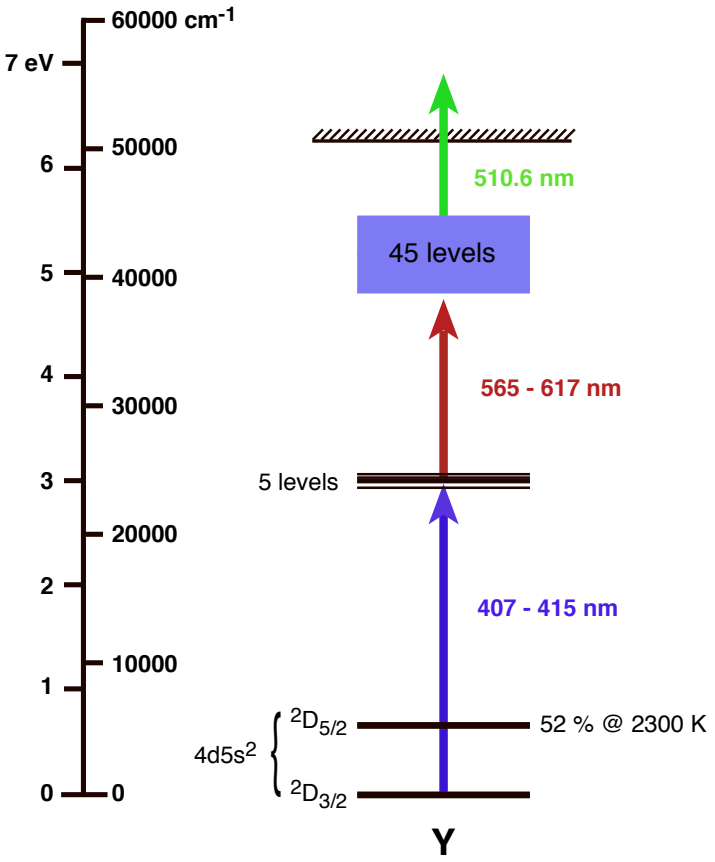

Figure 6.16: Extent of the Y RIS study.

6.7 Conclusions and Future Work

With the development of these new ionization schemes, the RILIS can now provide a means of efficient and selective ionization of 27 of the elements. In accordance with the requirements of the ISOLDE experimental program, new schemes will continue to be developed for RILIS using procedures similar to those described in this work. Currently, such studies have to fit into the framework of general ISOLDE off-line development and thus, the dedicated mass separator use required is limited to just a few weeks per year. A recent letter of intent addressed to the ISOLDE INTC committee gives details of a new and dedicated RILIS research laboratory. Following the completion of this laboratory, the investigation of new

ionization schemes will become a task that is independent of ISOLDE scheduling. Many of the RILIS ionization schemes rely on an inefficient final step of non-resonant ionization using a large proportion of the total CVL power. It is hoped that the time consuming search for auto-ionizing states for many of these elements could be carried out in this laboratory and significant improvements in RILIS efficiency could be made.

Table 6.3: Three-step ionization schemes for Au. The text in italics and bold face correspond to the scheme used in [41] and the optimal RILIS scheme respectively. **R** is the efficiency parameter defined in Section 6.4.

λ_2 (air) nm	E_2 cm-1	State II	λ_3 (air) nm	E_3 cm-1	Laser Power, mW 2	3	**R** $\mathbf{I_{1+2+3}/I_{1+3}}$
365.07	64742.9	8s $^2S_{1/2}$	511, 578	Continuum	75	10000	1
332.01	67469.68	7d $^2D_{3/2}$	511, 578	Continuum	75	10000	9.6
319.18	68680.63	9s $^2S_{1/2}$	511, 578	Continuum	60	10000	2.1
306.54	69971.42	8d $^2D_{3/2}$	511, 578	Continuum	75	11000	7.7
300.59	70617.73	10s $^2S_{1/2}$	511, 578	Continuum	65	11000	1.5
300.26	70653.25	J=3/2	511, 578	Continuum	65	11000	1.2
406.51	*61951.89*	*6d $^2D_{3/2}$*	*591.90*	*78842.0*	*75*	*625*	*55*
319.18	68680.63	9s $^2S_{1/2}$	668.65	83631.9	90	1130	4.4
319.18	68680.63	9s $^2S_{1/2}$	644.93	84181.9	90	1130	3.1
332.01	67469.68	7d $^2D_{3/2}$	592.85	84332.8	90	500	10
332.01	67469.68	7d $^2D_{3/2}$	584.84	84563.8	90	750	6.4
332.01	67469.68	7d $^2D_{3/2}$	578.38	84754.5	90	550	73
306.54	69971.42	8d $^2D_{3/2}$	676.27	84754.3	80	750	150
332.01	67469.68	7d $^2D_{3/2}$	576.64	84806.6	90	950	120
306.54	**69971.42**	**8d $^2D_{3/2}$**	**673.9**	**84806.3**	**80**	**750**	**220**
332.01	67469.68	7d $^2D_{3/2}$	574.20	84880.5	90	750	34
306.54	69971.42	8d $^2D_{3/2}$	670.55	84880.4	80	1000	180
306.54	69971.42	8d $^2D_{3/2}$	666.24	84976.9	80	1130	13
332.01	67469.68	7d $^2D_{3/2}$	570.77	84985.0	90	750	2.6
306.54	69971.42	8d $^2D_{3/2}$	665.81	84986.6	80	1130	38
332.01	67469.68	7d $^2D_{3/2}$	569.80	85014.7	90	975	3.5
332.01	67469.68	7d $^2D_{3/2}$	567.24	85094.1	90	600	4.5
306.54	69971.42	8d $^2D_{3/2}$	661.08	85093.9	80	1250	21
332.01	67469.68	7d $^2D_{3/2}$	567.12	85097.8	90	600	5.4
306.54	69971.42	8d $^2D_{3/2}$	660.90	85098.0	80	1250	20
332.01	67469.68	7d $^2D_{3/2}$	564.14	85190.8	90	450	3.3
306.54	69971.42	8d $^2D_{3/2}$	632.80	85769.9	80	500	4.3
319.18	68680.63	9s $^2S_{1/2}$	567.39	86300.3	80	750	4.5
319.18	68680.63	9s $^2S_{1/2}$	565.61	86355.6	85	625	3.8
319.18	68680.63	9s $^2S_{1/2}$	565.36	86363.5	85	625	3.6
306.54	69971.42	8d $^2D_{3/2}$	575.60	87339.7	85	750	76
306.54	69971.42	8d $^2D_{3/2}$	572.38	87437.6	85	750	59
306.54	69971.42	8d $^2D_{3/2}$	570.70	87488.4	85	750	59
306.54	69971.42	8d $^2D_{3/2}$	567.98	87572.8	85	700	44
306.54	69971.42	8d $^2D_{3/2}$	567.14	87598.7	85	550	7.4
306.54	69971.42	8d $^2D_{3/2}$	564.07	87694.9	85	550	15
306.54	69971.42	8d $^2D_{3/2}$	561.71	87769.1	85	375	4.3

E_0 = 6s $^2S_{1/2}$, 0 cm^{-1}; E_1 = 6p $^2P_{1/2}$, 37358.99 cm^{-1}

Table 6.4: Three-step ionization schemes for Sc. The text in bold face corresponds to the optimal RILIS ionization scheme.

E_2 cm^{-1}	State II	ν_2 cm^{-1}	λ_2 nm	Laser power, mW 1	2	3	Las/Surf Ion Ratio
44060.44	new	13353.8	748.65	-	170	1000	5.5
44496.16	new	13789.5	724.99	-	240	-	41.7
44594.97	**3d4p^2 ^{2}P$_{3/2}$**	**13888.3**	**719.83**	**200**	**200**	**1000**	**400**
44690.65	3d4p^2 ^{2}P$_{3/2}$	13984.0	714.91	-	200	-	352.9
45514.98	3d4s4d ^{2}S$_{1/2}$	14808.3	675.11	70	60	1000	216.7
45672.16	new	14965.5	668.02	-	170	-	120.7
45764.56	new	15057.9	663.92	-	-	-	36
45824.26	new	15117.6	661.30	-	90	900	28.3
45866.86	new	15160.2	659.44	-	100	900	41.7
46027.56	new	15320.9	652.52	-	140	-	-
46563.76	new	15857.1	630.46	-	130	-	-
46652.96	new	15946.3	626.93	-	110	-	51.9
46825.26	new	16118.6	620.23	-	70	1000	42.3
46924.76	new	16218.1	616.42	-	70	1000	92
47425.46	^{2}D$_{5/2}$	16718.8	597.96	-	120	900	125
47588.36	new	16881.7	592.19	-	150	950	161.8
47626.46	new	16919.8	590.86	90	120	1000	448.3
47723.96	new	17017.3	587.47	-	170	900	84.4
47761.86	new	17055.2	586.17	-	170	800	20.3
47783.86	new	17077.2	585.41	-	150	800	243.3
47794.36	new	17087.7	585.05	-	150	800	106.5
47998.76	new	17292.1	578.14	-	200	900	77.4
48065.46	new	17358.8	575.92	-	320	1000	121.6
48065.76	new	17359.1	575.91	-	150	800	173.3
48065.76	new	17359.1	575.91	100	130	800	250
48107.76	new	17401.1	574.52	-	320	1000	114.3
48229.56	new	17522.9	570.52	-	100	1000	39.1
48229.66	new	17523	570.52	70	300	1000	59.1
48490.16	new	17783.5	562.16	100	200	1000	325.6
48920.60	^{4}P$_{5/2}$	18213.94	548.88	-	190	1000	5
48975.46	new	18268.8	547.23	-	160	1000	7.5
49069.96	new	18363.3	544.41	-	120	1000	13.5
49146.46	new	18439.8	542.15	-	100	1000	12.4

E_0 = 3d 4s^2 ^{2}D$_{5/2}$, 168.34 cm^{-1} *(57% @ 2400 K)*; E_1 = 3d4s(^{3}D)4p ^{2}P$_{3/2}$, 30706.66 $cm^{-}1$

Table 6.5: A - Three-step ionization schemes for Y.

E_2 cm^{-1}	State II	ν_2 cm^{-1}	λ_2 (air) nm	Laser power, mW 1	2	Las/Surf Ion Ratio
39001.4	new	14870.2	672.30	110	250	8.7
39087.2	new	14956.0	668.44	110	400	5.7
39209.3	new	15078.1	663.03	110	500	12.9
39224.4	new	15093.2	662.37	110	600	88.4
39313.2	new	15182.0	658.50	110	740	51.8
39446.3	4d5s5d $e^4F_{3/2}$	15315	652.77	110	750	22.1
39553.0	new	15421.8	648.25	110	900	22.3
39565.1	4d5s5d $e^4F_{5/2}$	15433.8	647.75	110	870	24.3
39686.0	new	15554.8	642.71	110	920	30.9
40287.6	new	16156.4	618.78	110	720	9.4
40307.7	new	16176.5	544.41	110	700	11.5
41423.1	new	17291.9	578.15	110	1200	25.8
41660.3	new	17529.1	570.32	110	1600	32.9
41660.3	new	17529.1	570.32	110	1400	31.2
41669.5	new	17538.3	570.02	110	1500	16.1
41853.3	new	17722.1	564.11	110	1400	31.6
41879.9	new	17748.7	563.27	110	900	7
41992.8	new	17861.6	559.70	110	700	2.3

$E_0 = 0$ cm^{-1}; $E_1 = 24131.2$ cm^{-1}; State I = 4d5s5p $y^2D_{3/2}$

Table 6.5: B - Three-step ionization schemes for Y.

E_2 cm^{-1}	State II	ν_2 cm^{-1}	λ_2 (air) nm	Laser power, mW 1	2	Las/Surf Ion Ratio
39313.2	new	14832.6	674.01	170	200	22
39322.1	new	14841.5	673.60	170	-	0.4
39446.3	4d5s5d $e^4F_{3/2}$	14965.7	668.01	170	400	16.5
39552.8	new	15072.2	663.29	170	440	15.8
39565.1	4d5s5d $e^4F_{5/2}$	15084.2	662.76	170	400	13.5
39686.0	new	15205.4	657.48	170	640	17.6
40287.6	new	15807.0	632.46	170	840	13.5
40307.7	new	15827.1	631.65	170	940	14.1
40455.1	4d5s5d $f^4P_{3/2}$	15974.3	625.83	170	900	0.3
40517.1	4d5s5d $f^4P_{5/2}$	16036.35	623.41	170	800	16
41660.6	new	17180.0	581.91	140	780	40.1
41669.7	new	17189.1	581.60	140	-	31.9
41853.3	new	17372.7	575.46	140	1200	27
41880.3	new	17399.7	574.56	140	1300	16.1
42048.9	new	17568.3	569.05	140	1500	34.7
42098.5	new	17617.9	567.45	140	1400	41.9
42106.6	new	17626.0	567.19	140	1400	16.9
42135.0	new	17654.4	566.27	140	-	2.5
42171.0	new	17690.4	565.12	140	1300	11.9
42220.9	new	17740.3	563.53	140	1200	1.5
42253.3	new	17772.7	562.50	140	1100	39
42301.3	new	17820.7	560.99	140	800	1.1

$E_0 = 0$ cm^{-1}; $E_1 = 24480.60$ cm^{-1}; State I = 4d5s5p $y^2P_{3/2}$

Table 6.5: C - Three-step ionization schemes for Y.

E_2 cm^{-1}	State II	ν_2 cm^{-1}	λ_2 (air) nm	Laser power, mW 1	2	Las/Surf Ion Ratio
39313.2	new	14794.4	675.75	160	100	8.9
39446.3	4d5s5d $e^4F_{3/2}$	14927.5	669.72	160	300	11.1
39553	new	15034.2	664.97	160	520	17.1
39565.1	4d5s5d $e^4F_{5/2}$	15046.3	664.43	160	520	22.1
39686	new	15167.2	659.14	160	650	33.1
39757.8	4d5s5d $e^4F_{7/2}$	15239.1	656.03	160	800	9.9
40517.1	4d5s5d $f^4P_{5/2}$	15998.3	624.89	160	700	12.9

E_0 = 0 cm^{-1}; E_1 = 24518.80 cm^{-1}; State I = 4d5s5p $y^2F_{5/2}$

Table 6.5: D - Three-step ionization schemes for Y.

E_2 cm^{-1}	State II	ν_2 cm^{-1}	λ_2 (air) nm	Laser power, mW 1	2	Las/Surf Ion Ratio
39565.1	4d5s5d $e^4F_{5/3}$	14818.5	674.65	120	150	30.8
39686.0	new	14939.4	669.19	120	420	27.6
39757.8	4d5s5d $e^4F_{7/2}$	15011.2	665.99	120	600	8.6
40455.1	4d5s5d $f^4P_{3/2}$	15708.5	636.42	120	-	1.9
40517.1	4d5s5d $f^4P_{5/2}$	15770.5	633.92	120	1200	20.7
41722.4	new	16975.8	588.91	140	380	7.9
41853.3	new	17106.7	584.40	140	700	10.1
42048.8	new	17302.2	577.80	140	1200	16.4
42098.6	new	17352.0	576.14	140	-	24.5
42106.6	new	17360.0	575.88	140	1300	25.5
42220.8	new	17474.2	572.11	140	-	3.1
42253.6	new	17507.0	571.04	140	1500	23.7
42391.3	new	17644.7	566.59	140	1300	4.1
42487.9	new	17741.3	563.50	140	1200	13.5

E_0 = 530.36 cm^{-1}; E_1 = 24746.60 cm^{-1}; State I = 4d5s5p $y^2D_{5/2}$

Table 6.5: E - Three-step ionization schemes for Y.

E_2 cm^{-1}	State II	ν_2 cm^{-1}	λ_2 (air) nm	Laser power, mW 1	2	Las/Surf Ion Ratio
39686.0	new	14786.5	676.11	120	70	0.1
39757.8	4d5s5d $e^4F_{7/2}$	14858.3	672.84	120	260	0.9
39963.7	4d5s5d $e^4F_{9/2}$	15064.2	663.64	120	400	17.4
40189.2	new	15289.7	653.85	120	780	0.1
40429.9	new	15530.4	643.72	120	1100	0.2
40517.1	4d5s5d $f^4P_{5/2}$	15617.6	640.13	120	1200	2
42098.6	new	17199.1	581.26	110	810	29.5
42253.3	new	17353.8	576.08	110	-	1.6
42390.9	new	17491.4	571.55	110	-	5.3
42487.6	new	17588.1	568.41	110	-	28.1

E_0 = 530.36 cm^{-1}; E_1 = 24899.50 cm^{-1}; State I = 4d5s5p $y^2F_{7/2}$

Chapter 7

Simultaneous RIS and nuclear spectroscopy at RILIS

ISOLDE has three laser spectroscopy set-ups: COLLAPS, COMPLIS and RILIS. Details of each of these techniques are provided in a review of lasers in nuclear physics [48]. COLLAPS was originally reliant upon fluorescence detection of atoms or ions Doppler tuned to resonance with a co-propagating fixed frequency tunable CW dye laser. Using a 'collinear beams' geometry and with the low velocity spread of the 60 kV ISOLDE beam, this setup gives extremely high resolution, Doppler-free spectra, essential for the measurement of charge radii of light isotopes or for the accurate determination of the electric quadrupole or small magnetic dipole moments. For fluorescence measurements, the sensitivity of the COLLAPS technique is inhibited by the low fluorescence detection efficiency, and the large background signal from scattered laser light reaching the photo-multiplier detectors. The issue of sensitivity has been addressed to some extent through the use of the particle-detection techniques of β–NMR and β–asymmetry although this type of measurement is sensitive to ion-beam impurities and is only compatible with β-decaying isotopes with a short half life.

By performing Resonance Ionization Spectroscopy (RIS), where the signal is provided by ion detection, scattered laser light does not contribute to the signal background and the sensitivity is limited primarily by the ionization efficiency. For COMPLIS [49][50], the ISOLDE ion beam (either surface, laser or electron impact ionized) is implanted onto a graphite disk catcher. The sample, either

the implanted isotope itself or one of its decay products, is then released from the target by laser desorption using a high-power Nd:YAG laser. RIS is performed on the resulting atomic plume using a tunable pulsed dye laser and a narrow-linewidth pulsed dye amplifier. With the higher laser bandwidth and the increased relative velocity spread of the sample, the achievable resolution ($\sim$350 MHz) is considerably worse than for COLLAPS. On the other hand, the COMPLIS method enables the study of isotopes produced by decay of the ISOLDE beam and, with the option of accumulating a sample before desorption, the measurement of isotopes with very low yield is possible provided their lifetime is long. As a result of the nature of the laser ablation process, the efficiency of the COMPLIS measurements is rather low, with typically one ion measured for every 10^5 ions implanted. To date, isotopes of Au, Pt, Ir, Sn and Te have been measured with COMPLIS. Of these, Pt and Ir are not released from the ISOLDE target but are obtained as the daughter products from the decay of a Hg beam after its implantation at the COMPLIS setup.

Laser spectroscopy with RILIS can be carried out by scanning the laser frequency for an atomic excitation step of the ionization scheme [51]. For ionization scheme development, or measurements on stable isotopes, where the beam current is in the nA range, the ion signal is measured during the scan using one of the ISOLDE Faraday cup detectors. For the radioactive isotopes, the beam is transported to a nuclear spectroscopy set-up, where a largely background free signal can be obtained by measuring the characteristic radiation decay of the isotope of interest. This technique, known as In-Source RIS was first demonstrated by the group of Letokov in Petersburg Nuclear Physics Institute (PNPI), St Petersburg [52] and has been applied at ISOLDE for the measurement of nuclear properties of Be, Ag, Cu, Pb, Bi and Tl isotopes. With ionization taking place inside the hot ionizer cavity, the atomic spectral lines are fully Doppler broadened due to the velocity distribution of the sample in the hot ionizer cavity. This Doppler broadening is typically greater than 1 GHz and therefore, whilst the in-source RIS method is unrivaled in terms of sensitivity, its application is limited to isotopes with large isotope-shifts or hyperfine structures. The technique is particularly suited to the measurement of heavier elements, for which the Doppler broadening is smaller and the mass shift is negligible compared to the field shift between

isotopes, allowing a direct measurement of the change in nuclear mean-squared charge radii. Further details of this technique are presented in this chapter in the context of the recent studies of ^{104}Ag and ^{189,191}Bi.

7.0.1 The narrow-band dye laser

In-Source RIS is most commonly performed at ISOLDE for ionization scheme development during which the primary concern is ionization efficiency. In this case the large bandwidth ($\sim$ 5 - 10 GHz) of the RILIS lasers is advantageous as one can be confident that all hyperfine components of the atomic levels are excited simultaneously. For the study of nuclear properties, such features must be resolved and a reduction in the laser bandwidth and the spectral line broadening is required to achieve a precision approaching the limit set by the Doppler broadening in the hot cavity ($\sim$ 1.5 GHz for heavy elements). This can be achieved by inserting a 6 mm thick glass Fabry-Perot etalon into the laser cavity. If the atomic transition is saturated, the linewidth is increased by power (saturation) broadening. Through the use of neutral filters, the laser power can be reduced to just below saturation to result in a reduced linewidth with little loss of ionization efficiency.

7.1 The ^{104m,104g}Ag isomer-shift

The series of elements starting from zirconium ($Z = 40 \rightarrow 46$) are not released from ISOLDE due to their low vapour pressures within the range of practical operating temperatures. Silver is the first element with Z greater than 40 to exhibit favourable diffusion characteristics that enable its release from a thick ISOLDE target matrix such as uranium carbide (UCx)[53].

With a 1 GeV beam, the production cross section for neutron-rich Ag isotopes during proton induced fission of uranium is high, but early attempts to produce pure beams of Ag were instead marred by the beam contaminants of Cd, In and other readily produced isobars which were ionized very efficiently in the plasma ion-source that was used at the time. It was this clear demonstration of the beam-purity limitations of the ISOLDE facility and the strong motivation to study the

decay of ^{129}Ag (an r-process waiting point nucleus) that initiated the development of RILIS [54].

The application of RILIS to study the ^{129}Ag was still hampered by an isobaric background of indium which is readily surface ionized. An additional cause for concern in terms of RILIS efficiency was the magnitude of the hyperfine splitting. For the Ag isotopes of known nuclear spin lying closer to stability, dramatic variations in the size of the HFS have been observed [55]. For the $I = \frac{1}{2}$ isotopes, the ground-state splitting is of the order of a few GHz and so is smaller in magnitude than the laser linewidth. For the $I = \frac{7}{2}$ and $I = \frac{9}{2}$ nuclei, the splitting is far greater ($\sim$ 39 and $\sim$ 48 GHz respectively). The HFS for ^{107,107m} Ag were measured by Sebastian *et al.* [56] as a feasibility study of the spectroscopic capabilities of In-Source RIS with RILIS. The splitting of the $I = \frac{1}{2}$ state proved too small to be resolved but, for $I = \frac{7}{2}$, two distinct HFS multiplet structures were observable. A subsequent RIS study of ^{122}Ag combined for the first time the techniques of atomic and nuclear spectroscopy at ISOLDE. For this measurement, by observing the relative intensities of the gamma-decay lines for ^{122}Ag as a function of laser frequency, it was possible to assign the gamma lines to the decay of the high- or the low- spin isomer [57].

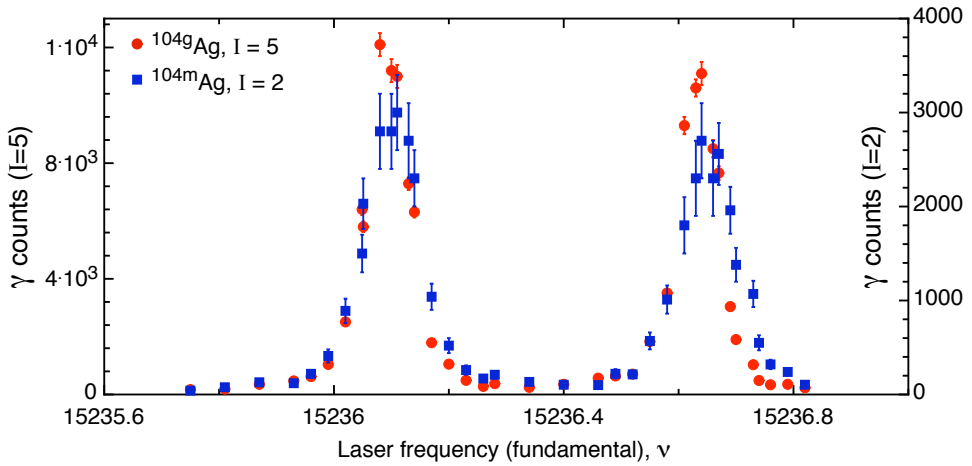

Figure 7.1: The HFS measurements of ^{104m,g}Ag performed in 2002.

The hyperfine structures of Ag isotopes were briefly studied again in 2002 during yield measurements of the neutron- deficient Ag isotopes from a uranium

carbide target. Only a crude data collection and scanning procedure was used since the intention was not to accurately determine nuclear parameters but to examine the possibility of isomer-selective ionization, where the primary interest is in determining the resonance frequencies corresponding to the greatest difference between the isomer and ground-state ionization efficiency. No results were published from this work but in the measurement of ^{104}Ag, it was possible to plot the HFS of the high- and low- spin isomers from a single laser scan based upon the known assignments of the gamma lines following the decay to ^{104}Pd. A typical spectrum is shown in Figure 7.1. The collection of these optical spectra predated the recent in-source RIS improvements that were implemented for the dedicated RIS studies with RILIS. Tuning the laser frequency therefore required manual adjustment of the dye-laser grating. These data were not analyzed in depth but an interesting observation was that all of the optical spectra obtained exhibit a small bump in the hyperfine structure at the high-frequency side of the HFS for the $I = 2$ state. Since this isomer-shift has not previously been measured, it was suspected that the observed HFS (which closely overlaps the HFS for the $I = 5$ state) was due to an incorrect assignment of one or more of the gamma energies to the $I = 2$ decay and that the small bump is the influence of the true $I = 2$ HFS, which is masked by the comparatively large $I = 5$ structure. These measurements have been repeated, taking advantage of a newly implemented computerized dye-laser grating control system and a feedback-based frequency stabilization program (developed for use in a series of in-source RIS studies on the neutron-deficient isotopes in the vicinity of $Z = 82$). This further study has enabled a rigorous check of the gamma-decay assignments to be performed with the benefit of increased confidence in the laser frequency position at each scanning interval.

7.1.1 Production

A uranium carbide (UCx) target of thickness 51 g/cm^2 was used for the production of ^{104}Ag by proton-induced fission. The RILIS ionization scheme for Ag is a three-step scheme using a non-resonant ionization step. The first excitation step requires UV generation by frequency doubling. An efficiency measurement

performed in 1998 using this scheme and with similar laser operating conditions determined the RILIS efficiency to be 11 % for the stable isotopes ^{107,109}Ag. Both of these have a ground-state spin of $\frac{1}{2}$ and so the HFS is smaller than the laser linewidth of the first-step laser. The large HFS for ^{104}Ag will reduce the ionization efficiency by up to 50 %.

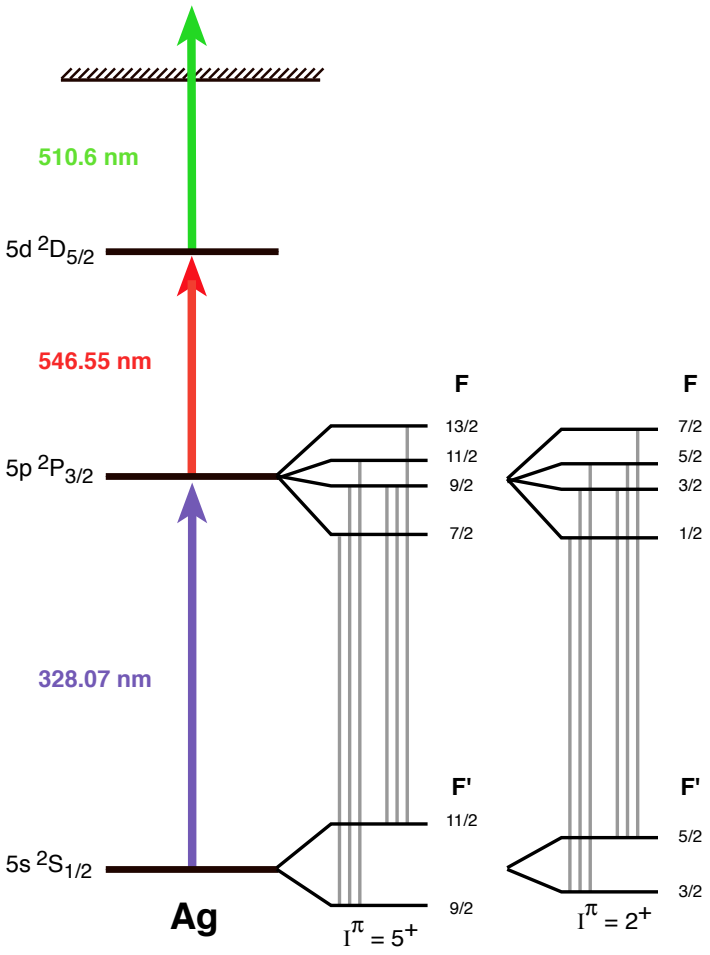

Figure 7.2: The RILIS ionization scheme for Ag.

7.1.2 Data Collection

The data acquisition was performed as an extension of a set of yield measurements using the ISOLDE tape station set-up. This system is illustrated in Figure 7.3. For yield measurements with the tape station it is important that the technical aspects of the data collection are recorded in order to deduce the yield in terms of atoms per micro-Coulomb of the incident proton beam. For its purpose as a means of particle detection during RIS studies, it is important only to maintain consistency throughout the measurement cycles. The operating conditions are listed in Table 7.1. The tape transport time T_t was assumed to be constant and small compared to the measurement time T_{meas}.

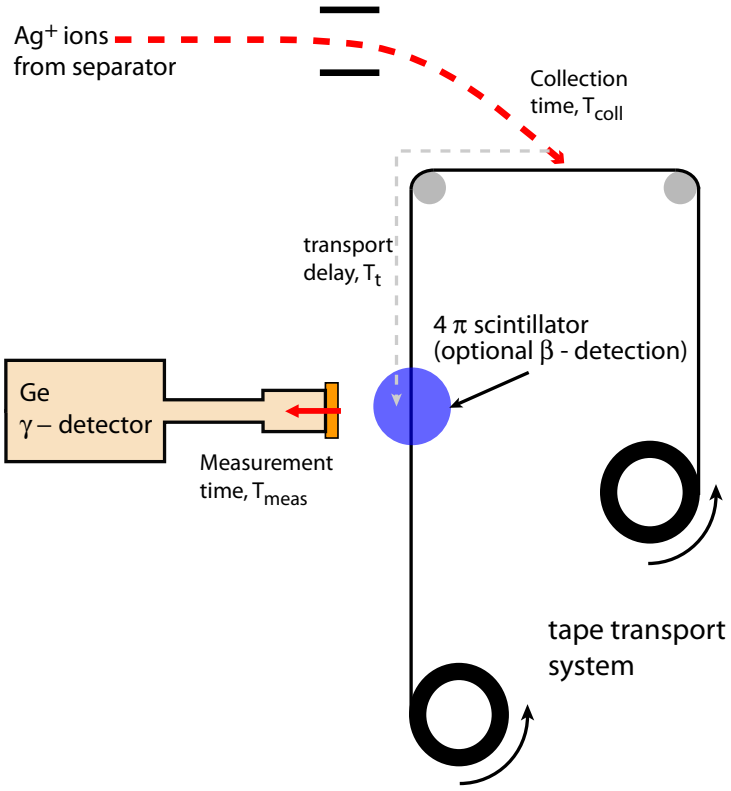

Figure 7.3: The movable tape system used for yield and lifetime measurements of short-lived β and γ emitters.

Table 7.1: The laser scanning and gamma-spectra acquisition parameters.

Mass, A	104
Half life, $t_{1/2}$	69.2 m (g), 33.5 m (m)
Proton intensity	3.2×10^{13}/pulse
No of pulses	5/supercycle
Collection time T_{coll}	16.8 s
Measurement time T_{meas}	200 s
Start frequency (fundamental)	15235.75 cm^{-1}
End frequency	15236.82 $^{-1}$
No of scan steps	38

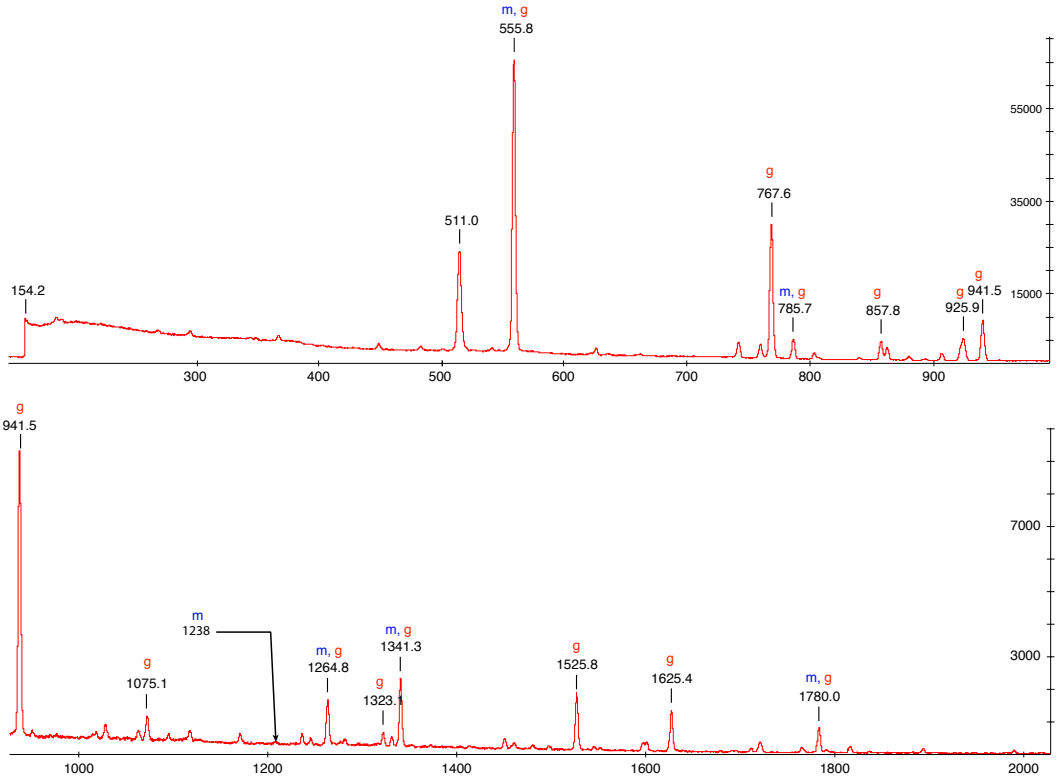

Figure 7.4: The gamma-spectra obtained after implantation of the ^{104} Ag beam on the tape.

Figure 7.4 shows a summation of the gamma spectra obtained for each 200 s collection period. The strong gamma lines are indicated along with their ^{104g}Ag or ^{104m}Ag assignment taken from the Pd level scheme in the Table of Isotopes [58]. Many of the lines are assigned to both the isomer and the ground-state and in fact, the strongest line associated with the isomer only is at 1238 keV, barely visible on the scale of the figure. For an incorrect gamma-line assignment effect to be observed within the optical spectra, it would have to be related to one of the strong lines visible within Figure 7.4. To investigate this, a laser scan was constructed for each of the gamma lines, using the sum of the counts in each gamma peak (after background subtraction).

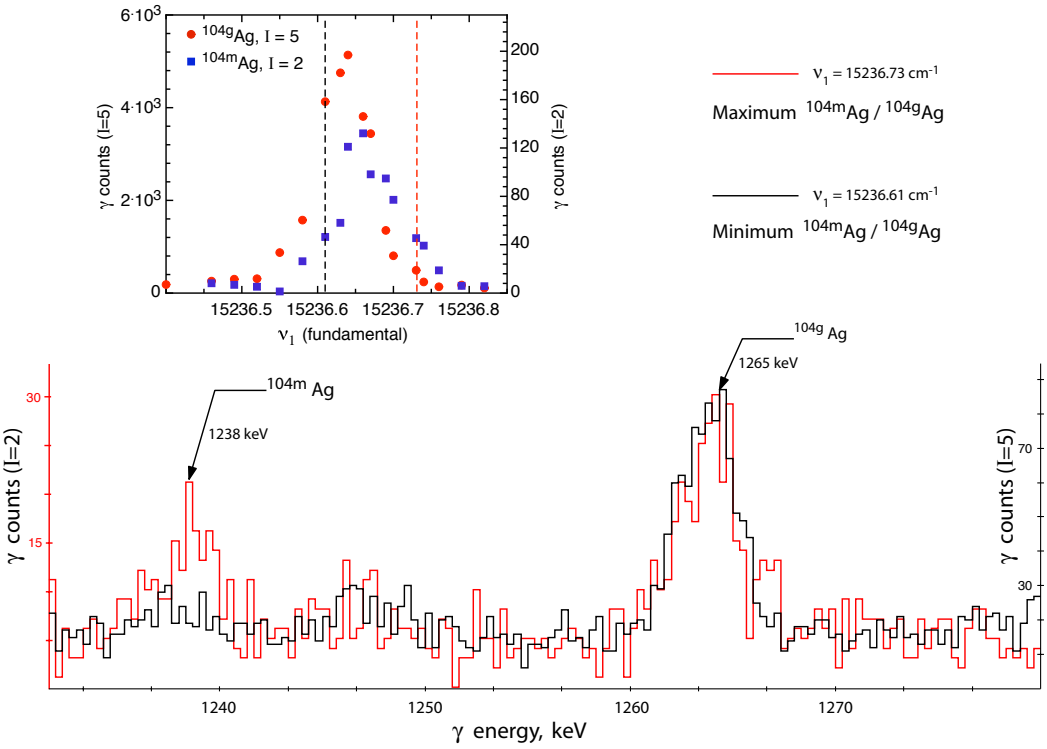

Figure 7.5: Identification of the 1238 keV gamma peak assigned to ^{104m}Ag by precise tuning of the laser frequency across the F′ = 9/2 HFS multiplet.

Figure 7.5 shows two superimposed gamma spectra for ^{104}Ag in the energy range 1250 - 1280 keV. This energy interval encompasses two weak gamma lines: 1238 keV and 1265 keV, which are given pure ^{104m}Ag and ^{104g}Ag assignments

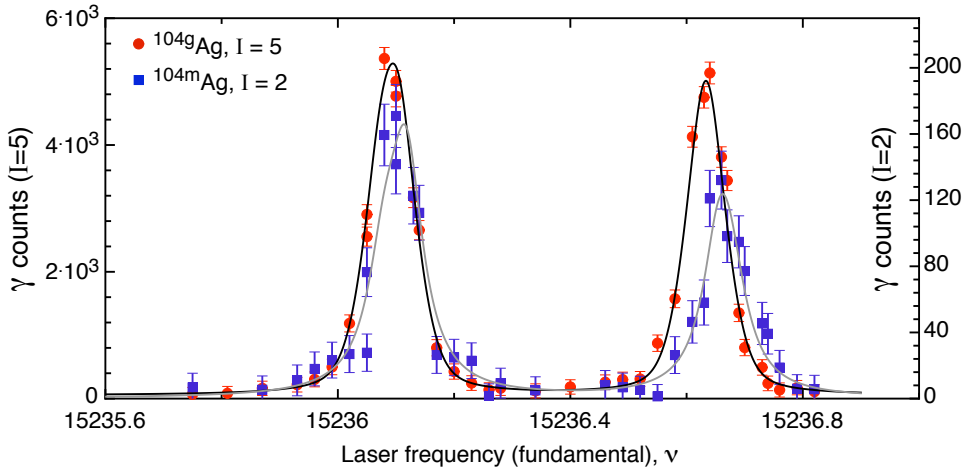

Figure 7.6: The new measurements of the ^{104}Ag HFS. For ^{104g}Ag the data are the summed γ counts from the five most intense lines measured. The ^{104m}Ag data are the summed γ counts in the peak at 1238 keV.

respectively. The red spectrum was obtained with the laser frequency at setting corresponding to the maximum ^{104m}Ag:^{104g}Ag ratio, as indicated on the inset HFS spectrum.

7.1.3 Results

The optical spectra were fitted with a χ^2-minimization program based upon the CERN MINIM routine [59]. The spectral lineshape, a convolution of a Gaussian (Doppler broadened) and a Lorentzian (laser lineshape) was fitted with a Voigt profile for which the Gaussian component is one of the fitting parameters. Additionally, the background, peak width (FWHM), structure intensity, structure centroid and the hyperfine coefficients of the upper and lower levels were included as fitting parameters. Standard errors were calculated for the extracted features by determining the parameter change required to increase χ^2 to $\chi^2_{min} + \chi^2_{min}/N_{df}$, where N_{df} is the number of degrees of freedom.

Optical spectra were produced for each of the strong gamma lines labeled in Figure 7.4 individually. Fitting was performed for each of these and also for the only observable pure ^{104m}Ag gamma line (1238 keV). The gamma-spectra analysis was performed using the RADWARE package and macro programs were

created to extract the number of gamma counts in each peak by a summation of the bins within constant channel number window size, determined by examining the peak shape at an 'on resonance' position. The background count rate at each scanning position was determined as the average count rate per channel for two channel windows selected in featureless regions of the spectrum, either side of and equidistant from the gamma-peak. The mean background value for each scanning position was subtracted from the corresponding peak count rates.

With the exception of the 1238 keV peak, the fits for all of the optical spectra were identical within experimental errors. This was true even for the gamma-lines with a mixed isomer and ground-state assignments on account of the relatively small isomer fraction of the total beam current.

Table 7.2 summarizes the fit results from the spectra displayed in Figure 7.6. Using the ratio of $A_{g.s}(^2S_{1/2})/A_{is}(^2S_{1/2})$ obtained from the fit results, it has been possible to extract a magnetic moment value for the isomer of $\mu_{2+} = +3.704(11)$ μ_N assuming that the sign of the A value is positive. This is an improvement in accuracy over the published value of +3.7(2) μ_N given in Reference [60]. Despite the clear difference in the hyperfine structures between the two nuclear spin states, on account of the relative weighting of the states, the measured isotope-shift of 288(180)MHz is not significantly larger than the experimental errors.

Table 7.2: The fit results and extracted magnetic moments and isotope-shifts for ^{104}Ag and ^{104m}Ag. The magnetic moments are determined with a greater degree of precision than the published values (labeled a).

A	I^π	A_m/A_g MHz	μ n.m	$\mu^{(a)}$ n.m.	Isotope Shift MHz	Ref.
104	5^+	–405.5(27)	$+4464(27)^{(f)}$	+3.729(3)	–21790(300)	this work
104m	2^+	–403.7(12)	$+4444(12)^{(f)}$	+3.704(11)	–17894(200)	this work

7.2 The isotope-shifts and magnetic moments of ^{189}Bi and ^{191}Bi

During the ISOLDE 2004 operational period, the first on-line run for experiment number IS407 [61] took place. This experiment aimed to investigate the nuclear structure and ground-state properties of Pb and Bi isotopes across the N=104 neutron mid-shell. Figure 7.7 shows the extent of the study of charge radii systematics within this region of the nuclear chart and it exhibits some interesting phenomena, notably, the huge odd-even staggering for Hg and abrupt shape changes in the Au and Ir isotope chains. A large isomer-shift has been observed for ^{185}Hg [62], [63] with the $\frac{13}{2}^+$ isomer exhibiting a charge radius that brings it in line with the trend in the isotope chain before the onset of the large odd-even staggering. In addition, the charge radii of Pt isotopes close to N = 104 exhibit a large deviation from the droplet model predictions. Shape coexistence, the presence of strongly prolate or oblate configurations at low excitation energy, is a probable explanation for these isotopes being prone to large shape changes or digressions from the droplet model predictions [64].

Shape coexistence has been investigated thoroughly for the Pb and Po chains at many facilities through alpha-decay and gamma-ray spectroscopy studies [65] and compelling evidence for this phenomenon was provided by a study of ^{186}Pb [66]. In this experiment, the alpha-decay of ^{190}Po was studied in coincidence with conversion electrons, and characteristic gamma- and X-rays. The data showed that the 0^+ ground-state was populated not purely by a gamma cascade from the excited configuration after the alpha-decay of Po, but also via the population of two low-lying 0^+ states with subsequent E0 conversion electron emission.

Charge-radii determinations from optical isotope-shift measurements offer a uniquely model independent means of studying this effect and form the principal motivation for experiment IS407 at ISOLDE. Measurements on the Pb chain down to $A = 183$ were performed initially [67], and extended to include the 55 ms ^{182}Pb isotope during the 2005 experimental period (this analysis is in progress). These studies showed little departure from the spherical ground-state configuration, leading to the conclusion that the mixing with any low-energy deformed configurations is not significant for these isotopes. Measuring the neighbouring

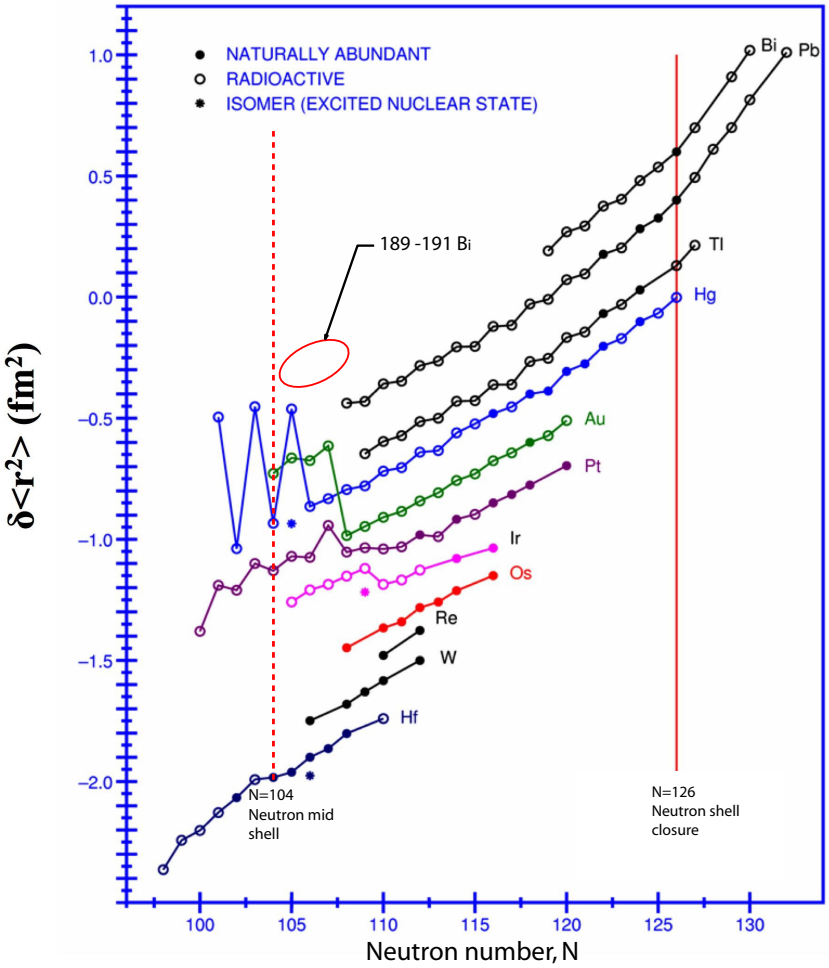

Figure 7.7: Trends in mean-squared charge radii for isotopes near Z = 82.

bismuth isotopes was a secondary goal of the first experiment, with ^{189}Bi and ^{191}Bi successfully measured to provide data fourteen isotopes further from stability than previous optical measurements on bismuth. The analysis and results are presented here and were acquired due to the collaborative efforts of groups from IKS-K.U.Leuven, IPN-Orsay, The University of Mainz, and the ISOLDE collaboration.

7.2.1 Previous bismuth measurements at ISOLDE

The ground-state properties of A=205, 206, 208, 210, 210m, 212 and 213 bismuth isotopes have been measured earlier at the ISOLDE facility using the technique of resonant laser fluorescence spectroscopy of atoms in an inert buffer gas [68]. During that work, the proton energy at ISOLDE was limited to 1 GeV. The isotopes ^{205,206,212,213}Bi were obtained as the granddaughters in the decay chain of francium isotopes produced by proton spallation on a uranium target using a hot tungsten cavity surface ion source. The ^{208,210,210m}Bi isotopes were produced by spallation of a thorium target and were ionized with a hot plasma discharge ion source.

In addition to the sensitivity gain from the in-source RIS technique, the upgrade of the CERN PSB proton beam-energy to 1.4 GeV has resulted in increased production cross sections for bismuth isotopes approaching the proton drip-line.

7.2.1.1 Isotope production and detection

The neutron-deficient isotopes of bismuth are alpha emitters. They were produced within a 50 g/cm^2 uranium carbide (UC_x) target by spallation reactions induced by the incident 1.4 GeV proton beam. The relevant decay data and production yields are given in Table 7.3 for each isotope the alpha-decay branching ratio was more than 50 %. Diffusion through the target matrix and effusion to the ion source was enhanced by applying 650 A to the target heater supply (T $\approx$ 2300 K).

Bismuth atoms were resonantly ionized inside a standard tungsten hot cavity ionizer tube using the RILIS ionization scheme shown in Figure 7.8. This scheme

Table 7.3: Yield and α-decay information for ^{189,191}Bi.

A	I^{π}	$T_{1/2}$ (s)	E_{α} (keV)	Rel int. (%)	Yield (ions/μC)
189	$\frac{9}{2}^-$	0.680(30)	6672(5)	95(3)	1.4×10^2
			7116(15)	5(3)	
191	$\frac{9}{2}^-$	12(1)	6311(5)	97.1(3)	3.0×10^4
			6639(5)	2.9(3)	
191	$\frac{1}{2}^+$	0.150(15)	6876(5)	100	7.3×10^1

The yield information is taken from the ISOLDE PSB yields database [12].

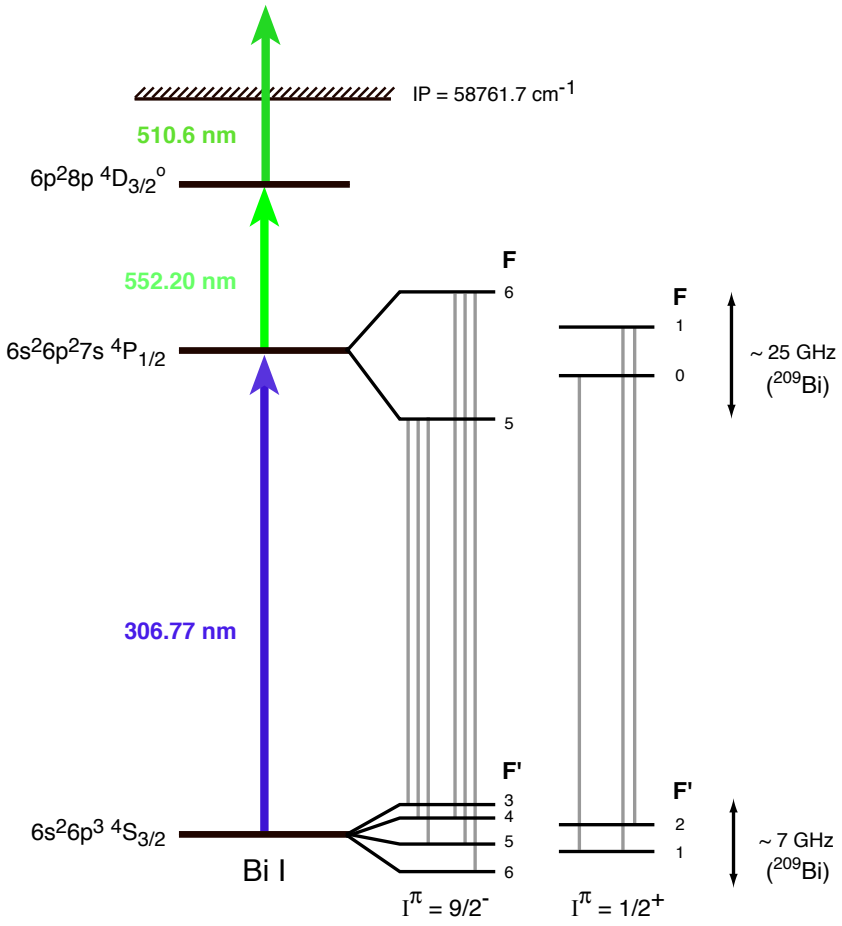

Figure 7.8: The RILIS ionization scheme for bismuth.

was developed in January 2000. During the tests the RILIS efficiency was determined by evaporation of a 2750 nAh Bi mass marker. After evaporation, the

integral of the ion current measured on the Faraday cup was determined to be 165 nAh, a RILIS efficiency of close to 6 %. The ionizer cavity heating current (LINE) was kept at 250 A throughout the measurements.

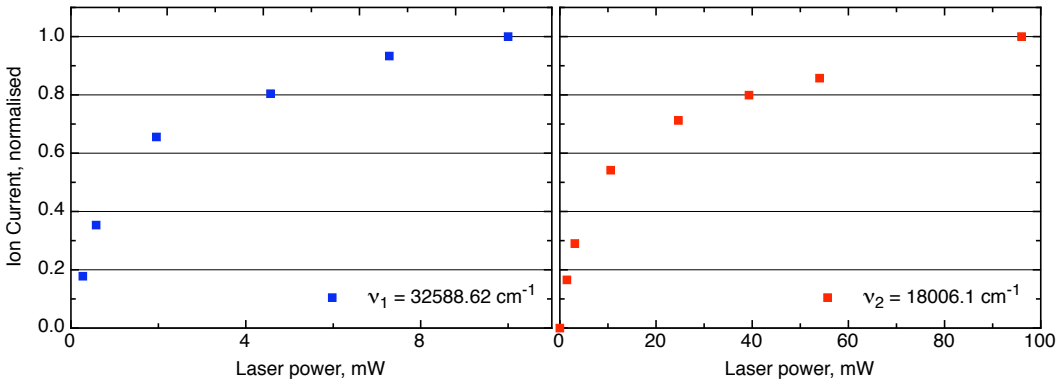

Figure 7.9: Saturation curves for the two resonant transitions of the bismuth ionization scheme. The values of laser power are the estimated power transmitted to the ion source.

During the experiment sufficient laser power was available to saturate both the resonant transitions. The saturation curves are shown in Figure 7.9. For laser scanning in narrow-band mode, the laser power for the first step was reduced to below the level of saturation in order to avoid power broadening of the spectral line. At this reduced laser power and as a result of operating in narrow-band mode with a laser linewidth less than the hyperfine structure splitting, the maximum ionization efficiency during laser scans was expected to be closer to 1 %.

The Bi ions were extracted with a 60 keV potential and mass separated using the GPS. The desired mass was then guided to the spectroscopy set-up where the yield of the selected isotope as a function of laser frequency can be monitored by their characteristic alpha-decay energies.

The alpha detection set-up and data acquisition system were provided by the Nuclear Spectroscopy group at the IKS, Leuven. The system uses a 'windmill' configuration with ten catcher disks mounted around the circumference of a rotating wheel (Figure 7.10)

Carbon catcher disks with a thickness of 20 μg/cm^2 were used for beam implantation. They were thin enough to enable easy identification of nearby al-

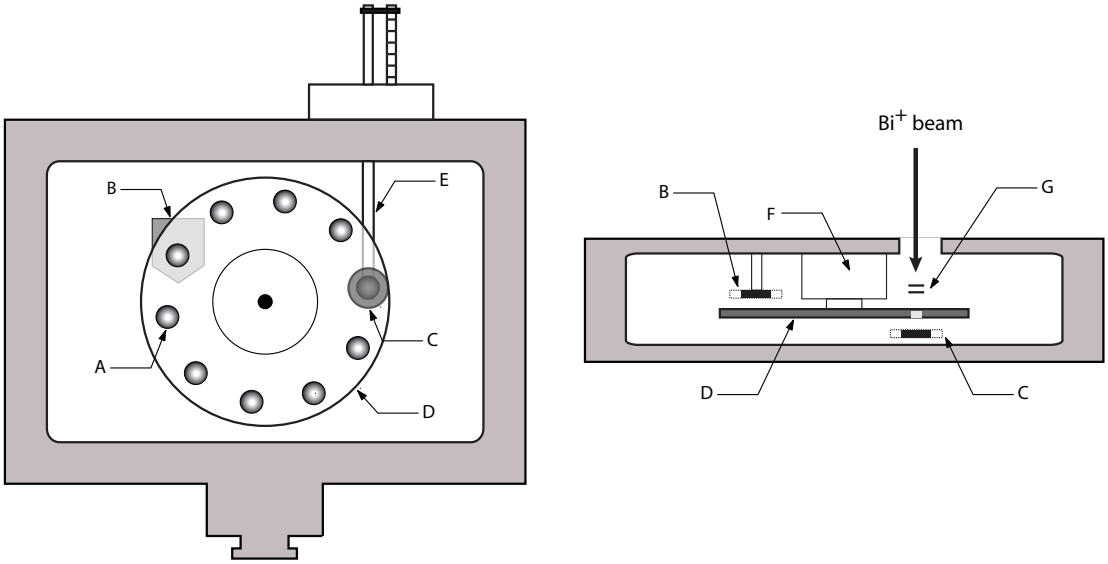

Figure 7.10: The moving target alpha detection unit. The ten carbon disks (A) are mounted on a wheel (D) that can be rotated using a stepping motor (F). The incident beam current can either be measured with a moveable Faraday cup (E) or can be sent through a collimator (G) onto the foil. One Si detector (C) measures the alpha spectrum during implantation on the foil, a second detector was used to measure a previously implanted foil to verify its cleanliness before re-use.

pha peaks (better than 50 keV resolution). A passively implanted planar silicon (PIPS) detector was placed behind the catcher foil. A detection surface area of 150 mm^2 and a thickness of 300 μm was used.

A LynxOS system running the MBS data collection software was used. The MBS software is a C-based data acquisition and monitoring system that supports input from a wide range of electronics units (NIM, VME, CAMAC) and interfaces well with the standard CERN graphics and analysis packages, PAW and ROOT [69]. For this experiment, data were acquired via a series of NIM and VME electronics units and the initial analysis and data manipulation were performed using linux PCs running PAW. A detailed description of the data acquisition system and electronics configuration is given in References [67] and [70].

The MBS system was operated in *list* mode, triggering from the alpha detector. In this mode, each event is stamped with the time elapsed from the start of the measurement (given by a TDC) and the laser-frequency position (sent via an RS232 signal from the laser control PC) is appended to the list mode data file.

Figure 7.11 shows typical alpha spectra for ^{189}Bi and ^{191}Bi. For ^{191}Bi the optical spectra show a significant difference between the HFS for the ground-state and for the isomer. This is demonstrated further in the accompanying alpha spectra where the left-hand spectrum was obtained at a scan position with the highest $\frac{1}{2}^+$:$\frac{9}{2}^-$ spin state ratio and the right-hand spectrum shows the highest obtainable $\frac{9}{2}^-$:$\frac{1}{2}^+$ ratio.

For ^{189}Bi, examples of alpha spectra taken during a scan of the higher energy side of the HFS are given. The spectrum on the right was acquired whilst the laser was tuned to near resonance with the HFS peaks, and the left spectrum was obtained earlier in the laser scan, with the laser tuned to a frequency approximately corresponding to the mid-point between the high and low energy groups of HF components.

7.2.1.2 Laser scanning

The frequency of the scanning laser can be adjusted using a PC equipped with a 'Measurement Computing' 16-bit multichannel DAQ card. This allows control of dye-laser etalon and grating angles by sending -10 V to +10 V DC signals to the

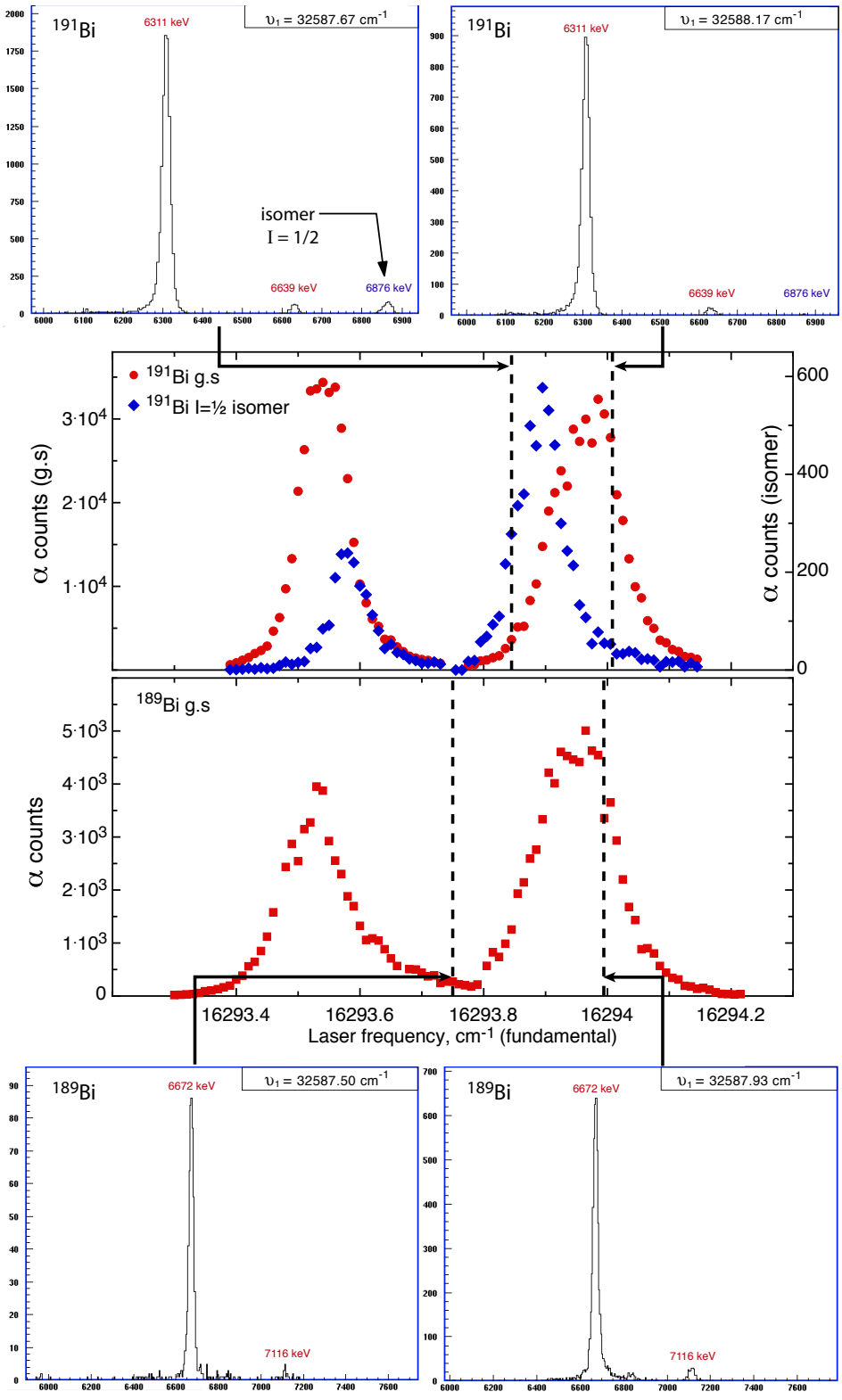

Figure 7.11: Examples of alpha spectra acquired during fine scans of ^{189}Bi and ^{191}Bi

respective motors. This system was integrated into an automated laser scanning and stabilization system that was newly implemented at RILIS specifically for the experimental programme that encompasses this work. The system was developed by the ALMAS Group at Mainz University. For neutron-deficient isotopes with low production rates, the dwell time at each laser scan interval must be long (minutes) and so a laser-frequency readout/feedback-based frequency stabilization algorithm was included in the control program. Communication with the data acquisition enabled synchronization of the dye-laser etalon scanning increments with the PSB proton pulse supercycle. Additionally, a feedback based laser-frequency stabilization algorithm was incorporated and for each scan position, the value of the mean laser frequency was sent to the data acquisition system via RS232 and TCP/IP protocols. Using this system it was also possible to synchronize the laser scan stepping intervals and dwell time with the proton pulse time structure. Depending on the alpha count rate for the isotope being measured, the dwell time per scan position was set to an integer number of PSB proton pulse supercycles (n $\times$ 16.8 s). Figure 7.12 shows the event time structure within the measurement cycle. For bismuth the beam gate settings (closed/open) were 1/350 (ms) and 10/600 (ms) for masses 189 and 191 respectively: during each proton pulse the beam gate was closed. It was re-opened to allow alpha counting to start after a delay time which was optimized according to the release characteristics of the element of interest. This is a standard technique used at ISOLDE to reduce the level of isobaric contamination within the beam [16]. Additionally, in order to avoid saturation of the detectors, the alpha count rate can be limited by shortening the beamgate 'open' duration.

The odd bismuth isotopes exhibit an unusually large hyperfine structure with the hyperfine splitting greater than the resonance linewidth of the second-step in the ionization scheme. This adds some extra complexity to the scanning procedure: if a fixed second-step frequency is used then, during a scan of the first-step frequency across the entire hyperfine structure, the de-tuning of the second-step frequency becomes significant. This is illustrated in Figure 7.13 where a crude scan of the second-step resonance is plotted. Considering that the hyperfine splitting of the first excited level in ^{209}Bi is $\sim$25 GHz (0.8 cm^{-1} after frequency-doubling) it is clear that separate laser scans, each with an adjusted second-step

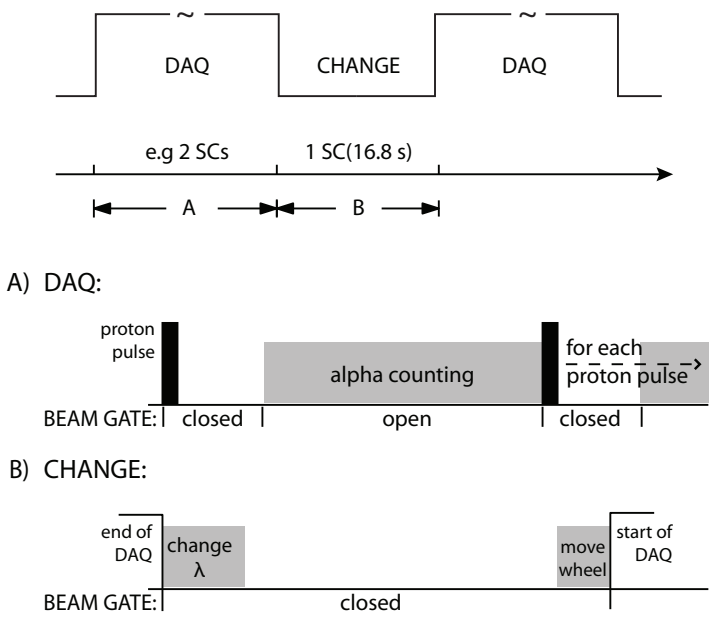

Figure 7.12: The data acquisition cycle for bismuth spectroscopy.

laser-frequency position, are required for transitions to the $F = 4$ and $F = 5$ levels of the excited state.

With the experience gained from previous in-source RIS work at the ISOLDE RILIS, it was anticipated that the laser power fluctuations and some drift in the laser-frequency measurement would be the main sources of uncertainty in the results of this experiment. At PNPI, St Petersburg, for their RIS work they address this problem with the use of a reference cell in which a vapour of a stable sample of the element of interest is created and resonantly ionized with a proportion of the laser power used for the spectroscopy study. The simultaneous collection of the stable spectra, for which the nuclear parameters and hyperfine structure are known to a high degree of accuracy, allows reliable corrections and fitting constraints to be applied to the radioactive spectra. Similarly, during the RILIS study of Cu isotopes at ISOLDE [71], the higher or lower mass stable isotope was guided along a neighbouring beam-line, allowing measurements of stable and radioactive spectra to be made simultaneously. This is only possible however when studying isotopes within a few mass units from stability. For the

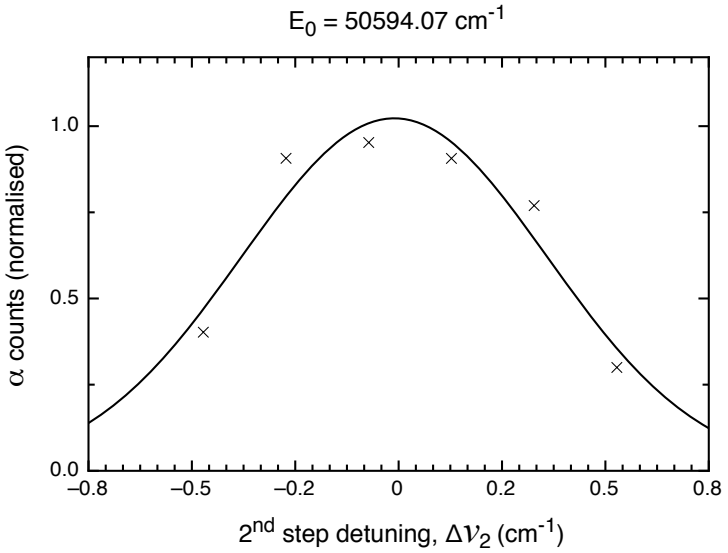

Figure 7.13: A rough scan of the second-step frequency using a fixed first-step frequency.

extremely neutron-deficient ^{189,191}Bi isotopes, this is not a possibility. Instead, an impression of the laser performance fluctuations during a single scan is obtained by taking alpha spectrum measurements at a reference frequency at regular intervals during the laser scan. For the Bi spectra, such readings were taken after every three laser-frequency stepping intervals. An 'on-resonance' reference frequency position was chosen. As an example, the alpha counts at the reference frequency during one laser scan are plotted in Figure 7.14.

For frequency calibration and in order to better understand the ionization spectrum and laser parameters such as lineshape, linewidth and saturation, it was necessary to obtain reference spectra with the stable isotope, ^{209}Bi regularly. With the proton beam request turned off, a vapour of stable bismuth was released into the ionizer cavity by heating a bismuth sample (mass marker) within one of ovens of the ISOLDE front end unit. The resulting ion-beam current (some nA on resonance) of ^{209}Bi could be measured using a Faraday cup detector positioned immediately after the mass separator. Since the ionization conditions and laser parameters remain unchanged, the spectra obtained are essential for optimizing the fitting procedure for the radioactive isotopes.

Fine scans were performed for each of the low energy and high energy HFS

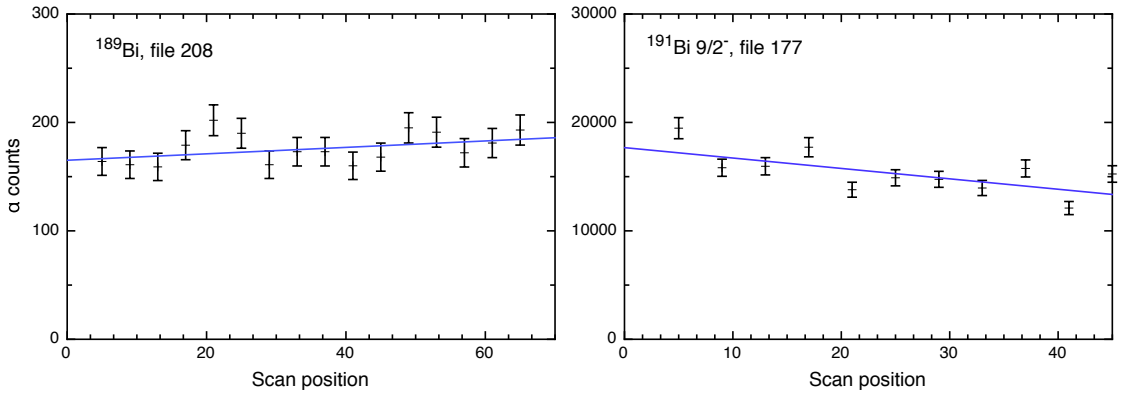

Figure 7.14: Typical reference fluctuations during laser scans for each isotope studied.

triplets individually. An example of these scans for each side of the HFS is shown in Figure 7.15. The fitting routine and details of the constraints imposed on the fitting parameters are discussed in the following sections.

Figure 7.16 shows the gradual drift of the ^{209}Bi centroid frequency obtained from fits of the reference spectra during the experimental period. Each of the data points represents a cluster of reference measurements taken within a narrow time window (∼50 minutes). The mean acquisition time and centroid position is plotted, with an error bar corresponding to the standard error from the dataset.

This change in wavemeter calibration has been previously experienced during RILIS running and as such, it has become standard practice to perform a wavelength optimization as part of the preparation for any RILIS-dependent experiment, rather then relying on the previously used wavelength values. The primary cause of the wavemeter instability is thought to be temperature fluctuations. During the measurements of the lead isotopes, conducted in the days before the bismuth study, the wavemeter drift was of a similar magnitude but with a negative slope. At this stage the internal cooling system of the wavemeter was activated. A reversal of the drift direction was observed shortly after this and a different correction had to be applied for ^{190}Pb which was the final lead isotope to be measured [67]. Clearly this upward drift of the wavelength calibration persisted during the bismuth measurements. The instability in the wavemeter

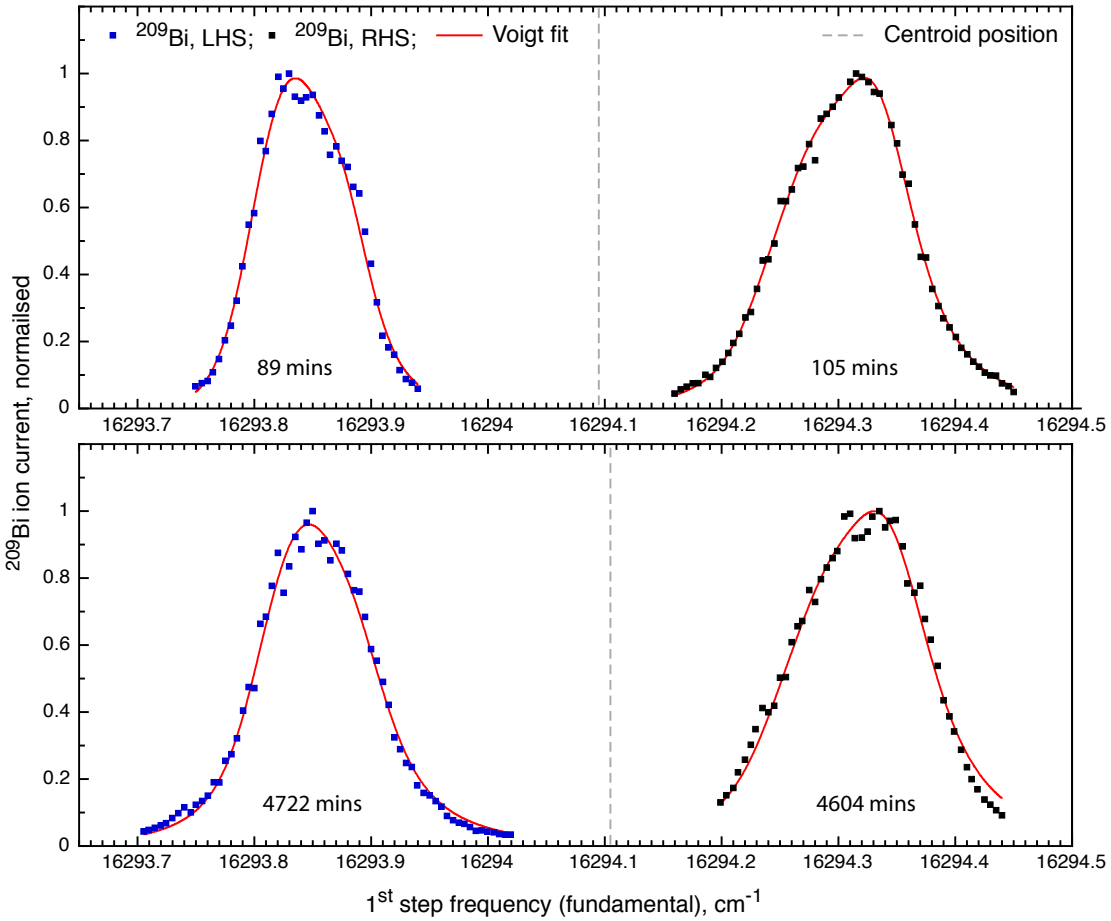

Figure 7.15: Voigt fits for four of the stable bismuth spectra. For each scan, the time elapsed from the beginning of the experimental period is marked. For the LHS and RHS spectra, different second-step frequencies were used, adjusted to account for energy difference between the hyperfine structure triplets. The mean centroid position for the total HFS in each plot is indicated.

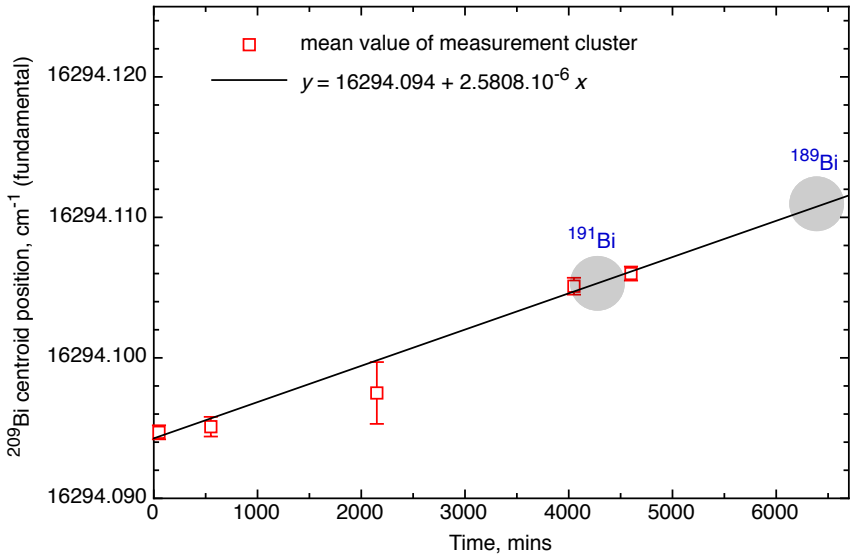

Figure 7.16: The drift of the centroid position for stable bismuth during the measurement period. No reference measurements were taken close to the time of the data collection for ^{189}Bi. The ^{209}Bi reference value for this isotope was taken from the linear fit parameters.

calibration introduces a large degree of uncertainty for absolute frequency measurements but the accuracy of relative frequency measurements is estimated to be approximately 40 MHz (0.0013 cm^{-1}) provided that a suitable reference point is available. For isotope-shift measurements of the radioactive bismuth isotopes, the centroid positions obtained from the fits were related to a ^{209}Bi centroid reference value, ν_{209}, for the same measurement time, t. This reference value was calculated from the linear fit parameters of Figure 7.16:

$$\frac{\nu_{209}}{2} = 16294.0940(15) + 2.5808(76) \times 10^{-6} t \tag{7.1}$$

For ^{191}Bi the reference spectra were acquired within a few hours before and after the measurements and so this procedure for reference frequency determination could be carried out with a good degree of confidence in its validity. For ^{189}Bi however, the data were taken approximately 1800 minutes after the final reference spectrum. Since the onset of the upward drift can be attributed to the activation of the wavemeter cooling system which remained on for the remainder

of the experimental period. It is unlikely that a significant increase in gradient of the slope would have been observed within 1800 minutes of the final reference measurement. The most extreme conceivable departure from Equation 7.1 is a decrease in gradient towards a plateau. In the analysis of the ^{191}Bi spectra, the reference frequency corresponding to the fitted line parameters was used but the implications of a flattening of the frequency drift trend are discussed.

Table 7.4: Laser scanning settings for the radioactive bismuth isotopes.

Time mins	A	$\nu_{start}/2$ cm^{-1}	$\nu_{end}/2$ cm^{-1}	$\nu_{ref}/2$ cm^{-1}	ν_2 cm^{-1}	Power, P$_1$ rel.
4124	191	16293.390	16293.730	16293.640	18006.90	2.5
4187	191	16293.390	16293.730	16293.540	18006.90	1.2
4232	191	16293.390	16293.730	16293.540	18006.90	1.2
4282	191	16293.700	16294.090	16293.900	18006.20	1.2
4431	191	16293.755	16294.145	16293.990	18006.20	2.6
6252	189	16293.300	16293.900	16293.530	18006.90	1.2
6522	189	16293.805	16294.225	16293.970	18006.20	1.2
6558	189	16293.805	16294.225	16293.970	18006.20	1.2

7.2.2 Fitting procedure

In order to reliably extract the centroid positions from the stable bismuth scans shown in Figure 7.16, care had to be taken to ensure that the fitting procedure was capable of accounting for the relevant laser characteristics and experimental considerations. For the mass 209, 189 and 191, the spin $\frac{9}{2}^-$ ground-states all give rise to six hyperfine structure components, separated into two triplets by the large splitting of the upper atomic state. Correctly fitting the experimental spectra was not trivial due to the inability to resolve the structure within the two HFS triplets. It is important to consider the triplet substructure in the fitting routine since the different line spacing and intensities of the constituent hyperfine components add a degree of asymmetry to the observed peaks.

7.2.2.1 Lineshape

An additional degree of uncertainty in the measurement of the laser frequency stems from the means by which the ATOS wavemeter analyses the fringe patterns from its four Fizeau interferometers. In standard operation, the wavemeter operates in 'CRUDE' mode and the peak positions within the interference patterns for each interferometer are determined using a 'centre-of-gravity' calculation. At certain relative orientations of the diffraction grating and etalon positions, the laser lineshape can become sufficiently deformed for the measured frequency to differ significantly from the frequency at the intensity maximum: $|\nu_{CoG} - \nu| \leq$ 100 MHz. As a precaution, the laser was scanned within the ranges of various grating/etalon angle calibrations chosen to provide a symmetrical lineshape. Due to the large scanning range involved for the wide bismuth HFS, some detectable changes in laser lineshape are unavoidable.

In the case of ^{191}Bi, the alpha decay of the $\frac{1}{2}^+$ isomer was observable, providing an opportunity to analyze the lineshape parameters for a pure line: For $I = \frac{1}{2}$, the upper and lower levels split into $F = 0, 1$ and $F = 2, 1$ states respectively, resulting in a HFS with a single peak ($F = 1 \rightarrow 0$) at the low energy side and an unresolved doublet at the high energy side of the spectrum.

This isomer peak was fitted as a single deformed Voigt profile. The Voigt profile is a convolution of a Gaussian profile (Doppler broadened) and a deformed Lorentzian profile (natural lineshape plus deformation parameter):

$$I(\nu) = I_0 \int G(\nu')L(\nu - \nu')d\nu' + I_{bg} \tag{7.2}$$

The Gaussian component of Equation 7.2 accounts for the Doppler broadening of the spectral line due to the thermal velocity distribution of the atoms within the hot cavity:

$$G(\nu) = G_0 \exp\left[-\frac{(\nu - \nu_0)^2}{0.36\delta\nu_{\mathrm{D}}^2}\right] \tag{7.3}$$

for which the HWHM (Doppler width), $\delta\nu_D$ is given by:

$$\delta\nu_D = \frac{\nu_0}{c}\left(8k_BT\frac{\ln 2}{m}\right)^{\frac{1}{2}} \tag{7.4}$$

where ν_0 is the transition frequency and k_B is the Boltzmann constant. For the bismuth isotopes, $\delta\nu_D$ = 700 MHz (0.023 cm^{-1} at the fundamental frequency) was used.

The Lorentzian component of Equation 7.2 incorporates both the natural linewidth of the transition and the deformation of laser lineshape due to a departure from the ideal calibration of the relative grating and etalon orientation within the dye laser. An exaggerated example of the deformed Lorentzian is shown in Figure 7.17.

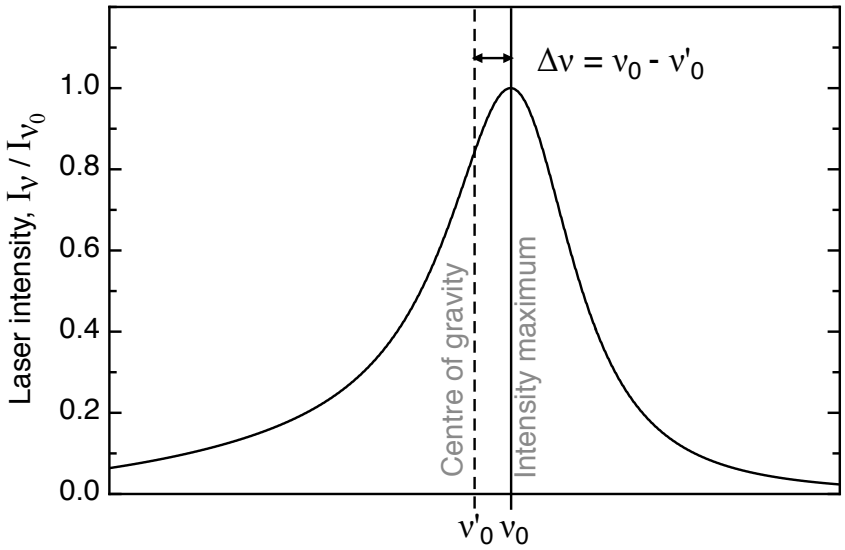

Figure 7.17: A Lorentzian curve with a large $\Delta\nu$ value for $\nu_0(^{191}\mathrm{Bi}^{I=1/2}$, $F = 1\rightarrow 0)$

For the analysis of the Pb data from the same experimental period [67], this lineshape is reproduced by the superposition of two Lorentzian profiles, $g(\nu)$ and $f_{mod}(\nu, \Delta\nu)$ with widths γ and $k\gamma$ respectively, separated by the frequency interval $\Delta\nu = \nu_{max} - \nu_{CoG} = \nu_0 - \nu_0'$:

$$L(\nu) = L_0 \cdot g(\nu) \cdot f_{mod}(\nu, \Delta\nu) \tag{7.5}$$

where

$$g(\nu) = \frac{\gamma/2\pi}{\nu^2 + (\gamma/2)^2} \tag{7.6}$$

and

$$f_{mod}(\nu, \Delta\nu) = \frac{k\gamma/2\pi}{(\nu - \Delta\nu)^2 + (k\gamma/2)^2} \tag{7.7}$$

For the lead isotopes, fits were performed using the full fitting function (Equation 7.2 with I_{bg}, I_0, ν_0 and γ as free parameters and using $k = 10$). To obtain a consistent set of values of ν_0 and ν_0', it was necessary to obtain fit results for different 'cutting levels' k_c ($0.3L_{max} \geq k_c \geq 0.1L_{max}$) and make a comparison. For bismuth it was necessary to use a more complex and time consuming fitting program than was used for the lead data in order to reproduce the HFS triplet substructure (more detail is given in the subsequent sections). For ease of fitting, an approximation of the double Lorentzian structure could be made by replacing it with a single Lorentzian, $L(\nu_{def}, \nu_0)$ where ν_{def} incorporates a stretching or contraction of the line profile according to a deformation paramater, β:

$$\nu' = \nu - (\nu - \nu_0) \cdot \beta \qquad \text{if } \nu < \nu_0 \tag{7.8}$$

and

$$\nu' = \nu + (\nu - \nu_0) \cdot \beta \qquad \text{if } \nu > \nu_0 \tag{7.9}$$

The following characteristics of the pure line were used to fix or constrain the fitting parameters for the other spectra:

- Doppler width $\delta\nu_D$
- Saturation power
- Lorentzian width, γ
- Asymmetry parameter, β.

7.2.2.2 HFS level spacing

The energy level spacing within the hyperfine structure is calculable to a high degree of precision by considering only the effects of the magnetic dipole and electric quadropole moments (higher-order effects are typically many orders-of-magnitude weaker) provided that the corresponding A_u, A_l and B_l hyperfine

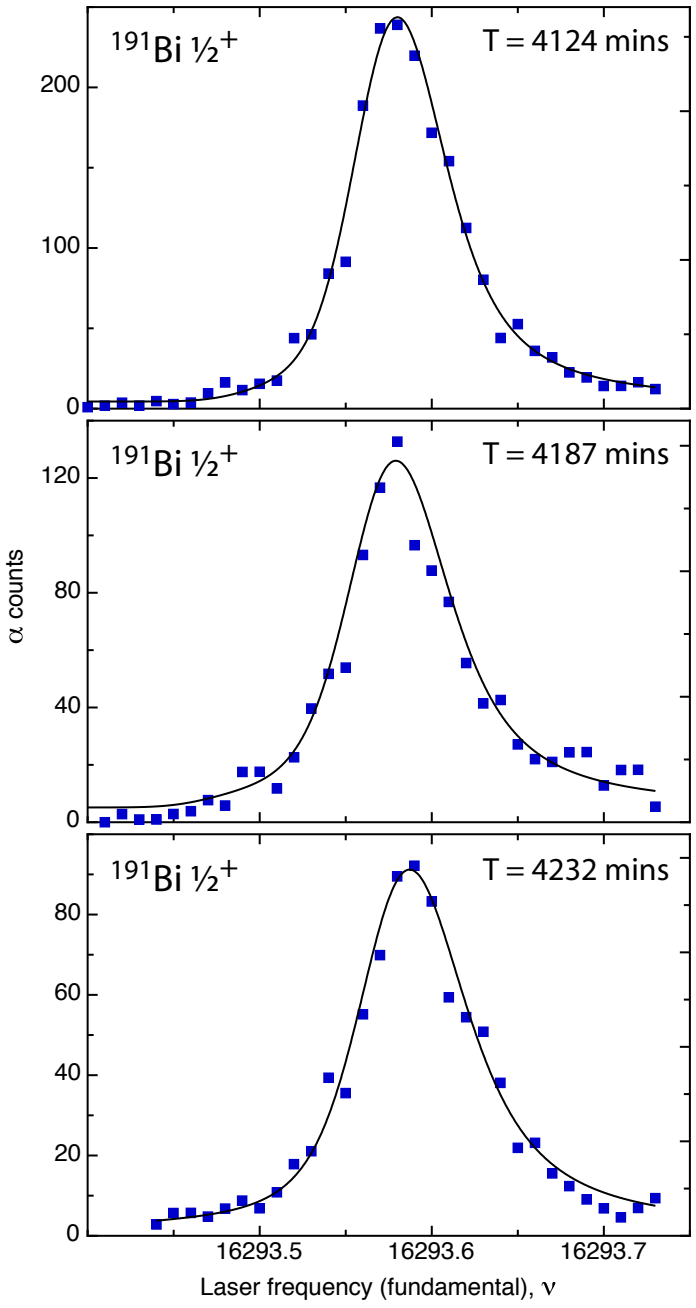

Figure 7.18: Voigt fits of the $F = 1 \rightarrow 0$ line for the ^{191}Bi $I^{\pi} = \frac{1}{2}^{+}$ isomer.

coefficients for the upper and lower atomic states, the nuclear spin, and the electronic angular momenta are known.

Using Equation 4.15, for $I = \frac{9}{2}$, the energy difference between the hyperfine levels (F) are related to the hyperfine coefficients as follows:

- For the upper $J = \frac{1}{2}$ level:

$$\Delta E^{J=1/2}_{F=4\rightarrow5} = 5A_u \tag{7.10}$$

- For the lower $J = \frac{3}{2}$ level:

$$\Delta E^{J=3/2}_{F=3\rightarrow4} = 4A_l - \frac{2}{3}B_l \tag{7.11}$$

$$\Delta E^{J=3/2}_{F=4\rightarrow5} = 5A_l + \frac{5}{24}B_l \tag{7.12}$$

$$\Delta E^{J=3/2}_{F=5\rightarrow6} = 6A_l + \frac{2}{3}B_l \tag{7.13}$$

and for $I = \frac{1}{2}$:

$$\Delta E^{J=1/2}_{F=0\rightarrow1} = \frac{A}{2} \tag{7.14}$$

$$\Delta E^{J=3/2}_{F=1\rightarrow2} = 2A \tag{7.15}$$

For the ^{209}Bi ground-state ($I = \frac{9}{2}$), the hyperfine coefficients are known from [68] to be $A(^4S_{3/2})$= -446.97(4) MHz; $B(^4S_{3/2})$ = -304.3(8) MHz and $A(^4P_{1/2})$ = +4920.8(6) MHz.

7.2.2.3 Relative line intensities

With the F level spacing fixed according to Equations 7.10 - 7.15, fitting the spectra for ^{209}Bi requires proper consideration of the relative line intensities. If the laser power is low enough so that the transition is far from being saturated, the intensities follow the relative transition probabilities given by the square of

the electric dipole transition matrix element. In this case, for a transition from a state $|J'I'F'\rangle$ to a state $|JIF\rangle$ the transition probability, P is

$$\begin{aligned} P(J'I'F' \rightarrow JIF) &= (\langle JIF||Q_l^{el}||J'I'F'\rangle)^2 \\ &= (2F+1)(2F'+1) \times (W_{FF'})^2 \times (\langle J||Q_l^{el}||J'\rangle\delta_{I,I'})^2 \end{aligned} \tag{7.16}$$

where Q_l^{el} is the electric dipole operator and the quantity $W_{FF'}$ is called the Wigner 6j symbol and is equal to $\begin{Bmatrix} J & F & I \\ F' & J' & 1 \end{Bmatrix}$.

In the event of a strong saturation of the transition, the relative transition probabilities follow the statistical weights of the corresponding F states:

$$P(J'I'F' \rightarrow JIF) \propto (2F'+1). \tag{7.17}$$

For the bismuth $I = 9/2$ and $I = 1/2$ states measured, the relative intensities given by these extremes of saturation are given in Table 7.5.

Table 7.5: Normalized relative intensities of hyperfine components of the bismuth $^4S_{3/2} \rightarrow ^4P_{1/2}$ transition for far from saturation and strong saturation conditions.

I^π	$F' \rightarrow F$	Not saturated	Saturated
$9/2^-$	$3 \rightarrow 4$	0.54	0.54
$9/2^-$	$4 \rightarrow 4$	0.51	0.69
$9/2^-$	$5 \rightarrow 4$	0.34	0.85
$9/2^-$	$4 \rightarrow 5$	0.18	0.69
$9/2^-$	$5 \rightarrow 5$	0.51	0.85
$9/2^-$	$6 \rightarrow 5$	1.0	1.0
$1/2^+$	$0 \rightarrow 1$	0.4	0.6
$1/2^+$	$1 \rightarrow 2$	1.0	1.0
$1/2^+$	$1 \rightarrow 1$	0.2	0.6

The laser power for the scanning laser was attenuated to avoid saturation and the consequential broadening of the spectral line and so a compromise was found between the ionization efficiency and spectral resolution. The optimized laser intensity is a value close to the saturation intensity and so the relative intensity distribution lies somewhere between the two sets of values given in Table 7.5.

It is important to include a fitting parameter that deals with this intermediate situation.

For a two level system, considering only the transition itself, and no optical pumping effects, $P(J'I'F' \rightarrow JIF)$ can be related to the laser intensity using:

$$P(F' \rightarrow F) = Y_{F'}(1 - \exp(-\mathrm{Z_{F\rightarrow F'} I_L})) \tag{7.18}$$

where $Y_{F'} = 2F' + 1$, $Z_{F\rightarrow F'} = (2F + 1)(W_{FF'})^2$. I_L is proportional to the laser intensity and can be included as a free parameter in the fitting routine. It follows that far from saturation where, if I_L is small with respect to $Z_{F\rightarrow F'}$, the relative intensities $P(F' \rightarrow F)_{rel}$ are proportional to the square of the matrix element as given in Equation 7.16. For saturation, where I_L is greater than $Z_{F\rightarrow F'}$, we have $P(F' \rightarrow F) \approx Y_{F'}$ and so the relative intensities are as given in the final column of Table 7.5.

The evolution of the relative transition probabilities with increasing laser intensity for the three peaks on the low energy side of the ^{209}Bi $I = 9/2$ HFS is shown in Figure 7.19.

This approach does not adequately model the experimental conditions for the excitation of the spectroscopic transition. For a pulsed laser system, the finite lifetime of the states must be considered, allowing a distribution of the relative level populations during the excitation process. The resulting relative line intensities are estimated using rate equations to simulate the atomic excitation dynamics [72]. Such an approach is described in [17]. A three-level rate equation is required to describe the three-step ionization process. A number of assumptions were made in order to simplify the fitting routine.

- There is no population transfer between upper state F levels.

- The second step is saturated and the final step is far from saturation.

- The laser linewidths of the second and third step are large (no detuning effect from scanning the first step).

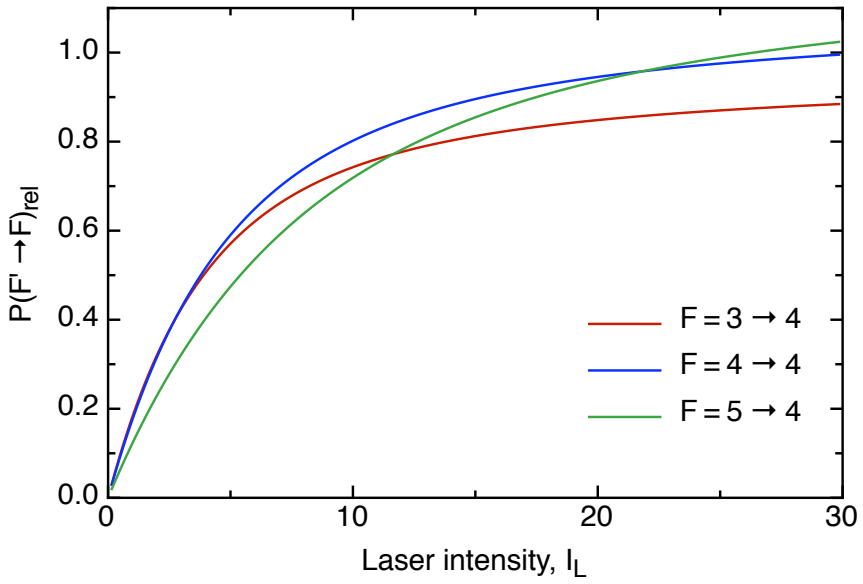

Figure 7.19: The effect of laser intensity on the transition probability for transitions from the ground-state F=3,4,5 levels to the upper F=4 level for the simple two level system described by Equation 7.18.

7.2.3 Results

For the $I = \frac{9}{2}$ spectra, since the low and high frequency sections of the complete HFS are both unresolved triplets, it was necessary to combine the separate scans into complete scans of the HFS. The value of $A(^4S_{3/2})/A(^4P_{1/2})$ was fixed using the precisely known A values for ^{209} Bi. No attempt was made to extract the quadrupole splitting, instead B was left as a free parameter but constrained to avoid a departure towards an unrealistic value. In one iteration, the positions of each peak in the HFS are determined from the free parameters: the centroid position of the complete HFS and the A and B values. Using these peak positions, the level of saturation can be determined, and this value can be used in the rate equation to determine the relative intensities of the peaks (as a separate calculation for each HFS triplet). The new relative intensities can be used in the subsequent iteration to obtain improved values for the fitted parameters.

For the fitting of the complete HFS of ^{191}Bi, $I = \frac{1}{2}$, the same procedure was used but with the added constraint that the position of the single low frequency

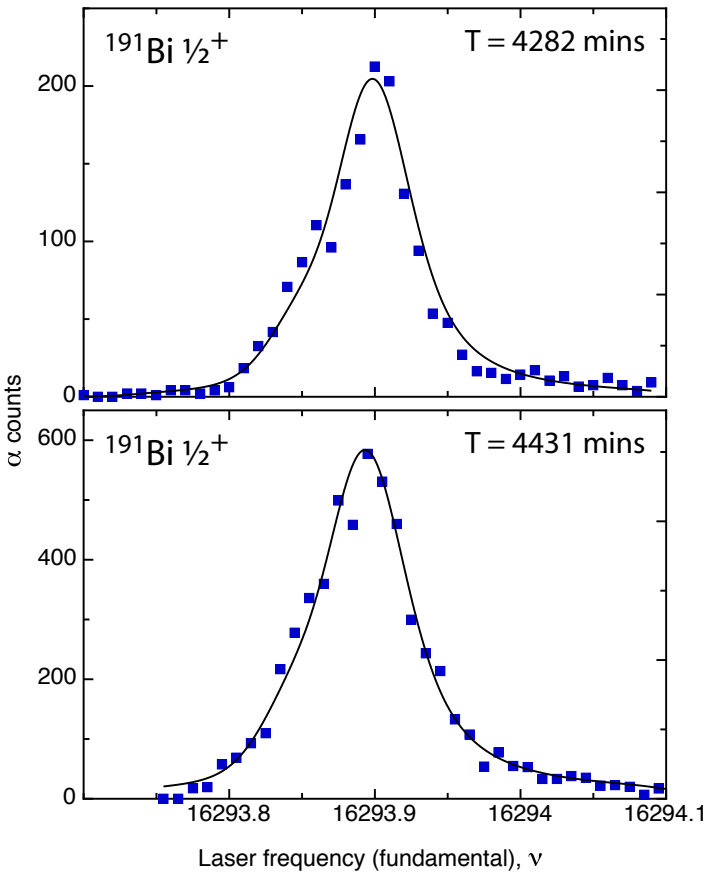

Figure 7.20: Voigt fits of the $F' \rightarrow F = 2 \rightarrow 1, 1 \rightarrow 1$ lines for the ^{191}Bi $I^{\pi} = \frac{1}{2}^{+}$ isomer. The fitting was performed with ν_0 for the $F' \rightarrow F = 1 \rightarrow 0$ transition fixed.

peak could be fixed at the value obtained from the fit of this line (Figure 7.20).

Table 7.6: An overview of the isotope-shifts and magnetic moments for bismuth isotopes. Notes:(a) [73]; (b) alternative values assuming $I = 6$; (c) [74]; (d) [75]; (e) [76]; (f) Calculated from $A(^4S_{3/2})$ using the $A(^4S_{3/2})/A(^4P_{1/2})$ ratio for ^{209}Bi.

A	I^π	$A(^4S_{3/2})$ MHz	$A(^4P_{1/2})$ MHz	μ n.m.	Isotope Shift MHz	Ref.
189	$9/2^-$	–405.5(27)	+4464(27)$^{(f)}$	+3.729(3)	–21790(300)	this work
191	$9/2^-$	–403.7(12)	+4444(12)$^{(f)}$	+3.704(11)	–17894(200)	this work
191m	$1/2^+$	–24.2(2)	+266(2)$^{(f)}$	+1.477(9)	–20380(200)	this work
202	$5^{+(a)}$	–405(10)	+4590(14)	+4.259(14)	–10267(58)	[68]
202	$(6^+)^{(b)}$	–343(7)	+3884(12)	+4.325(14)	–10520(58)	[68]
203	$9/2^{-(a)}$	–433(6)	+4810(15)	+4.017(13)	–8303(54)	[68]
204	$6^{+(a)}$	–332(32)	+3881(13)	+4.332(15)	–7681(85)	[68]
205	$9/2^-$	–437.0(10)	+4867(6)	+4.065(5)	–5632(21)	
206	6^+	–356.1(15)	+3916(6)	+4.361(8)	–4926(23)	
207	$9/2^-$	–443.99(24)	+4897.9(8)	+4.0915(9)	–2992(2)	[68]
208	5^+	–462(5)	+4993(9)	+4.578(13)	–1578(17)	
209	$9/2^-$	–446.97(4)$^{(c)}$	+4920.8(6)	+4.1106(2)$^{(d)}$	0	[68]
210	1^-	+21.78(3)$^{(e)}$	-	–0.04451(6)$^{(e)}$	+2495(85)	
210m	9^-	–147(6)	+1633(25)	+2.72(12)	+2463(42)	
212	1^-	-	+1727(207)	+0.321(38)	+7761(104)	
213	$9/2^-$	–339.3(18)	+4449(7)	+3.716(6)	+10507(24)	

7.2.4 Magnetic moments of ^{189,191}Bi

Since the spin assignments were already known for the bismuth isotopes studied, their magnetic moments could be calculated using the experimentally measured values for the lower-state hyperfine coupling coefficient, A_l. This was done using the magnetic-moment scaling relation (Equation 4.19) using ^{209}Bi as the calibration isotope (For ^{209}Bi: A_l = -446.97(4) and μ = +4.1106(2)μ_N and $I = \frac{9}{2}$). Spectroscopic measurements with RILIS do not have sufficient resolution to observe the hyperfine anomaly effect so this was neglected.

In Figure 7.22 the deduced magnetic moments for ^{189,191}Bi are shown alongside earlier measurements for the $I = \frac{9}{2}$ isotopes.

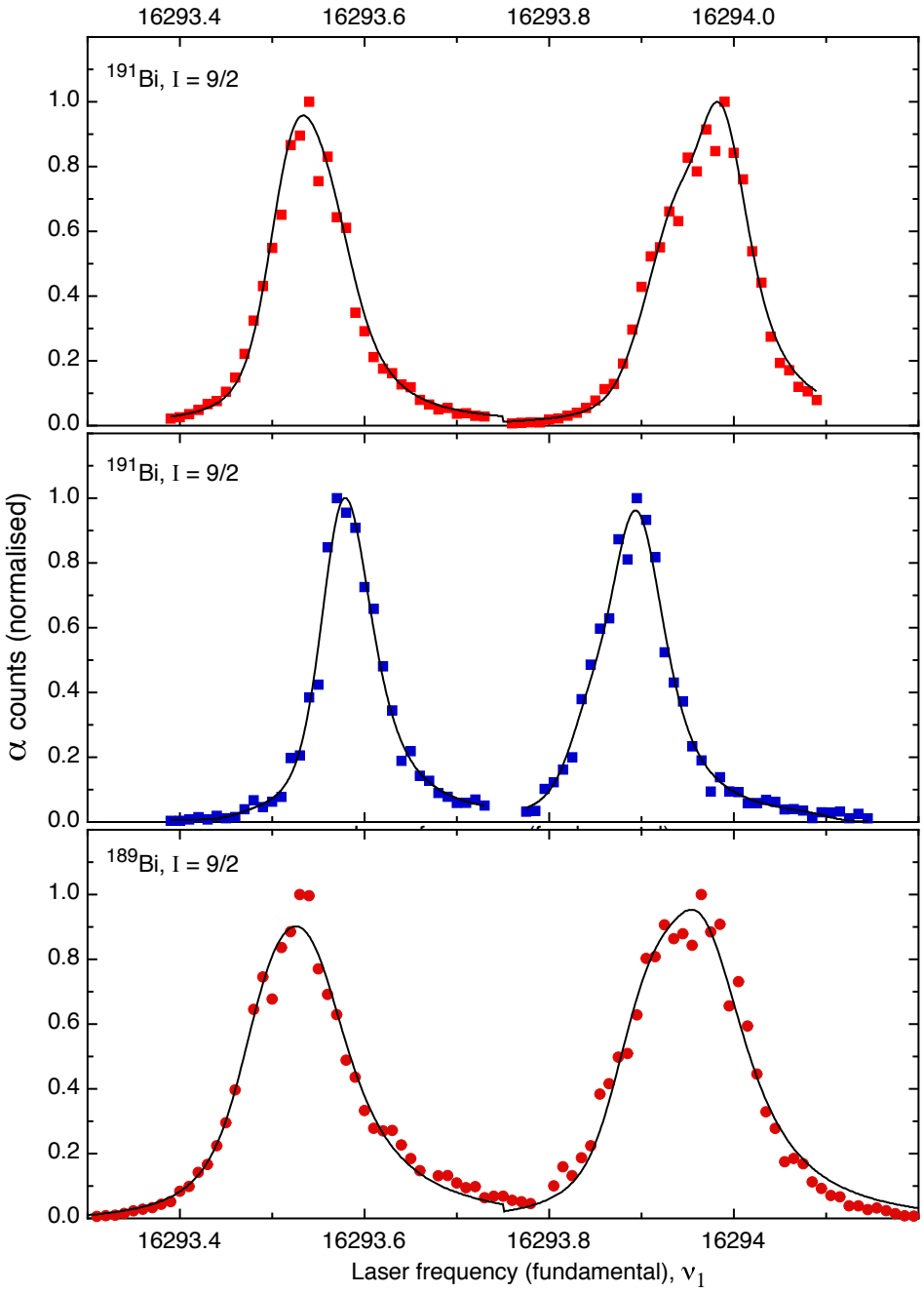

Figure 7.21: The fitted HFS scans for ^{189,191,191m}Bi. The spectra are normalized for ease of display and the fitting of each HFS triplet was performed separately.

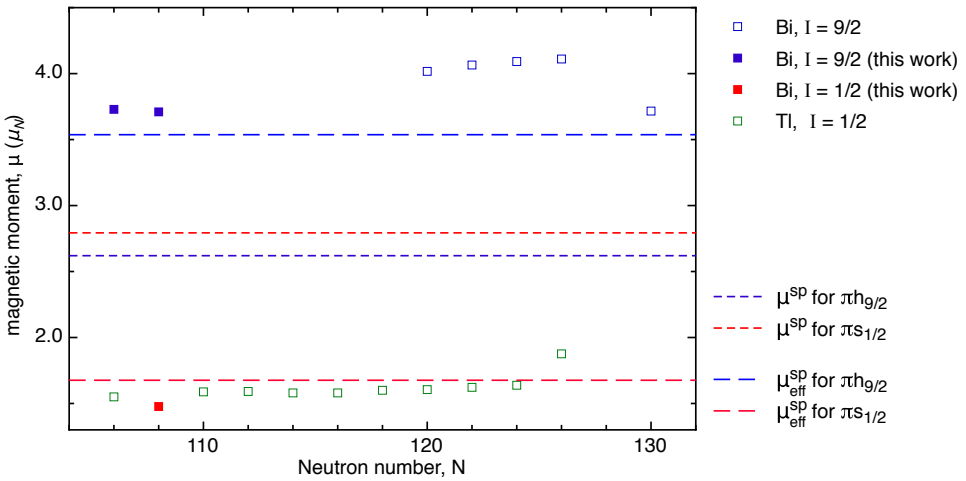

Figure 7.22: The magnetic moments of bismuth isotopes with $I = \frac{9}{2}$ and $I = \frac{1}{2}$. The predicted single-particle moments calculated from the intrinsic and effective proton g-factors are indicated.

The nuclear shell model provides a means of estimating the magnetic moment, $\mu_{s.p}$ for a pure single-particle configuration (the *Schmidt moment* [77]) using

$$\mu_{s.p} = j(g_l \pm (g_s - g_l)\frac{1}{2l+1}) \tag{7.19}$$

where g_s and g_l are the free nucleon spin and orbital g-factors respectively and $j = l \pm \frac{1}{2}$.

The new measurements for the $I = \frac{9}{2}$ states are consistent with earlier observations in the chain of the heavier isotopes in that they lie significantly above the predicted single-particle (Schmidt) values calculated for a proton in a $h_{9/2}$ orbital ($+2.62\ \mu_N$). Explaining departures from single-particle behaviour requires discussion of collective phenomena where the inner nucleons also play a role. The large deviation from the single-particle estimates for magnetic moments is explained qualitatively by M1 core polarization effects. A strong dependence of the core polarization on the occupancy of the proton valence shells has been demonstrated [78] and is characteristic of nuclei near magic shell closures. This effect is particularly strong if the filled core is a $J = l + \frac{1}{2}$ orbital and the valence particle sits in the neighboring $J = l - \frac{1}{2}$ partner. For bismuth this is the case: the valence proton occupies a $h_{\frac{9}{2}}$ orbit and core polarization is attributed to spin-flip

transitions involving an $h_{\frac{9}{2}}$ to $h_{\frac{11}{2}}$ particle-hole excitation. Even a small (1 %) mixture of this configuration with the pure $h_{\frac{9}{2}}$ wave function can strongly influence the magnetic moment due to the high strength of the allowed M1 transition from the 0^+ (g.s) to the 1^+ (particle-hole) nuclear core configuration. Magnetic moment predictions for complex nuclear systems are usually made using an effective g-factors, g_{eff}, which are adjustments to the intrinsic values to take into account this type of configuration mixing and also exchange current effects. For the heavy elements, an adjustment to the value of g_s by a factor of between 0.6 and 0.7 is commonly used [79]. The magnetic moment corresponding to $g_{eff} = 0.65\ g_s$ is indicated in Figure 7.22. This line shows a much closer agreement with the experimental values but still underestimates the extent of the departure from the single-particle calculation. In addition to core polarization, meson (π, ρ, ω) exchange between the valence proton and the core could be contributing to the shift in the magnetic moments but these effects are usually small and are unlikely to be influencing the magnetic moment by more than 5 %.

For the earlier measurements from $N = 130$ – 119, the deviation from the single-particle estimate is at a maximum at the N = 126 shell closure and the new measurements for the light isotopes approaching $N = 104$ indicate a continuation of downward sloping trend towards the mid shell.

The deduced magnetic moment of +1.477(9) μ_N for the ^{191}Bi $I = \frac{1}{2}$ isomer is a deviation of comparable magnitude from the predicted Schmidt moment for a single $s_{1/2}$ proton (+2.793 μ_N). As indicated in Figure 7.22 the use of a g_{eff} value of 0.65 g_s provides a closer prediction of the magnetic moment. The analysis of this 'quenching' of the single-particle magnetic moment is simplified by the study of single-particle or hole orbits with $l = 0$, for which the orbital contribution to the magnetic moment, g_l is zero. Such a system has been previously investigated by the study of the thallium $I = \frac{1}{2}$ isotope chain extending from $N = 106$ to $N = 125$ using the atomic beam magnetic resonance (ABMR) technique [80]. With respect to the discussion of departures from single-particle behaviour, the most interesting measurement of the thallium isotopes was the determination of the magnetic moment for ^{207}Tl which was measured at ISOLDE by Neugart et al. in one of the early COLLAPS experiments [81]. ^{207}Tl is the only heavy isotope with a single $s_{1/2}$ particle in addition to a doubly magic core. As such, it provides

an ideal opportunity to use the experimentally deduced magnetic moment to investigate the influence of first-order core polarization on the effective value of g_s in a system with a relative absence of contributions from higher-order or orbital specific effects. For ^{207}Tl, a theoretical prediction of the magnetic moment ($\mu = +1.80\ \mu_N$) based upon first-order core polarization plus pion exchange and vibrational state coupling [82] comes close to the experimentally determined value ($\mu = +1.876(5)\mu_N$). By singling out this dominant first-order core polarization effect, the subsequent discussion of the lighter thallium moments was simplified, with the magnetic moment fluctuations relative to the value for ^{207}Tl giving a direct insight into the higher-order core polarization contributions. The close agreement of the new result for the ^{191}Bi $I = \frac{1}{2}$ isomer with the magnetic moments of the light thallium isotopes confirms the analogous nature of these effects at the other side of the magic proton shell closure.

7.2.5 Isotope-shifts of ^{189,191}Bi

The ^{189,209}Bi, ^{191,209}Bi and ^{191m,209} Bi isotope-shifts have been measured by comparison of HFS centroid positions for the optical spectra of the radioactive isotopes with a calculation of the centroid position for the ^{209}Bi HFS using Equation 7.1. As was described in Chapter 4, the isotope-shift is formed from a field (or volume) shift and a mass shift. For the heavy elements such as bismuth, the mass shift contribution is insignificant and the field shift can be considered solely responsible for the isotope-shift. To a good approximation, the isotope-shift can therefore be considered to be directly proportional to the change in mean-squared charge radii. This assumption enables the discussion of the differential changes in charge radii using isotope-shift measurements alone, without the need to consider the atomic factor F_i. For bismuth, a reliable calculation of F_i is complicated by the significant change in the electron screening for the atomic transition used [24].

A good starting point for the discussion of charge radii systematics is the comparison with a spherical system. Often such a system can be produced by performing the droplet model calculations described by Myers and Schmidt [83]. Fortunately, in the discussion of charge radii systematics near the magic $Z = 82$ proton number, such approximations are not required because a realistic, near

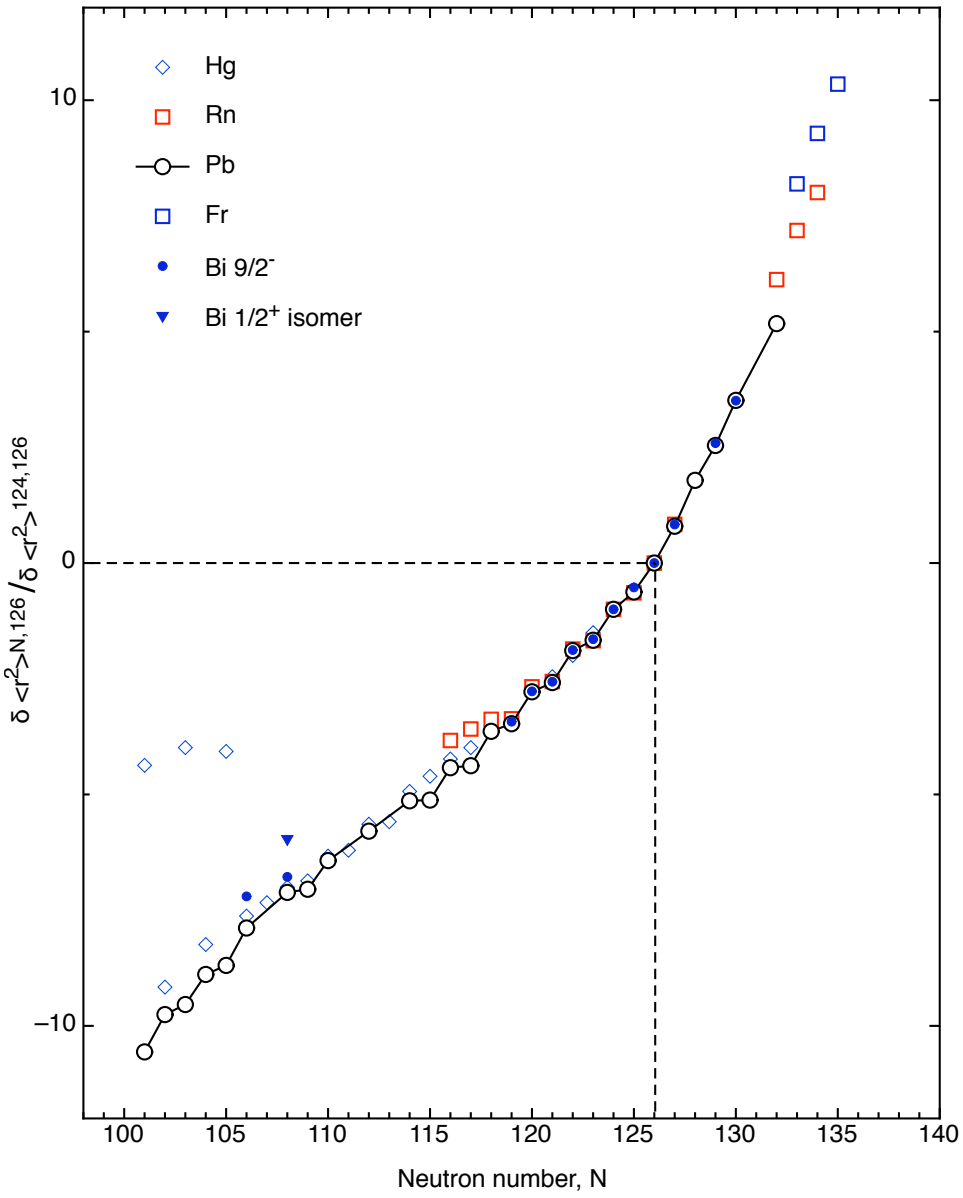

Figure 7.23: A comparison of the Bi, Hg, Rn, Pb, and Fr relative isotope-shifts with each chain normalized to IS(N=124,N′=126)=1.

spherical reference point is provided by the wealth of experimental data for the lead chain. The charge radius of the doubly-magic ^{208}Pb nucleus shows very close agreement with the spherical droplet model prediction but this agreement does not hold along the lead chain towards the proton drip line. In addition to the observation of the odd-even staggering, from $N = 115$ ($A = 197$), the charge radii exhibit an increasing departure from the droplet model with a reduction in neutron number. This feature of the charge radii systematics reaches a maximum close to the $N = 104$ mid shell. Features observed in plots of the change in mean-squared charge radii (e.g. Figure 7.7) are usually a good indication of the onset of nuclear shape changes and the extent of deformation. In the case of the lead chain, the values obtained for the quadrupole moments for these nuclei ($\langle\beta_2^2\rangle = 0.11$ for $^{190-184}$Pb and 0.09 for ^{182}Pb [67]) imply a near spherical shape. The charge radii for lead are interpreted with some degree of success using Beyond Mean Field [84] and Interacting Boson Model approaches [85],[86].

The charge-radii systematics in the vicinity of Z = 82 including the new measurements for bismuth are presented in Figure 7.23. In the discussion by Pearson et al [68] of the isotope-shifts for the bismuth isotopes near stability, the relative isotope-shifts for lead, bismuth and polonium were plotted in the same way as in Figure 7.23 and the incredible reproduction of small scale structures such as the odd-even staggering within the isotope-shift trend for nuclei with Z greater than 82 is highlighted. Across the nuclear landscape, this behaviour is unique to the isotopes near $N = 126$ with Z close to but greater than 82.

Whilst clearly illustrating correlations in charge-radii systematics, the relative isotope-shift plot also enables easy identification of any differential changes between isotones. Using the lead chain as a spherical reference point, the plot highlights any onset of deformation as a drift from the exact overlap of the data points. In Figure 7.23, an example of such a departure is seen in the radon chain starting at $N = 120$. In the discussion by Pearson et al [68] of the heavier neutron-deficient bismuth isotopes, the polonium isotopes show the same departure occurring slightly lower in neutron number. The new measurements presented here give the first convincing picture of the same effect for bismuth. The extent of the departure from overlap for the ^{200}Pb, ^{204}Rn isotone pair is seen for the ^{190}Pb, ^{191}Bi pair, ten neutrons further from stability. Using the deformed

droplet model of Myers and Schmidt [77], the mean-squared charge radius $\langle r^2 \rangle$ for a non-spherical nucleus is estimated from the quadrupole deformation parameter, β_2 using

$$\delta\langle r^2 \rangle = \delta\langle r^2 \rangle_{spherical} \left[1 + \frac{5}{4\pi} \langle \beta^2 \rangle \right] \tag{7.20}$$

assuming a negligible contribution from higher-order β_i and γ terms such as the octopole deformation and for a constant nuclear volume.

This model has been used to estimate a β_2 of ~ 0.09 for the isotopes $^{183-194}$Pb [67]. Continuing the assumption that the nuclei are spherical near the doubly magic ^{208}Pb ($\beta_2 = 0$), the required β_2 values to account for the relative isotope-shift plotted in Figure 7.23 for ^{191}Bi and ^{189}Bi are ~ 0.10 and ~ 0.12 respectively. As a comparison, the dramatic shape changes observed in the neutron-deficient mercury isotope chain is representative of $\beta_2 \approx 0.25$. It is difficult to apply the same discussion to the ^{191}Bi $I = \frac{1}{2}$ isomer since its nuclear state involves the promotion of an $s_{1/2}$ proton into the $h_{9/2}$ orbital. As such, an increased charge radius is expected due to the dependence of $\langle r^2 \rangle$ on the principal quantum number.

7.3 An alternative ionization scheme for bismuth

Bismuth proved a particularly difficult case during the resonance ionization study on account of the need to scan the two widely spaced HFS triplets separately. A new Bi ionization scheme has been developed for which the resonant transition following the spectroscopic transition is significantly broader so that a scan of the first-step frequency across the complete HFS would not result in a large detuning effect. As additional benefits, the transition is to a strong auto-ionizing resonance and so could provide an improvement in the RILIS efficiency over the current three-step scheme that relies on non-resonant ionization. For spectroscopy purposes, the use of a two step ionization scheme removes a level of complexity from the system, simplifying both the corrections for laser fluctuations and the modeling of the ionization process (two-level system).

From the $^4P_{1/2}$ at 32588 cm^{-1}, the continuum lies 26173 cm^{-1} away (accessible with a $\lambda < 380$ nm photon). At the time of this work, seven auto-ionizing levels were known within the 59000 - 65000 cm^{-1} range [87] but attempts had not been made to access them via a transition from the $^4P_{1/2}$.

7.3.1 Atomic beam RIS of stable Bi above the ionization potential

The search for a strong transition from the $^4P_{1/2}$ level to an efficient auto-ionizing state was conducted off-line in Manchester using a purpose built atomic beam unit (a laser ionization chamber with an ion detector) coupled with a low repetition rate pulsed dye-laser system. The vacuum chamber of the atomic beam unit (ABU) was a somewhat modular system in which an atomic vapour of ^{209}Bi could be prepared either by pulsed laser desorption of a solid bismuth sample, or by evaporation of powdered bismuth within a resistively heated oven.

Figure 7.24 illustrates the ionization chamber setup. The system is rather modular; in the figure the standard configuration is shown, with a bismuth oven in place and signal detection using an electron multiplier. The oven can be easily replaced by a pulsed laser ablation region. The electron multiplier can also be removed and the chamber can be sealed with a sapphire window to enable fluorescence detection using a photo-multiplier tube. For the creation of an atomic vapour by pulsed laser desorption, a focused beam from a second 10 Hz Nd:YAG laser, with ∼30 mJ/pulse and operating at 10 Hz and 1064 nm was available. When focussed onto a bismuth target, an intense plume of bismuth is released into the laser interaction region for a short time following the laser pulse (μs). It has been shown that the neutral fraction within the ablation plume can be high and the plume is released at the normal to the target surface, regardless of the incident angle of the ablation pulse. The dynamics of this ablation process is discussed in reference [88]. Alternatively, bismuth vapour could be released from a small joule heated graphite tube. The tube, filled with powdered bismuth, operates at 5V and the heating current of approximately 6 A results in a steady release of bismuth for over three hours at a vacuum pressure of 4×10^{-6} mbar. The lasers used were a 10 Hz Nd:YAG pumped Spectra-Physics pulsed dye laser and a 20 Hz

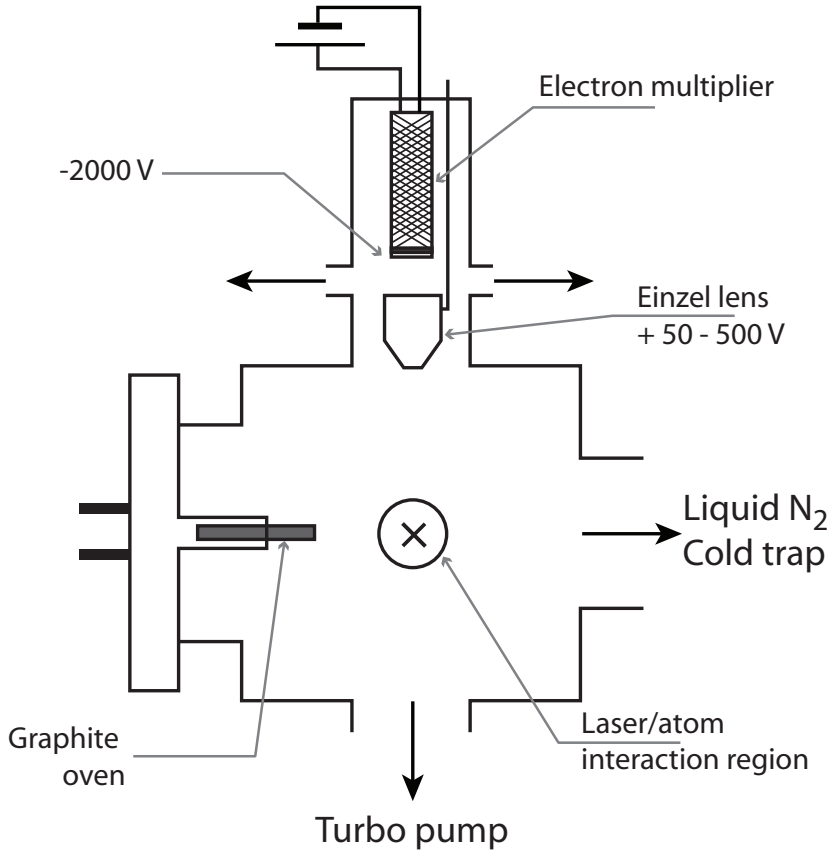

Figure 7.24: The ionization chamber configuration used for RIS of an atomic vapour released from an oven. For sample preparation by pulsed laser desorption, the oven can be replaced by a solid target and access for the ablation laser is provided by replacing the cold trap section with a flange fitted with a window.

Lumonics Nd:YAG pumped HyperDYE laser system. This latter was located in a separate laboratory and so its frequency doubled output beam was delivered to the ABU using a multi-mode UV optical fibre. In order to ensure the necessary temporal overlap (± 2-3ns) of the pulses from the two lasers, the flashlamp for the Lumonics laser was triggered with a delayed signal from the Brilliant YAG flashlamp monitor. Using the signal control box of the Lumonics Nd:YAG laser, this flashlamp pulse was adjusted and delayed to provide the Lumonics Q-switch trigger. A delayed signal from the Lumonics Q-switch provided the trigger signal for the Q-switch of the second Nd:YAG pump laser. Whilst observing the laser pulses at the experimental set-up using a photodiode a fine adjustment of the delays enabled the pulses to be overlapped.

Calibration of the laser frequencies was performed by passing the beam through a neon discharge tube, making use of the optogalvanic effect. As the laser frequency is scanned to resonance with a spectral line of neon, the resulting excitation affects the current flow through the tube which can be monitored on an oscilloscope. On account of the rich spectrum of atomic neon within the relevant frequency range, this is a precise and convenient calibration tool. The neon lines observed are listed in Table 7.7.

Table 7.7: Neon absorption lines used for PDL calibration. The atomic spectral line data are taken from the Kurucz database [40]

Wavelength air,nm	Energy,E1 cm^{-1}	Config.	Energy,E2 cm^{-1}	Config.	Resonance shape[a]
609.6163	134459.29	3s*[1+]	150858.508	3p'[1+]	UP
616.3594	134818.64	3s'*[0+]	151038.452	3p'[0+]	UP
621.7281	134041.84	3s*[1+]	150121.592	3p[1+]	UP
626.6495	134818.64	3s'*[0+]	150772.112	3p'[1+]	UP
630.4789	134459.29	3s*[1+]	150315.861	3p[1+]	UP
633.4428	134041.84	3s*[1+]	149824.221	3p [2]	UP
638.2991	134459.29	3s*[1+]	150121.592	3p[1+]	DOWN
640.2246	134041.84	3s*[1+]	149657.042	3p[2+]	UP

[a] The resonance shape, UP or DOWN, refers to the orientation of the second part of the resonance signal

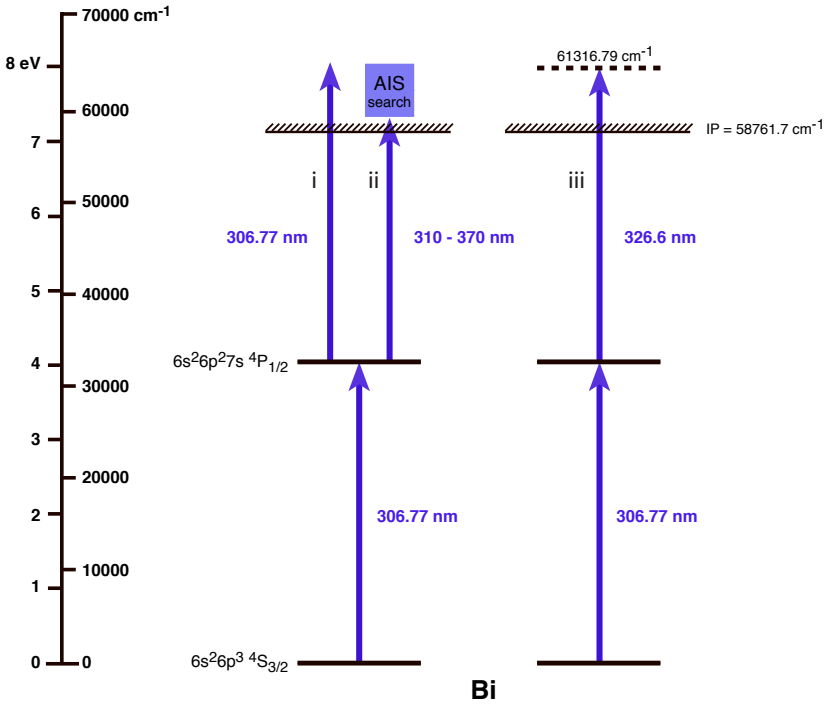

Figure 7.25: An energy level diagram illustrating the stages of the RIS study: i) Initial testing and optimization with the one-colour, two-step scheme; ii) Scanning with a second laser across the emission range of the DCM dye; iii) The new ionization scheme using an AIS.

Both DCM and Rhodamine 6G dyes were used in the RIS study. Pumped by light at 532 nm (the Nd:YAG 2^{nd} harmonic), these dyes cover a broad region within the visible spectrum, from ~605 - 660 nm. Frequency doubling of the fundamental output was performed using a BBO crystal in a configuration similar to that used at RILIS (Section 5.4). After doubling, the scanning range is ideal for an AIS search in an energy range just above the ionization potential. The extent of the RIS scanning range is illustrated in Figure 7.25. If the laser pulse energy is sufficiently high, bismuth can be resonantly ionized in a two-step process using only one laser beam at the wavelength for the first step in the RILIS ionization scheme (306.77 nm). This provided simplified ionization conditions for the characterization and optimization of the system.

Using this single-colour ionization scheme the first attempt at RIS inside the

ABU were performed using pulsed laser ablation to create the atomic vapour of the sample. The atomic plume produced by laser ablation is accompanied by a large plasma cloud. In the simple geometry of the small atomic beam unit this is particularly difficult to suppress and is detected by the electron multiplier as a large, sharp ion signal with a long fall off time. Using NIM electronics: a timing filter amplifier, gate and delay generator, constant fraction discriminator and a coincidence unit it was possible to establish a gated detection system and search for the laser ions within a small adjustable (0 - 100 μs) time window following the ablation pulse. Despite these measures, it was not possible to observe a reproducible laser ion signal.

The background count rate is greatly reduced if the atomic vapour is created inside a resistively heated oven. The oven is a long narrow graphite tube. Due to the geometry of the tube (with a length much greater than the width), bismuth vapour originating from the bismuth powder at the base of the oven, is well collimated, enabling efficient transfer to the nearby laser interaction region. With the laser frequency of the first laser optimized for maximum ion count rate at a given laser power, the power was then reduced to a level at which the ion signal falls close to the background level (a few counts per second). At this level, any enhancement in the ion signal resulting from the interaction with a second laser beam is clearly seen. Within the spectral tuning range of the DCM dye, one AIS was observed, located at an energy of 63196.79 cm^{-1}. This resonance is shown in Figure 7.26. The FWHM of this AIS is approximately 25 GHz, similar in size to the HFS of the odd bismuth isotopes. This is not large enough to enable a complete HFS scan of the first excitation step without an observable detuning from resonance of the second step but this scheme may be advantageous in terms of RILIS efficiency and stability during the long scanning times involved.

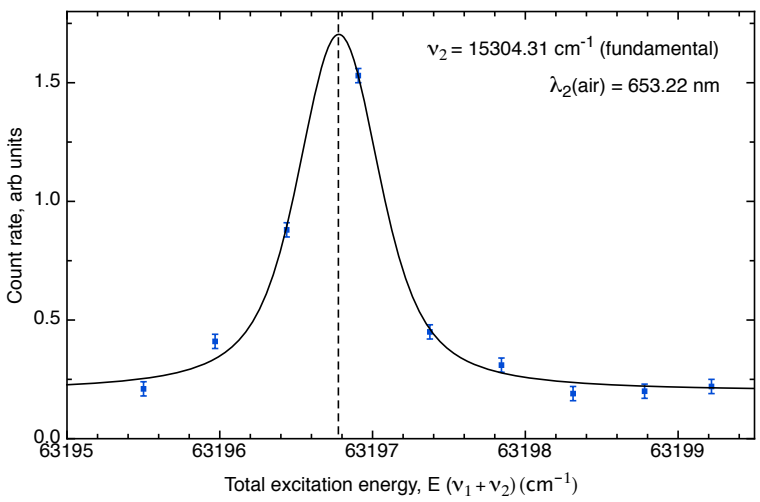

Figure 7.26: The scan of the AIS resonance at 63196.79 cm^{-1}

Chapter 8

FURIOS development work at the JYFL IGISOL

8.1 Introduction

The Fast Universal Resonance Ion Source, FURIOS is a new addition to the IGISOL facility at the Jyväskylä Accelerator Laboratory. Much of the development work carried out for the FURIOS project forms part of the laser activity contribution to the sixth framework programme of the EUROpean Nuclear Structure Research programme (EURONS) within a working group comprised of the LARISSA (Mainz), LISOL (Leuven), RILIS (ISOLDE) and IPN (Orsay). Specifically, the work described here was partly funded by the Marie Curie fellowship programme.

The motivation for laser ion source development at the IGISOL is the high degree of selectivity and significant improvement in ion-beam intensities that are to be expected. In combination with the fast release of radionuclides from the IGISOL target, these improvements could enable experiments to be conducted within previously unattainable regions of the nuclear chart.

The success of a laser ion source relies upon the availability of the sample in atomic form and as such, coupling laser ionization with the IGISOL is not a simple task. The first challenge is operating in 'atom guide' as opposed to 'ion guide' mode, requiring an adaptation of the gas-cell parameters to optimize the production of atomic reaction products. Additionally, a good temporal and

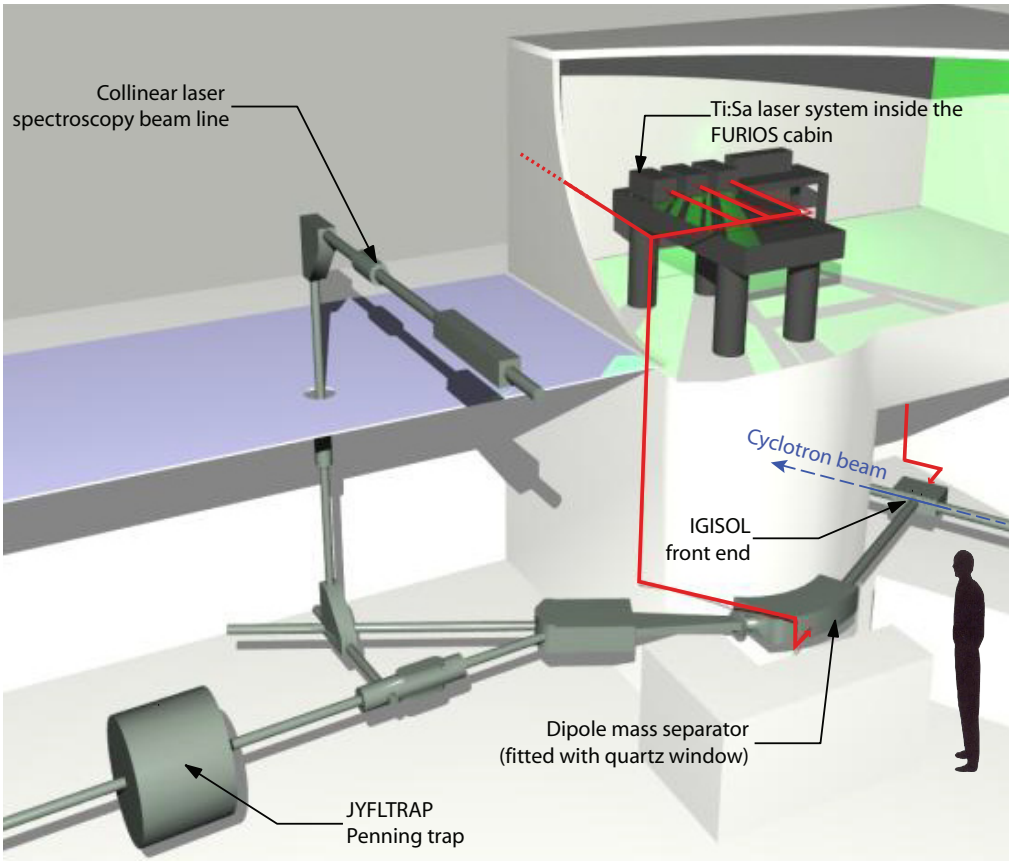

Figure 8.1: The IGISOL beam line layout showing the two laser beam access routes to the gas cell.

spatial overlap of the laser beams with the release of the atomic sample must be achieved.

The geometry of the IGISOL beam line (Figure 8.1) and the flexibility of the gas-cell design allows many means of laser access to be considered. In preparation for the laser ion source installation, the dipole magnet for the mass selection stage in the beam-line was replaced with one fitted with a quartz window to give a line of sight from this window, along the beam axis and through the nozzle of the gas cell. With laser access possible from the mass separator side of the gas cell, two distinct options for laser/atom interaction are apparent: ionization *inside* the gas cell and ionization *outside* the gas cell.

Both of these approaches are discussed below but the experimental study

presented in this chapter was conducted with ionization outside the gas cell in mind. Clearly, the efficiency of such an approach is reliant on a good overlap of the atomic sample with the laser beams. A study of the gas flow characteristics outside the gas cell is presented. An adaptation of the gas parameters both inside and outside the gas cell is suggested as a means of producing a narrow gas jet.

8.1.1 Ionization inside the gas cell

As illustrated in Figure 8.1, the lasers can be transported to the front end through a hole in the roof of the IGISOL cave. They be focussed inside the volume of a custom gas cell fitted with a quartz window. In this configuration, ionization takes place in the gas cell itself. Laser ionization in a gas cell has been extensively tested at the Leuven LISOL facility [89] and the development of this part of the FURIOS project is being carried out in close collaboration with this group, with results of initial testing described in [90].

The application of the laser resonance photo-ionization within a gas cell has been demonstrated at the LISOL facility where Ni, Co, Mn, Ti, Fe and the refractory elements, Rh and Re have been ionized with efficiencies approaching 10% in the best cases. One of the striking findings from this development has been the high sensitivity to the presence of impurities in the buffer gas. Changes in gas purity, even on the ppb level can have a dramatic effect on the photo-ion survival.

In the standard 'ion guide' mode of operation, the IGISOL is optimized for the predominant release of reaction products in a 1^+ charge state. In on-line operation, this process is somewhat dependent on the recoil energy and initial charge-state distribution of the reaction products and the final charge-state distribution is a consequence of a series of charge-exchange collisions and recombination processes. The complexities are discussed in some detail in [91] but it is important to note, that for most elements the second ionization potential is lower than the first ionization potential of helium and so the reduction to a 1^+ charge state cannot be solely a result of collisions with He atoms. In fact, the presence of molecular impurities such as O_2, H_2O, and so on, greatly enhance the process of charge-state reduction.

The laser ion source efficiency is given by,

$$\eta = \eta_{neutralisation} \cdot \eta_{ionization} \cdot \eta_{extraction}. \tag{8.1}$$

This presents some difficulties when trying to optimize the IGISOL for operation as a laser ion source. We have seen that the presence of impurities greatly increases the neutralization process, but, as has been demonstrated at the LISOL facility, these impurities can also dramatically reduce the survival rate of the laser ions prior to extraction.

To aid the neutralization process, the stopping power of the buffer gas can be improved by increasing the gas pressure. However, for spectroscopic applications of the laser ion source, where the goal is to precisely measure the positions of hyperfine components or the extent of the isotope-shift, it is important to limit the degree of pressure broadening of the spectral lines. The gas-purity requirement is an element-dependent parameter. At the Leuven IGLIS, great care has been taken to ensure high gas purity whilst optimizing the cavity design and laser interaction geometry for efficient extraction of the laser ions. The atom storage time is long on account of the large gas-cell volume and the laser interaction region is close to the exit nozzle of the gas cell. With the current gas delivery and purification system, the IGISOL cannot achieve a comparable level of gas cleanliness. Additionally, with shorter atom storage time and a laser access geometry resulting in ion creation across the entire length of the gas cell, the efficient application of the laser ionization within the gas cell is challenging.

The first demonstration of laser resonance ionization in the JYFL IGISOL was the PhD work of I. Moore in 2001 [92]. The purpose of this work was the study of ^{208,209}Bi by resonance ionization spectroscopy. Previously, the optical measurements of nuclear ground-state properties at the IGISOL required transport of an ion beam along the collinear laser spectroscopy beam line, where laser fluorescence spectroscopy is carried out on the ion beam. As discussed in Chapter 7, resonance ionization spectroscopy enables such measurements to be made with an unrivaled level of sensitivity.

The drawback of this technique is the loss of resolution due to the higher laser linewidth of the pulsed lasers, the large velocity spread of the atoms and the collisional broadening of the atomic lines within the high-pressure environment.

At the ISOLDE facility, where the flow of atoms within the hot interaction region is an effusion process and the atom motion is Brownian, the resonance linewidth is dominated by Doppler broadening of the atomic transitions. Operating at room temperature, Doppler broadening is still significant but does not fully account for the resonance profile in the IGISOL gas cell. Additionally, a broadening of the spectral lines occurs due to the collisions between excited ions and atoms of the buffer gas. Such collisions interfere with the atomic wavefunction, shortening its effective lifetime and broadening the energy width of the state. The lifetime of the excited state can be effectively reduced if the gas pressure is high enough for the mean time interval between collisions to be considerably shorter than the natural lifetime of the excited state. The effective linewidth is then the sum of the natural linewidth and the pressure-dependent collisional linewidth. For bismuth the pressure broadening factor is ≈ 10 MHz/Torr in argon [93].

Ionization inside the gas cell offers the following advantages:

- Increased resolution due to lower Doppler broadening (room temperature).[1]
- Greater residence time within the laser interaction region; the atom evacuation time from the gas cell is typically 1 ms which is long compared to the transport time of atoms across the SPIG structure (~ 100 μs).
- Significant pressure broadening: This is helpful because it allows a narrow-bandwidth laser to excite all atoms in the Doppler-broadened profile simultaneously.

It is expected that this means of ionization is likely to prove the most efficient for the production of intense ion beams. Unfortunately, aside from any attempts to improve the neutral fraction within the gas cell, the element selective laser ionization is not decoupled from the standard IGISOL system and so it is likely that a significant ion background will be present within the beam. In some cases, due to the higher selectivity of the IGISOL reaction mechanism (particularly for

[1] This is beneficial for resonance ionization spectroscopy but, for ionization with broadband lasers (> 1 GHz) a reduction in Doppler broadening has a negative effect on the ionization efficiency since only the resonant component of the laser frequency gives rise to resonant excitation.

light-ion or heavy-ion induced fusion evaporation reactions), it is unlikely that the ionic background will prove as problematic in terms of isobaric contaminants as the surface ionized fraction present in ISOLDE RILIS beams due to the higher selectivity of the IGISOL reaction mechanism.

8.1.2 Ionization outside the gas cell

With access through the dipole magnet and the lasers following a collinear and counter-propagating path with the ion beam, the possibility exists for laser ionization outside the gas cell within an interaction region close to the exit nozzle. Atoms are transported by gas flow from the gas cell into the laser interaction region immediately downstream of the gas-cell nozzle. It is clear that efficient ionization will require a good overlap of the reaction products within the gas jet with the counter-propagating laser beams. This is not trivial since the saturation of the atomic transitions requires a high photon flux, and therefore a small laser beam diameter.

In this chapter, the advantages of this option are discussed, as are the design considerations to ensure efficient operation. An off-line study of the gas flow characteristics outside the IGISOL gas cell has helped to determine some important optimal operating parameters and necessary design modifications for the laser interaction region. The results of this study are presented in this chapter and details of the laser interaction chamber, based on a RF-sextupole ion beam guide (SPIG) are given. Additionally, the results of the first test of laser resonance ionization within the SPIG are presented.

Ionization outside the gas cell offers the following advantages:

- Pure isotope and isomer beams by complete suppression of ionic isobar background of gas-cell ions.
- Potential for 'in-source' RIS on short-lived isotopes (sub-millisecond).

The characteristics that contribute to making this ionization option particularly well suited for laser spectroscopy measurements inevitably inhibit its potential in terms as a highly-efficient ion source. Additionally, this development work represents the first time laser ionization has been applied immediately outside an

ion guide gas cell. Because of this, the challenge of efficient extraction of reaction products in atomic form followed by efficient laser ionization is being addressed for the first time.

8.1.3 The radio-frequency sextupole ion beam-guide

The application of a gas-filled RF-multipole trap for laser ion sources has been demonstrated off-line at the LARISSA facility, Mainz [94] and is in development at the TRIUMF TRILIS facility, Vancouver. Incorporating a hot-cavity laser ion source, the Mainz LARISSA has a front end analogous to that of the ISOLDE target/ion source unit and their motivation for development of a Laser Ion Source Trap (LIST) is the eventual incorporation of such a device at ISOLDE where it could offer an alternative laser/atom interaction region. In this configuration, with the RILIS optimized for ionization of an atomic vapour within the LIST cavity, surface-ionized isobars could be completely suppressed with the use of repeller electrodes before laser ionization occurs. Additionally, users could benefit from the improved beam quality and time structure offered by such a device.

A similar device intended for the IGISOL is probably more accurately named LISS (Laser Ion Source SPIG) since no buffer gas is to be injected in addition to that present after emerging from the gas cell and a trapping mode is not intended for the device. It is merely to be used for efficient extraction of laser ionized products in the form of a low emittance ion beam.

8.2 The Laser System

A requirement for high ionization efficiency is the irradiation of all atoms within the sample. For ionization either within the gas cell or within the SPIG structure the sample can be regarded as being in continuous and fast flowing supply. To minimize duty cycle losses, the importance of a high repetition rate laser system is easily calculable. The duty cycle within the laser interaction region (ν_L) is given by

$$\nu_L = f\tau. \tag{8.2}$$

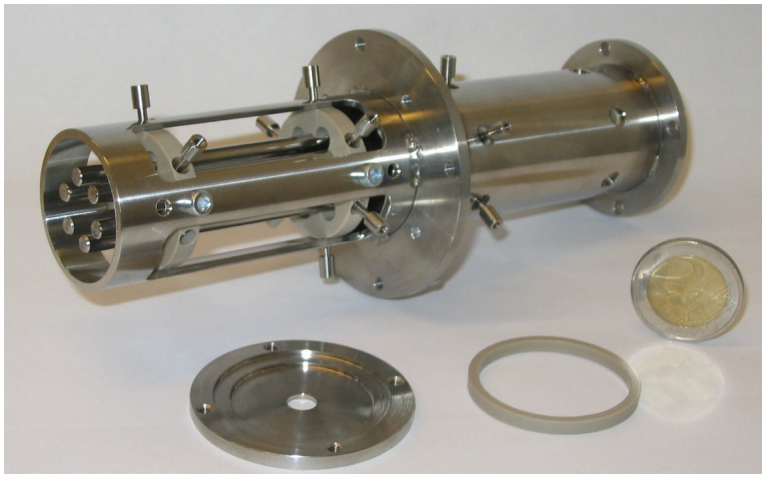

Figure 8.2: The double SPIG test unit for FURIOS.

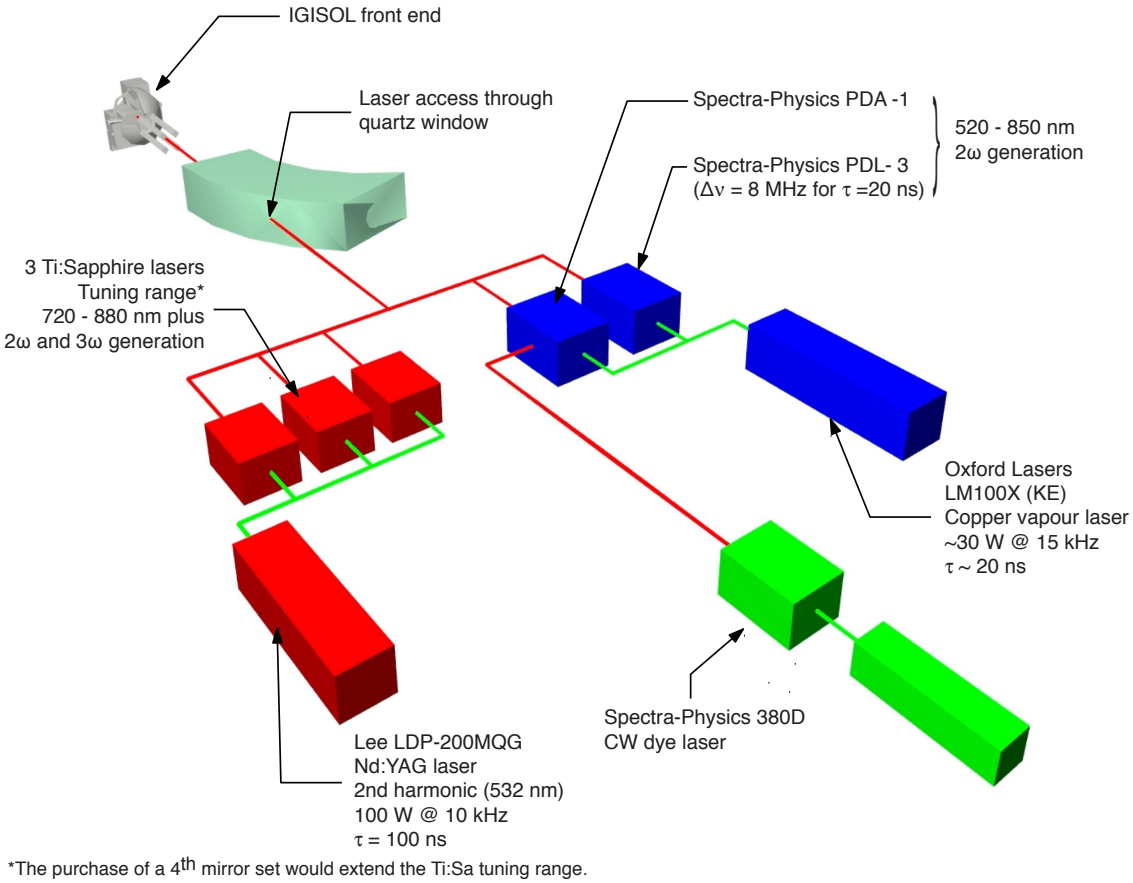

Figure 8.3: The layout of the high repetition rate laser system for FURIOS.

Element	Dimension / Value
Diameter of SPIG injection hole	6 mm
Diameter of SPIG extraction hole	6 mm
Diameter of repeller electrode	47 mm
Thickness of repeller electrode	3 mm
Distance between opposing SPIG Rods ($2r_0$)	10 mm
Length of individual rods (SPIG 1)	78.5 mm
Length of individual rods (SPIG 2)	81.5 mm
Length of complete SPIG structure	165.5 mm
RF frequency, ν_{RF}	2, 3 or 4 MHz
RF amplitude U_{RF}	0-600 Vpp
DC voltages on SPIG rods	0300 V (-ve)
Repeller voltage U_R	0$\rightarrow \pm$300 V
End electrode voltage U_E	0-500 V (-ve)

Table 8.1: Dimensions and operational parameters for the radio-frequency sextupole ion guide (SPIG)

where f is the laser repetition rate and τ is the transit time through the interaction region. For ionization of IGISOL reaction products, duty-cycle losses are zero for a CW laser system. However, the high power density needed to saturate atomic transitions necessitates the use of a pulsed laser system. Such a system should therefore satisfy

$$f \geq 1/\tau. \tag{8.3}$$

For gas-cell laser ionization, where the laser beam trajectory is along the nozzle axis, the laser/atom interactions take place within the region of highest gas-flow velocity. Earlier IGISOL ion-beam time structure measurements discussed by I. Moore in [92] indicate that residence times within the gas cell can be as little as 40 μs since this was the arrival time after the laser pulse for the first laser ionized ions during these tests. For atoms extracted this quickly, a laser repetition rate of 25 kHz is required to satisfy Equation 8.3. An evacuation time of 40 μs is however at the extreme lower limit and in the same study it was shown that more typical value is in the 0.1 - 1 ms range (1 - 10 kHz).

The gas-flow velocity is estimated to be up to 1000 ms^{-1} at the nozzle exit. Taking this as an upper limit for the velocity of atoms within the first SPIG structure (of length $L \approx 80$ mm) the minimum transfer time, τ, through the laser interaction volume is $\tau \geq L/v \geq 80\mu s$, necessitating a laser repetition rate of 12.5 kHz.

The intended workhorse of FURIOS is an all-solid-state laser system, with Nd:YAG pumped Ti:Sapphire lasers. This was chosen in preference to a dye-laser system on account of the success enjoyed by the LARRISA group at Mainz and the ease of use and stability of their laser system [95]. It is also preferable when possible to avoid the need to handle the toxic laser dyes that must be frequently changed in a pulsed dye-laser system.

The fundamental frequency tuning range of the Ti:Sapphire lasers is 720 - 880 nm, and so covers nicely the gap in the dye-laser tuning range from 760 - 790 nm and extends slightly further than the limit of $\sim$ 850 nm. With a Ti:Sa laser system using a single pump laser, it is not possible to use a portion of the high power pump beam as a final, non-resonant stage in the ionization scheme. This is due to the long build-up time within the Ti:Sa crystals before laser emission occurs ($\sim$300 ns). The maximum power output from one of the Ti:Sa lasers is of the order of 4 W. This is not normally sufficient to ensure efficient non-resonant ionization. Widely applicable ionization with a single YAG pumped Ti:Sa laser system would require a great deal of atomic spectroscopy work searching for efficient auto-ionizing states.

A 40 W copper vapour laser was also purchased as a pump laser for the pulsed dye laser and amplifier previously used at JYFL for collinear resonance ionization spectroscopy studies. The possibility exists to trigger the CVL using the Q-switch pulse from the YAG pump laser. By applying a time delay equivalent to the build up time for light emission from the Ti:Sa crystals (300 ns), the high power CVL beam can be used for a non-resonant ionization step.

The pulsed dye amplifier (PDA) is not a laser cavity itself, rather a series of 3 dye cells positioned in series. If 'seeded' with a compatible beam from a CW laser, pulsed amplification of the input beam can result in a pulsed output beam with a narrow linewidth, which is desirable for conducting high resolution resonance ionization spectroscopy at room temperature. The Spectra-Physics

PDA1 has three dye cells and amplifies light from a continuous wave ring dye laser. The ring dye laser system is part of the well established collinear laser fluorescence spectroscopy setup run by Manchester and Birmingham universities. Conveniently, this is housed in an adjacent laser hut almost directly above the IGISOL front end.

The linewidth of the CW laser is typically 1 MHz. After amplification in the PDA, the laser linewidth increases to the Fourier limit of ≈10 MHz for a 15 ns pulse, much lower then the Doppler broadening of atomic lines at room temperature, even for light elements (typically 200 MHz). For greater efficiency at the expense of spectral resolution, a Spectra Physics pulsed dye laser is also available. This is a Hansch [32] type oscillator (a laser cavity with a diffraction grating and transverse pumping) followed by one amplifier cell. The laser linewidth is of the order of 4 GHz.

Alternatively, a Spectron Laser Systems 50 Hz Nd:YAG laser is can be used for pumping the dye-laser system. Combined with the existing RFQ ion-beam cooler-buncher [96] and a sodium charge-exchange cell, this offers the possibility to perform collinear RIS on a fast, bunched atom beam with low duty-cycle losses. This is discussed in depth by K. Flanagan in [97].

In summary, FURIOS is equipped with a uniquely versatile laser system. The tuning range and spectral resolution is unrivaled amongst laser ion sources. The flexibility in terms of laser type and choice of interaction region gives the FURIOS system great potential in terms of not only universal applicability and ionization efficiency, but also resonance ionization spectroscopy and ion-beam purity.

8.3 Optimizing gas flow for FURIOS

Helium jet systems have been in use as a mechanism of extraction of radioactive nuclides since the 1960s and, as more became known about these systems, their use has become refined and more widespread [98]. Of particular note was the discovery of the favorable charge-state distribution brought about by the thermalisation process within the gas, with a large proportion of reaction products settling in a 1^+ charge state [99]. This characteristic formed the basis for the

IGISOL principle, allowing sub-millisecond conversion of reaction products into a radioactive ion beam.

A fuller understanding of the gas-cell system is desirable and has been the goal of various studies since the IGISOL has been in operation. Measurements of gas flow dynamics inside the gas cell were made by K. Peräjärvi et al. [100], concluding that the mean gas velocity at the exit nozzle of the gas cell is equal to the speed of sound in the gas. Little dependence on the actual gas pressure within the cell was observed.

Pre-dating this was an exploratory study into the nature of gas flow and expansion outside the gas cell [101]. This comprised of visual observations made possible through excitation, by electrical discharge, of the gas within the chamber. The faint fluorescence visible from the gas following the excitation is a result of relaxation to the ground-state. For metastable states, this relaxation is of the order of many milliseconds and so, at typical gas cell / vacuum chamber pressure differentials, allows imaging of the gas jet far into the expansion region. The gas-jet photographs obtained allowed identification of the distinct shock-wave structures described by the fluid dynamics of a freely expanding gas [101]. Some observations were made with gas flow obstructions, in the form of circular disks with a central aperture, placed down-stream of the nozzle. This was intended to simulate the real-world IGISOL situation where the expanding gas is incident upon a skimmer electrode within a few centimeters of the exit nozzle. The effect on the gas flow was tested for various aperture diameters. The study concluded that, for large apertures (with a diameter greater than the visible gas-jet diameter), the gas flow remains largely unperturbed. However as the aperture diameter is reduced to less than the visible gas-jet width, a shock-wave is observed and the gas flow after the aperture becomes more diffuse and expansive. It appears that a transition is made from a low emittance supersonic jet to a subsonic and rapidly expanding plume.

This work was conducted whilst the IGISOL was considered only as an ‘ion guide’ and within the extraction region, ion transmission is governed not by the gas flow, but rather by the electrostatic extraction potential. The gas flow changes caused by the presence of a skimmer electrode were not a major source of concern.

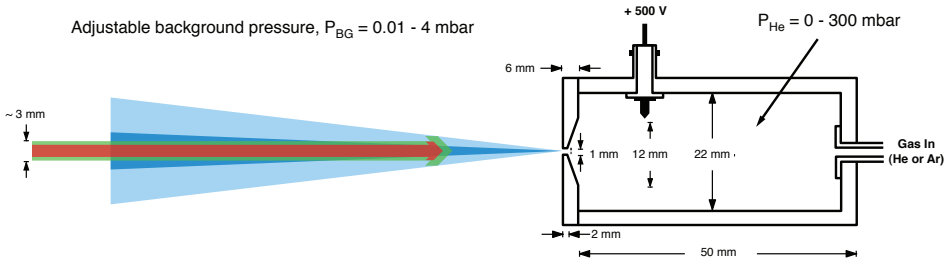

Figure 8.4: Schematic of the test gas cell. The proposed incident laser beam trajectory is shown with the expected beam diameter to illustrate the necessity for a narrow gas jet.

The development of the laser ion source and the use of the gas cell as an 'atom guide' has renewed interest in the gas flow dynamics where it is the atomic flow that is of primary importance. To this end, a further investigation has been conducted using a similar experimental setup to that described in [101].

A number of visual observations of the gas jet have been made for various gas flow rates and vacuum conditions. In addition, the transport by gas flow of isotopes recoiling from a ^{223}Ra source was studied. This served the purpose of confirming that intensity of the glow from the de-exciting gas was indeed representative of the gas flux.

8.3.1 Observation of the excited gas jet

Figure 8.4 is a schematic of the gas-cell set-up for gas-jet observations. For illustrative purposes, the expected laser beam trajectory and approximate dimensions for laser ionization at IGISOL are indicated in the figure. Helium or argon gas was injected into the rear of the gas cell and the pressure was regulated using a needle valve. A Pirani gauge attached close to the gas cell was used for the inlet gas-pressure measurement. The vacuum chamber was pumped with two Roots blowers, each with a specified pumping speed of 4000 m^3/h. A Penning gauge and a second Pirani gauge, positioned on the top flange of the vacuum chamber, approximately 15 cm from the gas-cell nozzle, allowed monitoring of the background pressure within the extraction region. In practice, the minimum pressure

achieved within this region (without gas injection) was of the order of 10^{-3} mbar. An overhaul of the vacuum chamber; the renewal of the seals for each flange and a reduction of the pumping volume should be performed if lower pressures are to be achieved. The setup was visible from one side of the vacuum chamber through a Plexiglas flange.

The single electrode was connected to a 50 mA current-limited DC power supply. To initiate the discharge within the gas cell, a helium gas pressure of over 100 mbar and a voltage in excess of 300 V was required. With an increase to 500 V, the gas emerging from the nozzle exhibited a glow easily visible with the naked eye.

The gas jet could be photographed using a digital camera with a high ISO setting ($\geq$800) and an exposure time preferably in excess of 15 s. Two cameras were used throughout this study; a Minolta F200 (ISO 800 and 20 s exposure) and a Sony DSC V-1 (ISO 1600 and 15 s exposure). For stability, pictures were taken with the camera mounted on a fixed support, 30 cm from the gas cell using the 10 second self-timer facility, which allowed for dissipation of vibrations caused by contact with the apparatus.

The following variables were tested during the gas-jet study:

- Nozzle design
- Gas-cell pressure, P_{He}
- Background pressure, P_{BG}

Figure 8.3.1 shows the evolution of the gas jet with increasing gas-cell pressure for the two nozzle types tested. These nozzles were chosen for convenience due to their immediate availability at the onset of the investigation. Of the existing nozzle designs, these two differ the most greatly from each other in terms of their cross section and so it was assumed that a dependence on nozzle shape would become most apparent through their comparison. The first nozzle has a small conical entry and exit aperture, with a maximum radius of 2 mm tapering down to the central exit hole of radius 0.8 mm. The second nozzle has the same exit hole dimensions but a flat exit aperture and a larger conical inner aperture with a maximum radius of 6 mm. For testing these nozzles, a helium gas pressure

within the gas cell of ≤ 50 mbar was used and the background pressure in the chamber was maintained close to 0.05 mbar. Whilst these pressure parameters differ somewhat from the standard IGISOL operating conditions, they resulted in the production of a large and clearly visible glowing gas cloud, facilitating the comparison of nozzle types. Photographs of the gas jets are shown in Figure 8.3.1 and little difference can be seen in the gas jets produced from each nozzle.

Whilst this is by no means a comprehensive assessment of IGISOL nozzle options, the overriding importance of the gas pressures; P_{He} and P_{BG} in determining the gas-jet profile is clearly demonstrated and so formed the basis of further study. The gas jets pictured in Figure 8.3.1 are very expansive and do not have favorable dimensions for the application of resonance ionization using single pass lasers along the axis of the gas-cell nozzle. Figure 8.6 shows the outcome of a systematic test of various P_{He}:P_{BG} combinations. With a helium pressure of 140 mbar and a background pressure of 3 mbar, a gas jet with greatly favorable dimensions is produced. This jet is well collimated and maintains a width comparable to the expected laser beam diameter over a distance greater than the proposed laser/atom interaction length.

Within the relevant helium gas-pressure range (80 - 300 mbar), a relative lack of dependence on the He pressure was observed and emittance of the gas jet is apparently determined by the background pressure. It appears that at a certain P_{BG} value, a transition from a gas cloud with almost isotropic expansion, to a highly directional gas jet occurs.

Within the scope of the earlier gas-jet work carried out by K. Peräjärvi [100], the gas flow from through the nozzle is assumed to be *viscous* since, for the gas pressures involved, the mean free path of the atoms is much smaller than the gas-cell dimensions.

For viscous flow, the maximum gas velocity is equal to the speed of sound in the gas and is reached when the following critical pressure condition is satisfied:

$$\frac{P_{in}}{P_{out}} \geq \left(\frac{\gamma+1}{2}\right)^{\frac{\gamma}{\gamma-1}} \tag{8.4}$$

where $\gamma = C_p/C_v$, the ratio of specific heats of the buffer gas at constant pressure and constant volume. P_{in} is the gas pressure in the high pressure region

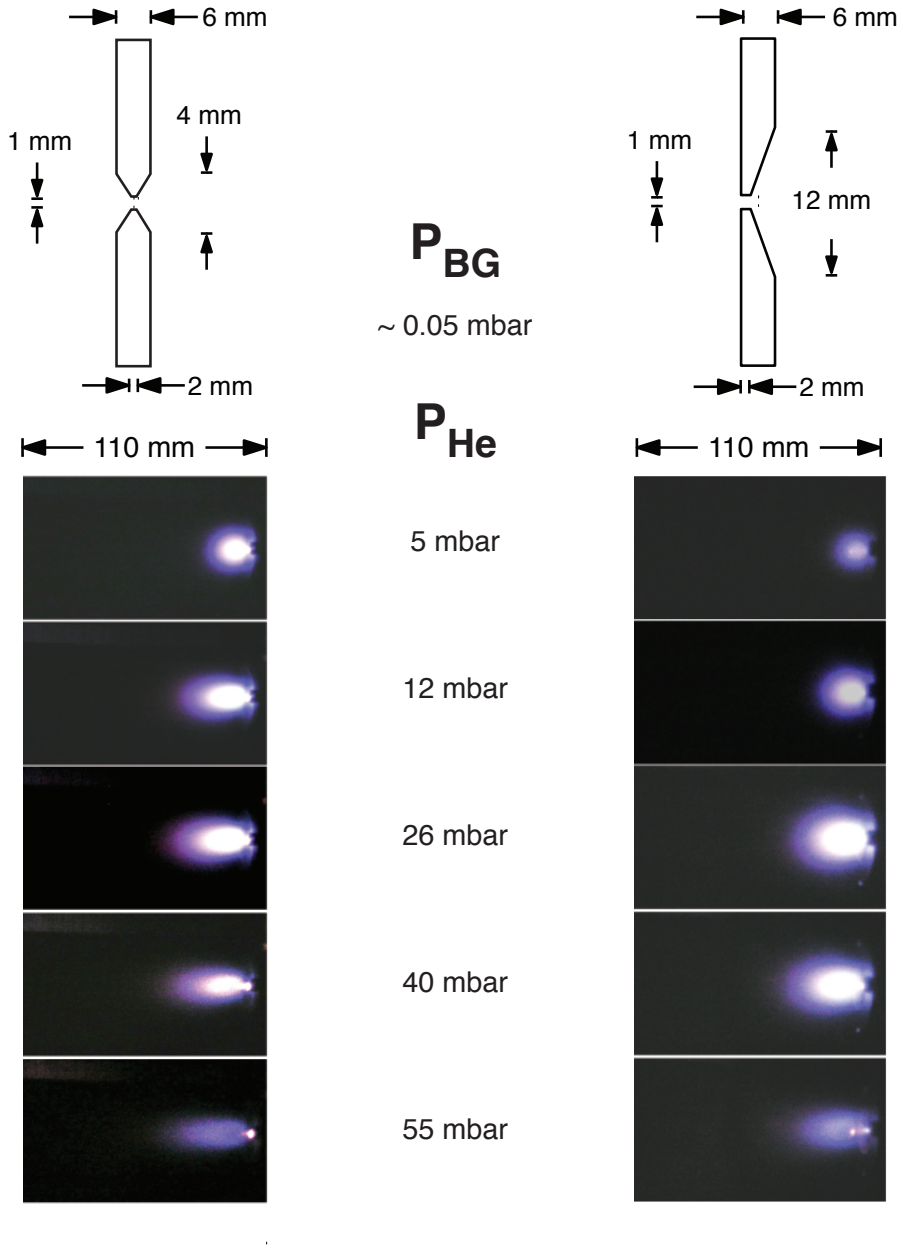

Figure 8.5: Initial gas-jet observations for comparison of two IGISOL nozzle types.

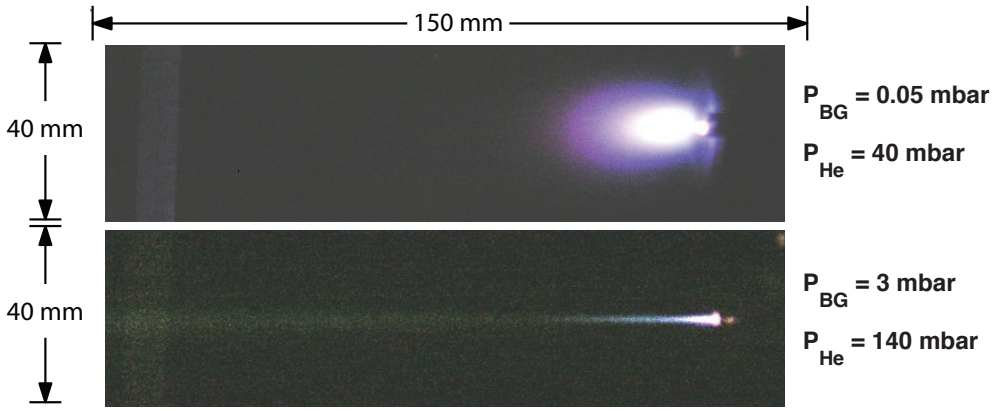

Figure 8.6: Achieving a narrow gas jet with restricted pumping of the vacuum chamber (high background pressure)

and P_{out} is the pressure within the gas-expansion volume. For the purposes of this work the critical-pressure condition becomes:

$$\frac{P_{He}}{P_{BG}} \geq 1.4. \tag{8.5}$$

For all of the measurements made during this study, this condition is met. The gas velocity is therefore equal to the speed of sound and is independent of the gas-cell pressure. It follows then that the behavior of the gas outside the nozzle is now determined by the environment into which it is expanding.

Generally, objects moving faster than approximately 0.8 times the speed of sound (Ma = 0.8) produce shock-waves propagating with an angle θ to the velocity of the object with Ma= $1/\arctan(\theta)$. For an expanding gas jet, these shock-waves alter the density distribution within the gas jet and, under steady state conditions, discrete loci of high and low gas density form.

Most of the literature dealing with the free expansion of gas from a sonic nozzle deals with high pressure gas entering a region of atmospheric pressure. Figure 8.7, taken from Reference [102] shows the gas-jet structure expected under certain pressure conditions. The left-hand side of the figure (labeled *a*) shows the jet structure obtained for a pressure ratio $P_{in}/P_{out} \ll 100$. The gas jet has a multiple-shock cell structure with a long, narrow tail of successive compression

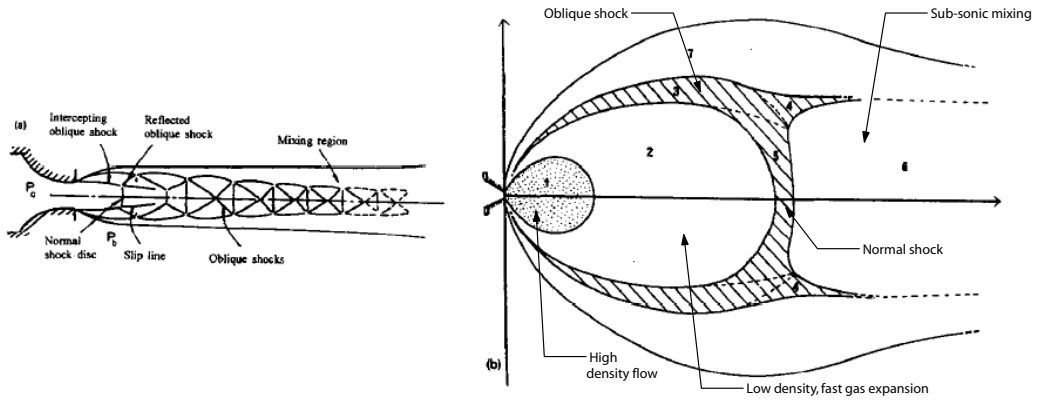

Figure 8.7: The shock wave structures associated with sonic flow through a nozzle.

and expansion waves. The right-hand illustration, (labeled *b*), shows the behavior observed with with a higher pressure ratio, $P_{in}/P_{out} > 100$. The first shock cell dominates the jet structure.

A multiple shock-wave structure somewhere between these two extremes was observed in the gas-jet photographs taken with a helium pressure of 140 mbar. Figure 8.8 shows the change in the gas density structure for increasing values of P_{BG}. A shock wave known as the *Mach disk* surrounds the first region of fast, low density gas expansion and is immediately upstream of a compression wave where the gas density is considerably greater. These compression waves are clearly visible after digital manipulation of the photographs to highlight the areas of increased intensity.

In Reference [102], the Mach disk location, x_M is related to the pressure ratio and also the nozzle diameter, D by:

$$x_M = 0.67(P_{in}/P_{out})^{1/2} \cdot D. \tag{8.6}$$

The predicted Mach disc location has been calculated for the conditions shown in Figure 8.8 and are tabulated alongside the experimentally observed values in Table 8.3.1.

The observation of the shock-wave structure within the gas jet is evidence that sonic flow is occurring. The experimentally observed Mach disk positions, x_M^{expt}, are in reasonably good agreement with the theoretically predicted values. This

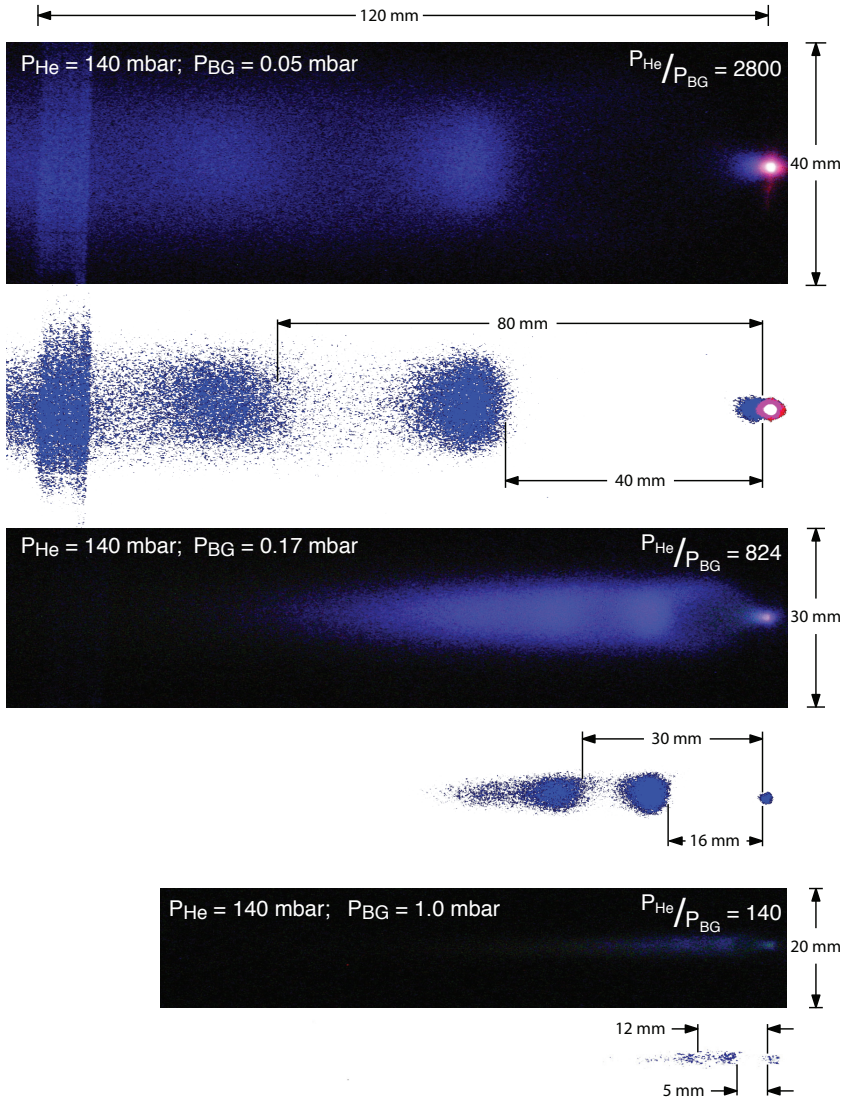

Figure 8.8: Contraction of the first and second shock disks with increasing background pressure.

P_{He}/P_{BG}	x_M^{expt} mm	x_M^{theory} mm
2800	40	36
824	16	19
140	5	7.9

Table 8.2: A comparison of the observed Mach disk position with those predicted by Equation 8.4.

confirms the correct identification of the features within the shock-wave structure, verifying that the brighter areas within the gas jet are indeed areas of greater gas density.

With increasing background pressure, the reduction in x_M is accompanied by a considerable reduction in the jet width. Figure 8.9 shows a further series of measurements for which the photographs were studied using the Matlab image manipulation package, capable of displaying a contour plot of the image brightness. At the bottom of the figure, intensity plots of gas-jet cross sections at a distance of 20 mm from the nozzle are displayed. Assuming for each photograph considered individually, the gas-jet brightness is proportional to the gas density, the plots imply that a factor of almost 100 increase in background pressure results in an order of magnitude reduction in jet width.

8.3.2 Alpha Recoil Measurements

There was some concern that the effect of the increased background pressure was to merely accelerate the collisional de-excitation process for the excited gas, and that the reduction in the observable jet width with increasing background pressure is actually somewhat misrepresentative of the behavior of the unexcited gas. An attempt was made to investigate this by studying the transport of particles within the gas. For this, an α-recoil source of ^{223}Ra was placed within the gas cell on the tip of a needle. ^{223}Ra is a commonly used source for off-line IGISOL testing due to the suitable lifetimes of the daughter products ^{219}Rn (3.96 s) and ^{215}Po (1.8 ms). The source is collected on a needle tip as the granddaughter of the decay of a 200 kBq ^{227}Ac (21.8 yrs) source.

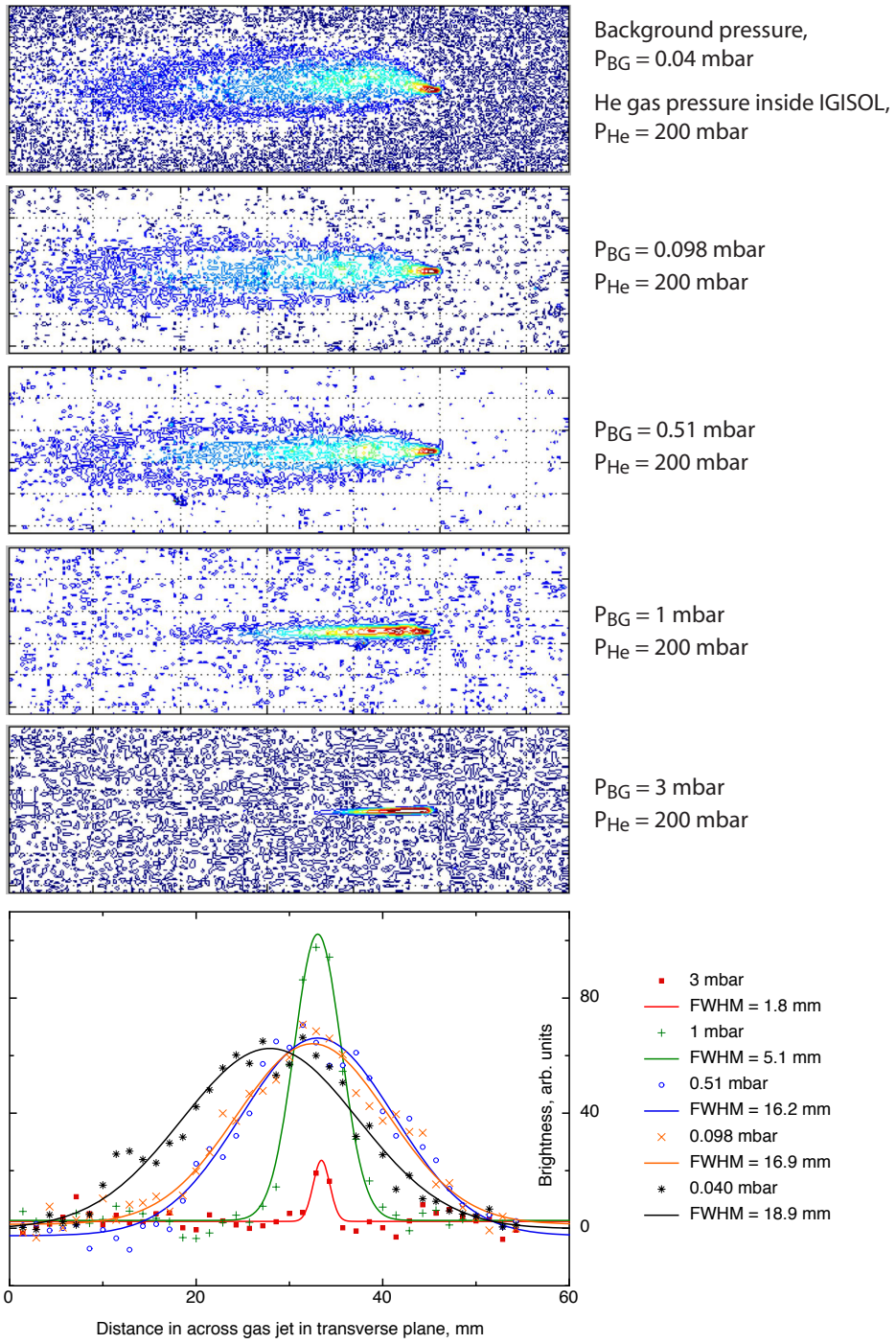

Figure 8.9: MATLAB image analysis of excited He jet and jet profiles 20 mm from IGISOL nozzle.

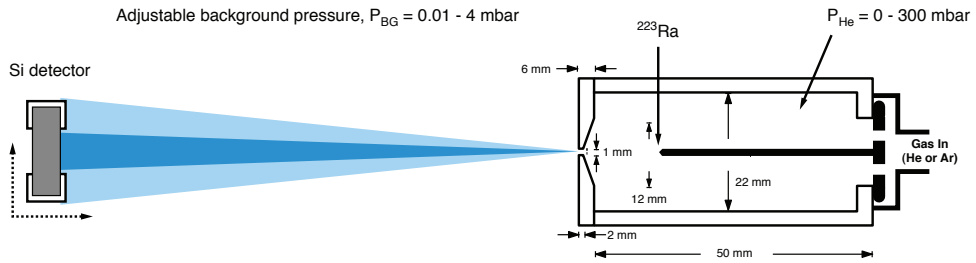

Figure 8.10: Schematic of the test gas cell for use with a ^{223}Ra α-recoil source.

The needle tip was placed within a modified gas cell as shown in Figure 8.10 and mounted on a customized O-ring adaptor at the gas inlet connection point. The Ra source covered only a 5 mm long section of the needle tip and was positioned approximately 10 mm from the exit nozzle. For these measurements, the objective was not to improve the accuracy of the measurements obtained by imaging the gas jet, but rather to verify the key observations of this study and establish some confidence in the ability to rely on the fluorescence variations in the photographs as a true representation of the gas density distribution. Additionally, for high background pressures, it is difficult to observe the gas jet more than a few centimeters into the expansion region. Measuring particle transport therefore facilitates gas-jet measurements at a distance covering the entire intended laser interaction region.

The ^{219}Rn ions recoiling into the gas cell from the alpha decay of the source were transported out of the cell and carried into the vacuum chamber within the gas jet. A small silicon detector (with a 15 mm diameter active area) was placed on a moveable mount within the vacuum chamber and could be positioned at various locations within the previously observed gas flow region. The probability of particle detection at a given location within the gas is proportional to the gas-jet density at this point.

The results of this study, shown in Figure 8.11 provide convincing evidence that the apparent narrowing of the gas jet with increasing background pressure is genuine:

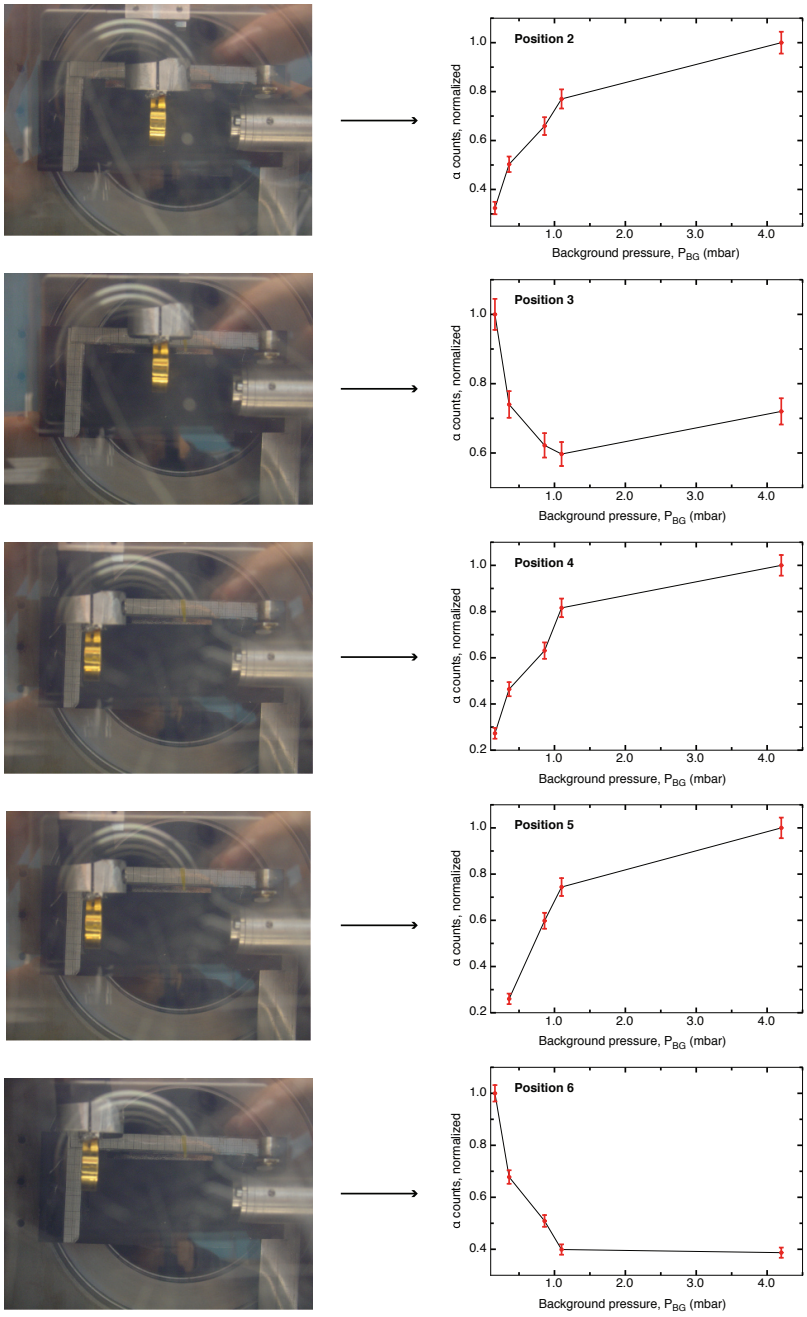

Figure 8.11: Alpha counts as a function of background pressure for various detector positions.

Position 2

Even at a short distance from the nozzle, an increase in background pressure greatly improves the transport efficiency of particles close to the axis of the gas-cell nozzle.

Position 3

With the detector placed ≈15 mm from the nozzle axis, where a wide gas jet is required for transport of the particles to the detector, the ion count rate is greatest for a low background pressure.

Positions 4, 5 and 6

The type of behaviour observed for positions **2** and **3** is more evident at a greater distance from the exit nozzle. A consistent feature throughout these measurements is the apparent saturation of the ion count rate with increasing background pressure. For all plots, little improvement in the particle transport characteristics is observed with an increase in P_{BG} from 1 to 4 mbar. Three proposed explanations for this are discussed:

i For $P_{BG} > 1$ mbar, the jet width is less than the diameter of the detector surface. For detector positions **3** and **6** the gas jet completely misses the detector surface if $P_{BG} > 1$ mbar whilst, for the same pressure but with the detector in position **2**,**4** or **5**, the jet is entirely within the detector surface.

ii For $P_{BG} > 1$ mbar, the depth of penetration of the gas jet into the vacuum chamber is reduced. The benefit of a reduced jet width is offset by the reduction in jet length. This seems unlikely since the same saturation point of $P_{BG} \approx 1$mbar is observed at two distances across the vacuum chamber from the nozzle (positions **2** and **5**).

iii For $P_{BG} > 1$ mbar, a transition of the gas flow dynamics from turbulent to laminar is complete and so no further significant change in the gas flow characteristics occurs for small pressure increases. This explanation could hold provided that the gas flow is analogous to viscous flow through a pipe.

Under this condition, the velocity dependent Reynold's number, R_e, is used to classify the flow as being either *turbulent* or *laminar*:

$$R_e = \frac{\rho}{\eta} d v_f \tag{8.7}$$

where ρ is the gas density, η is the viscosity and v_f is the gas velocity. Turbulent flow occurs when $R_e \geq 2100$ and, for $R_e \geq 110$ the flow is laminar. The values of v_f and ρ for the gas jet are not known but the possibility of a transition to laminar flow should be considered.

It is likely that the simple explanation offered in point **i** above is sufficient to account for the observed behaviour but the flow dynamics discussed in point **iii** are of interest and will be discussed later in the context of the revised SPIG design.

Figure 8.12 shows the results of a further measurement of the alpha count rates averaged over a 2000 s integration time with the detector positioned 12 cm downstream of the nozzle. The detector position was chosen to provide a set of measurements of the particle transport outside of the observable range of the gas jet. The location of the detector is indicated on the previously acquired photographs of gas jets observed under the same pressure conditions.

8.3.3 The gas-jet enclosure

For the application of FURIOS inside the RF sextupole, the gas-jet observations show that a high pressure region outside the nozzle (1 mbar) is required across the entire laser interaction region. In normal operating conditions, the IGISOL vacuum chamber close to the nozzle is held at a lower pressure than this, typically 10^{-4} mbar. This is to enable a good vacuum to be maintained within the subsequent mass separator and beamline sections.

With the use of a gas enclosure surrounding the RF sextupole device, it should be possible to satisfy the pressure requirements for the narrow gas jet, without any need to alter the same vacuum pumping configuration or compromise the background pressure within the vacuum chamber. The enclosure provides a means of restricting the gas extraction immediately around the laser interaction region.

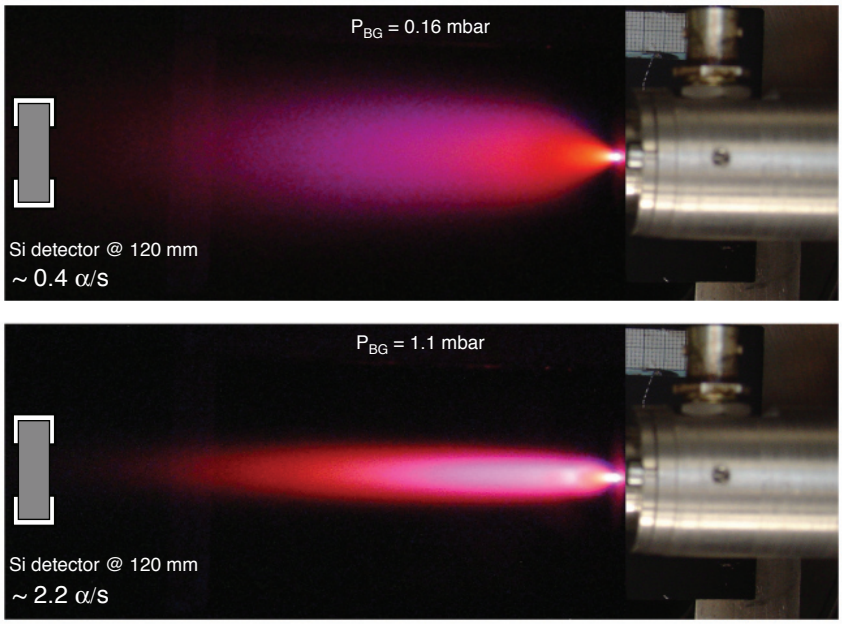

Figure 8.12: Alpha count rates for high and low background pressures with 200 mbar He.

Figure 8.13 shows the influence of a cylindrical Perspex enclosure placed at the nozzle exit. In this configuration, the gas extraction is possible only through the 10 mm diameter hole at the enclosure exit, 150 mm downstream from the gas-cell nozzle. For both gas jets shown the background pressure in the vacuum chamber was 0.01 mbar.

Figures 8.14, and 8.15 show gas flow simulations conducted by A. Popov as confirmation of this study [103]. The simulations show the clear benefit of the use of a gas-jet enclosure to provide a collimated gas jet for efficient laser/atom interaction.

The final design for the SPIG is shown in Figure 8.16. The structure comprises of two RF sextupoles separated by an adjustable iris. The first SPIG surrounds the laser/atom interaction region and is enclosed for restricted gas extraction and the second SPIG is left open for ion-beam manipulation within a lower pressure environment.

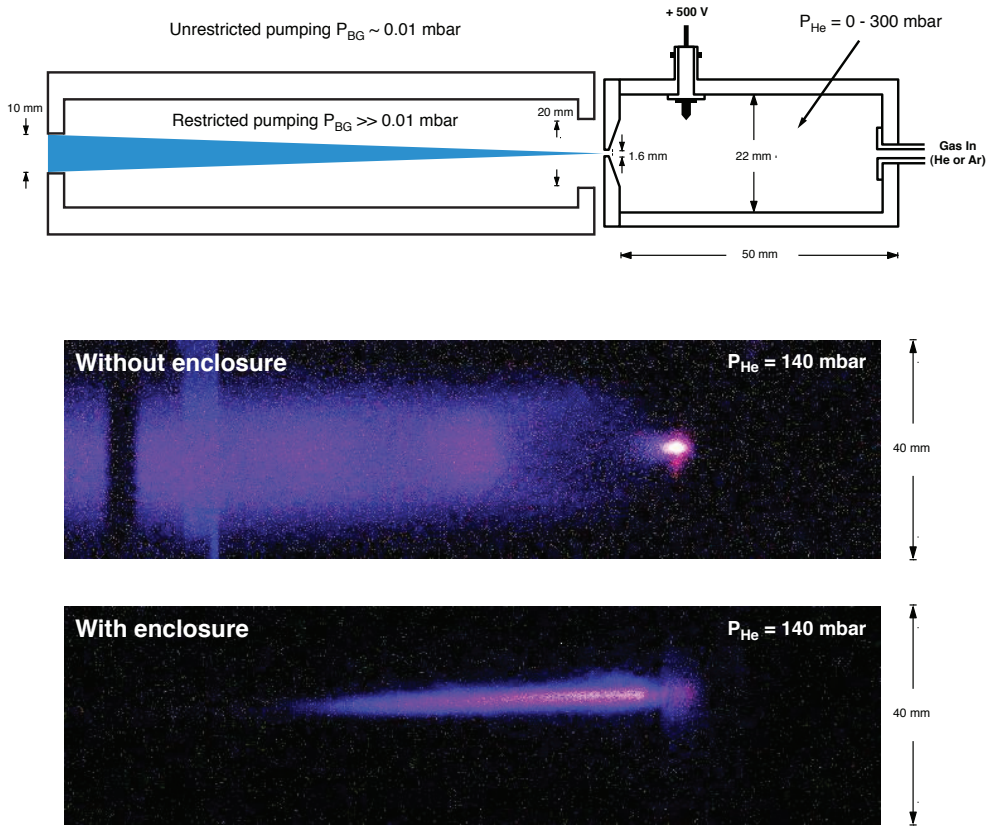

Figure 8.13: Obtaining a narrow gas jet through the use of an enclosure to locally inhibit the gas extraction outside the gas cell.

8.4 Offline test of RIS inside a RF-sextupole ion guide.

A RIS study of stable bismuth was considered an ideal candidate for the first FURIOS test inside the SPIG volume due to a number of factors:

- Easy sample preparation.
- Low chemical reactivity.
- Simple and well characterized ionization scheme.

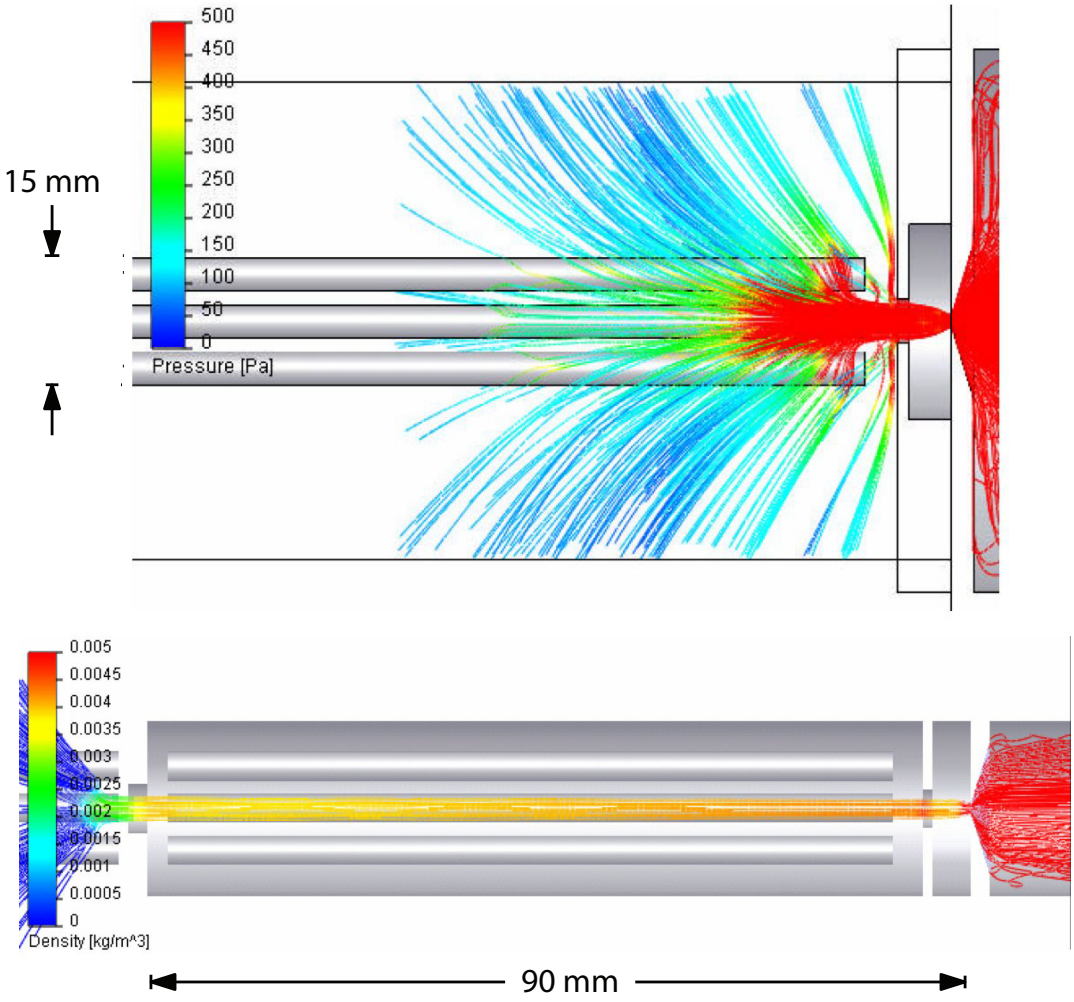

Figure 8.14: FlowWorks2004 simulations: Gas particle paths in open and closed SPIG structures. The ion guide and exit nozzle are located on the right.

- Previous experience of Bi gas-cell RIS at IGISOL.

The objective of the test was to make a direct comparison of RIS of bismuth inside the gas cell with RIS outside the gas cell within the first SPIG structure. The respective time structures for the ion beam, the spectral resolution and the relative ionization efficiency were of interest.

An atomic vapour of bismuth was created within the gas cell by resistively heating in-situ a bow-tie shaped bismuth-coated tantalum foil (2.5 mg/cm^2 Bi on

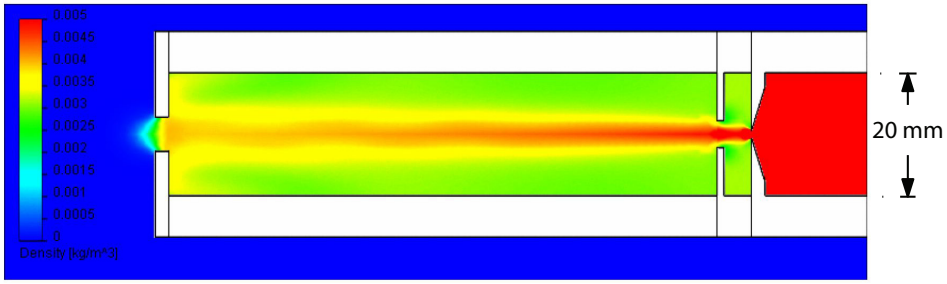

Figure 8.15: FlowWorks2004 simulation: Gas density distribution inside the enclosed SPIG structure.

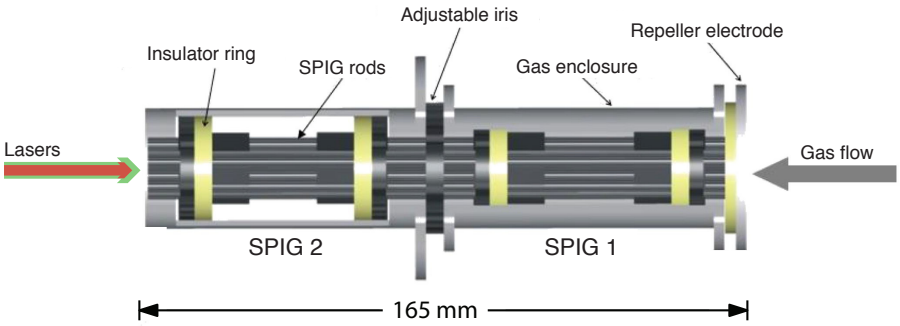

Figure 8.16: Final SPIG design with variable restricted gas extraction in the ionization region (SPIG 1).

7.4 mg/cm^2 Ta). For experimental simplicity in terms of attaining the necessary laser power density, signal detection and ion beam time structure analysis, a low repetition rate (50 Hz) laser system was used. This consisted of a 50 Hz Spectron Laser Systems SL-801 Nd:YAG laser providing output beams from the second and third-harmonics of the fundamental emission wavelength (532 nm and 355 nm). The ionization scheme, shown in Figure 8.18 is the same simple two-step scheme used in the previous gas-cell RIS work for bismuth carried out by Moore et al. [92]. This scheme employs the same resonant transition used for the RILIS spectroscopy study of bismuth presented in chapter 7: 306.770 nm excitation from the ground-state $^4S_{3/2}$ level to the $^4P_{1/2}$ level.

Laser light for this first transition in the ionization scheme was generated by amplification and frequency-doubling of the continuous wave (CW) output from

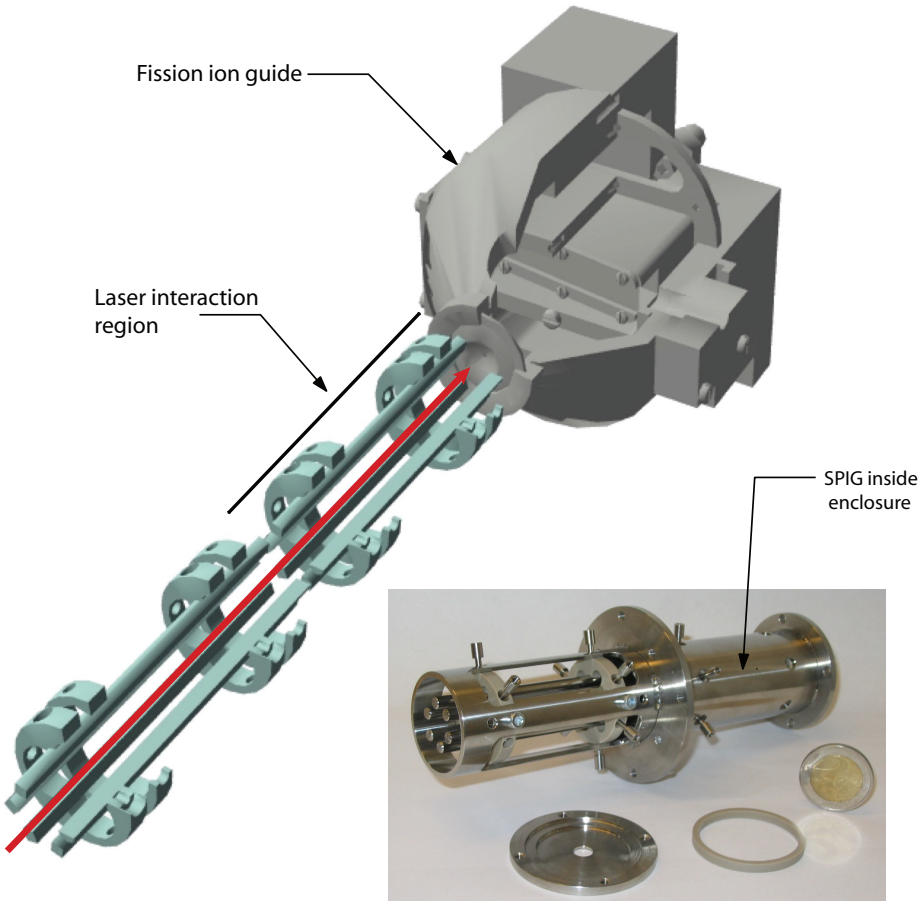

Figure 8.17: Dual SPIG design with inset photograph of the finished SPIG with a steel enclosure surrounding the first SPIG section.

a Spectra-Physics 380D ring dye laser using Rhodamine 6G dye pumped by a Coherent Verdi CW Nd:YAG laser. The setup of the ring dye laser is described in References [93] and [97]. Pulsed amplification was performed by sending the beam through the three dye cells of a Spectra-Physics PDA1 pulsed dye amplifier (PDA). DCM dye was used and pumped with the second-harmonic (532 nm) output from the aforementioned Spectron Laser Systems 50 Hz Nd:YAG laser. The optimal YAG pump power distribution was determined to be a 15:15:70 power configuration for the respective dye cells (oscillator:amplifier 1:amplifier 2). A BBO crystal was used for frequency-doubling in a single pass configuration

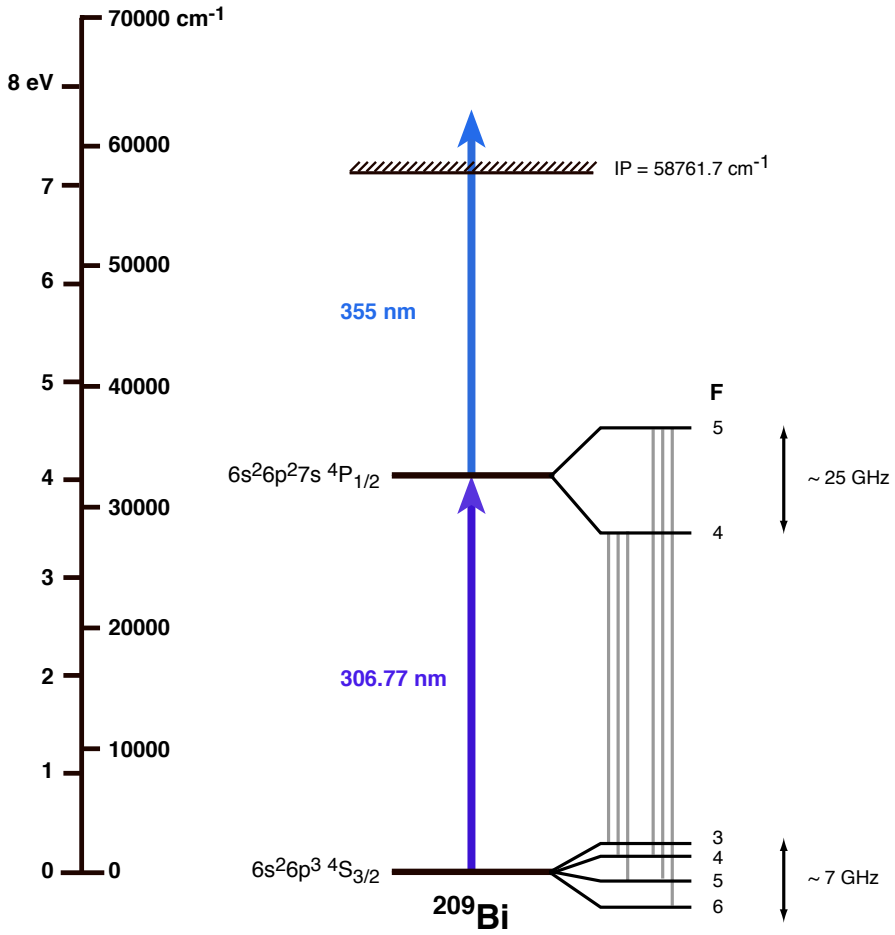

Figure 8.18: The two-step ionization scheme used for the FURIOS RIS tests.

similar to that shown in illustration **ii** of Figure 5.4. From the $^4P_{1/2}$ level, the ionization continuum is attainable by absorption of 355 nm photons, provided by the third-harmonic Nd:YAG output. For this beam a delay line of approximately 3 m was required in order to ensure temporal overlap of the pulses at the laser/atom interaction region.

Initial tests of the system were performed with both laser beams focussed inside the gas cell through the rear window. Telescopes were used to reduce the beam divergence, enabling transport of the laser beams to the IGISOL cave using UV bending mirrors. For the final focussing inside the gas cell, a 3 m focal length lens was used. Microchannel plates positioned in the switchyard after the dipole mass separator were used to monitor the beam current at mass 209. The ion signal could be monitored on an oscilloscope triggered from the Nd:YAG Q-switch pulse. The presence of laser ionized ^{209}Bi could be confirmed by blocking the laser beam for the first-step transition which resulted in an ion count rate of zero. For the study of the ion beam time structure, data acquisition was performed using up to three adjustable coincidence gates (scalars). The coincidence gates were set relative to the Nd:YAG Q-switch pulse.

Bismuth ion spectra were obtained by scanning the 380D dye laser across the full hyperfine structure ($\approx$ 25 GHz). For each scan an additional scalar was reserved for recording the spectrum from an iodine absorption cell. This technique produces convenient reference spectra for each laser scan. Examples of these iodine spectra are displayed on the plots in Figures 8.21, 8.22 and 8.23. A frequency drift of the laser scanning range can be monitored by identification of the corresponding I_2 absorption spectrum. Laser beam access to the IGISOL front end is possible either from the exit nozzle side, via a quartz window in the mass separator, or from the rear of the gas cell, through the window opposite the exit nozzle. Due to time constraints and activity levels close to the IGISOL front end, all tests were conducted with the laser beam for the first-step entering the interaction region through the gas-cell window. A simplified illustration of the experimental setup is shown in Figure 8.19.

The He gas pressure was fixed during the tests at 42 mbar, chosen to allow sufficient heating of the foil for the duration of the measurements despite being

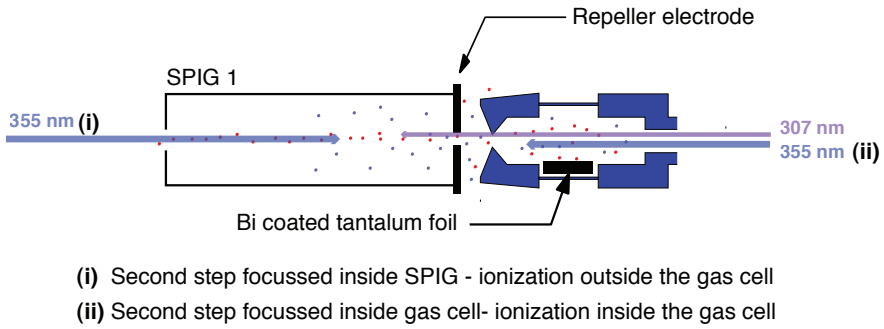

Figure 8.19: Laser access options and ion guide setup for bismuth ionization either inside the SPIG or within the gas cell.

significantly lower than the expected optimal gas pressure for on-line IGISOL operation.

Figure 8.20 shows the typical measurement cycle and ion arrival time structure. The measurement cycle was triggered from the flashlamp firing time for the Nd:YAG laser. The Q-switch pulse follows 120 μs later. Ion arrival times are indicated for a series of repeller voltages to illustrate the additional ion guidance action of the repeller voltage and its use in determining the creation point of the ions. With a negative repeller voltage (and therefore no suppression of ions from the gas cell), the arrival ion time is later than for a positive repeller voltage. For a positive repeller voltage (suppression of gas-cell ions) the ions arrive sooner with increasing repeller voltage. This is attributed to an increase in the acceleration potential and so can only be seen if the ions are created down stream of both the nozzle and the repeller (inside the SPIG).

8.4.1 Results

The starting point for this work was a test of ionization within the gas cell, enabling an initial comparison with the earlier gas-cell RIS work to be made. Figure 8.21 shows the Bi ion spectrum for ions created inside the gas cell. The total ion spectrum is shown alongside the spectrum for ions arriving within a 1000 μs coincidence gate beginning 120 μs after the flashlamp trigger pulse. Two broad

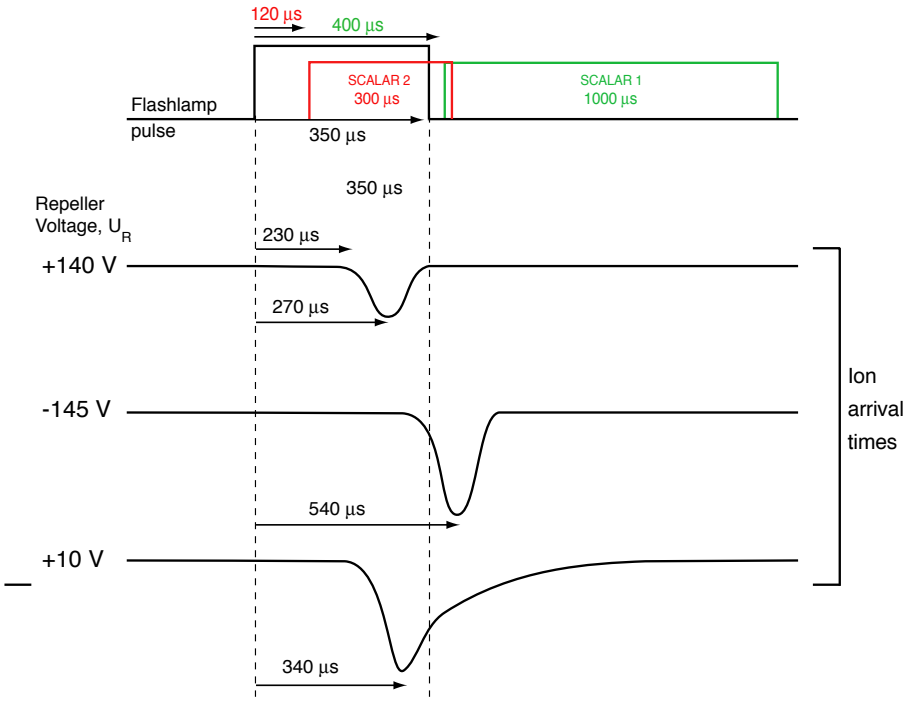

Figure 8.20: Laser pulse and data acquisition timing structure. Examples of the scalar window durations and raw channel plate ion signal time structures are given.

resonance peaks are seen, each of which encompass three unresolved hyperfine components. Clearly, a large fraction of the ions are released outside the time window of the coincidence gate hence are created further inside the gas cell and so take more time to reach the nozzle.

Figure 8.22 shows a Bi spectrum taken using two coincidence gates, one gate of 1 ms duration starting 400 μs after the trigger pulse and a narrower, 300 μs preceding this, positioned only 120 μs after the trigger. The laser beam for the second step was sent through the nozzle and into the gas cell from the mass separator side. The low power first step beam was focussed inside the gas cell so that only a small fraction of the diverging beam was capable of entering the SPIG section through the gas-cell nozzle. The spectra show that approximately an equal number of ions are detected within the two coincidence gate time window, accounting for more than two thirds of the total ion signal. The first spectrum

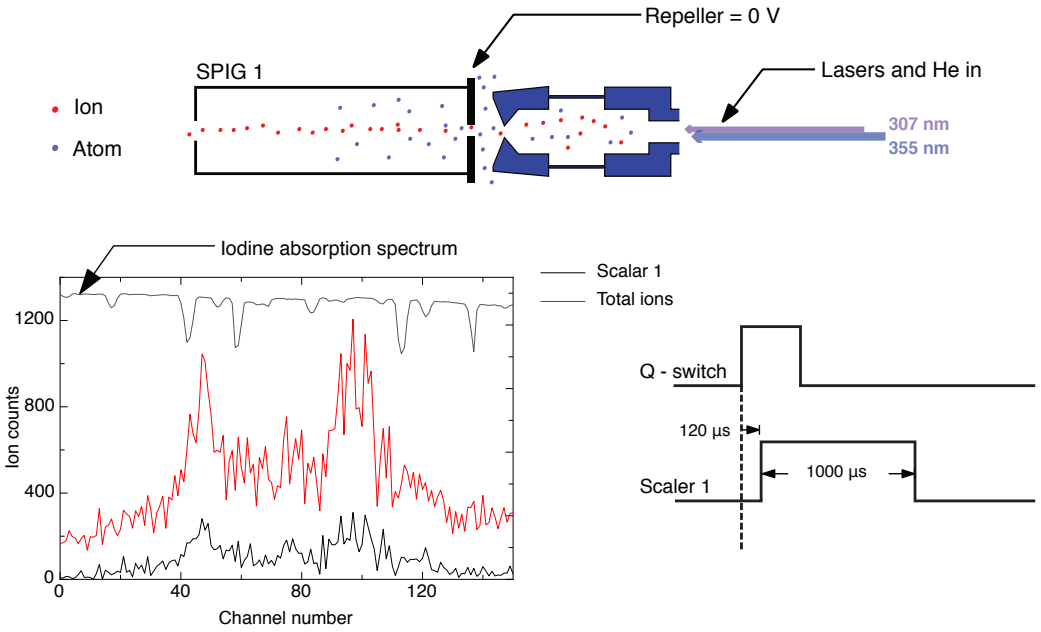

Figure 8.21: Bismuth ion spectrum: ionization inside the gas cell.

was acquired with maximum attainable power at 307 nm ($\approx$ 50 μJ per pulse). With this beam attenuated to below saturation an improvement in resolution was achieved at the expense of ionization efficiency. It was still not possible to resolve the structure within the HFS triplets [2] but operating at a laser power below saturation simplifies the analysis of the ion signal by ensuring the ionization process is reliant upon the presence of the second laser beam. The lower spectrum shows the ion signal with a reversed repeller voltage polarity (+10 V). The absence of an ion signal confirms that the gas cell is indeed the source of the ions in the previous two spectra whilst also illustrating the ease with which these gas-cell ions are suppressed.

Ionization within the SPIG volume was tested after adjusting the focus for the first-step laser beam. By moving the final lens and focussing the beam in the gas-cell nozzle, the gradual beam divergence commences as it enters the SPIG structure. In this configuration, resonant laser ionization can occur either within

[2] In subsequent work with a high repetition rate (15 kHz) laser system and a narrower linewidth (lower power density and a longer pulse length), the individual hyperfine components were resolved for ions created in the gas cell [47]

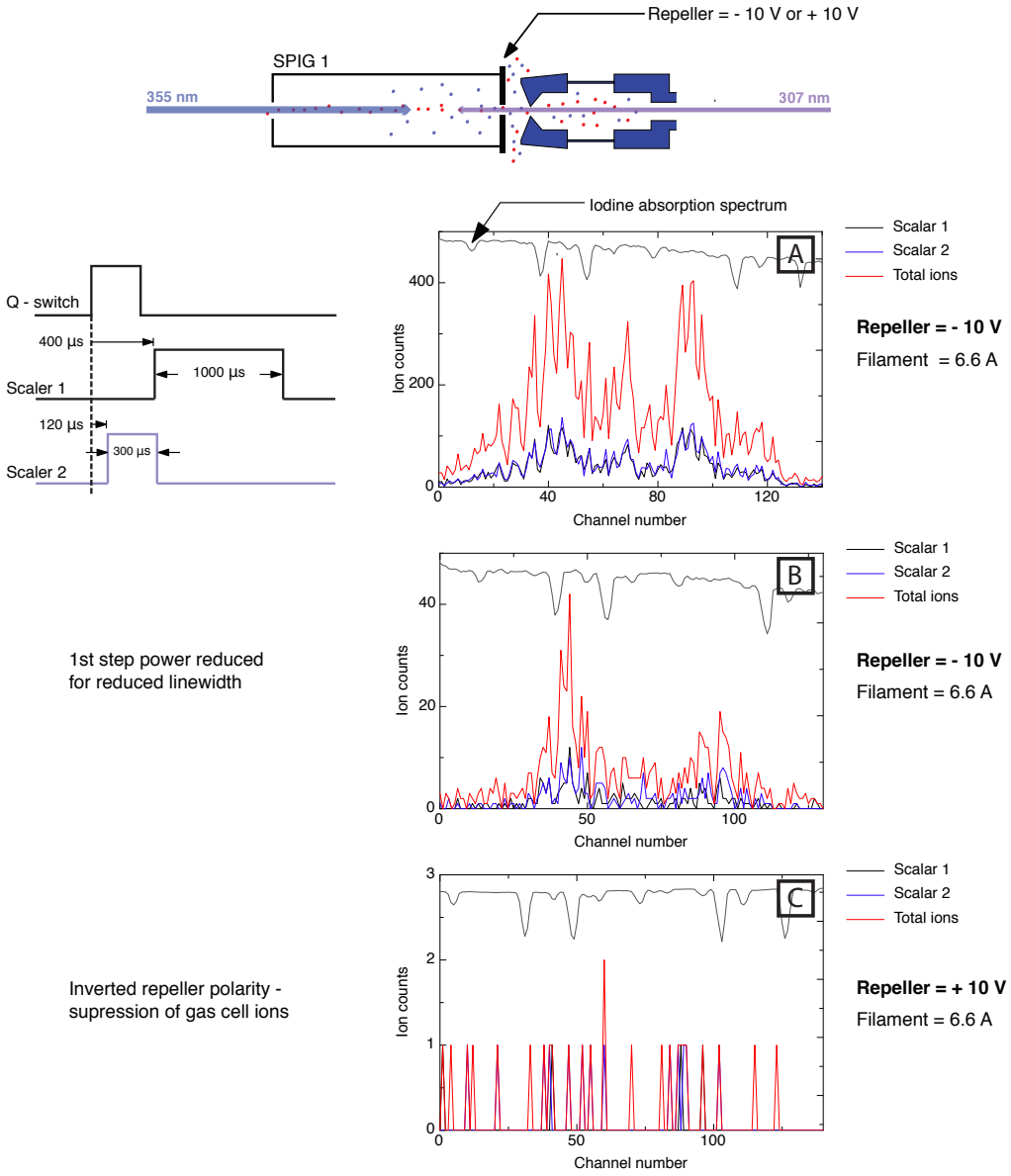

Figure 8.22: Bismuth ion spectra with the laser for the first-step focussed inside the gas cell. All ions are created inside the gas cell.

the gas cell or within the SPIG structure. This is desirable in order to make a direct comparison between the two ion signals whilst also providing good testing conditions for the suppression of gas-cell ions whilst extractions laser ions from the SPIG. During the test runs the insulator ring section of the SPIG enclosure, which is intended to seal the space between repeller electrode and the gas-cell nozzle, was not complete. As a consequence, the initial attempts to ionize Bi atoms outside the gas-cell were unsuccessful, most probably due to poor gas transmission to the SPIG.

To improve the gas transmission, the SPIG/gas-cell gap was sealed using insulating tape around the full circumference of the gas cell as illustrated in Figure 8.23.

Spectrum **A** in Figure 8.23 is very similar in terms of ion time distribution between the two scalars as seen in spectra **A** and **B** of Figure 8.22. In this case however, the ion signal remains unaffected when the repeller voltage polarity is reversed (spectrum **B**). This is attributed to the increased gas-jet density within the sealed section between the gas cell and the repeller. Suppression of the gas-cell ions required an increase in the repeller voltage to +100 V, as shown in spectrum **C** of Figure 8.23. With suppression of the gas-cell ions the delayed Bi^+ counts within scaler 1 (>400 μs) disappear, accompanied by a significant reduction in the prompt ion count rate within scaler 2 (<400 μs). Little difference can be seen between the ion spectrum from scaler 1 and the total ion signal, thus proving that all the ions are created within the SPIG and that all arrive at the detection point within the time window 120 - 420 μs after the trigger pulse. This is the first demonstration of RIS outside the gas cell at the IGISOL facility.

These results are confirmed in spectrum **D**, acquired after an optimization of the temporal overlap of the laser pulses for the two ionization steps, resulting in a balance of the relative intensities of the hyperfine components.

8.5 Conclusions

The gas flow study provided a valuable insight into the gas behaviour within one of the intended laser interaction regions for the FURIOS laser ion source. The confirmation of the observed gas-jet characteristics by measurements of particle

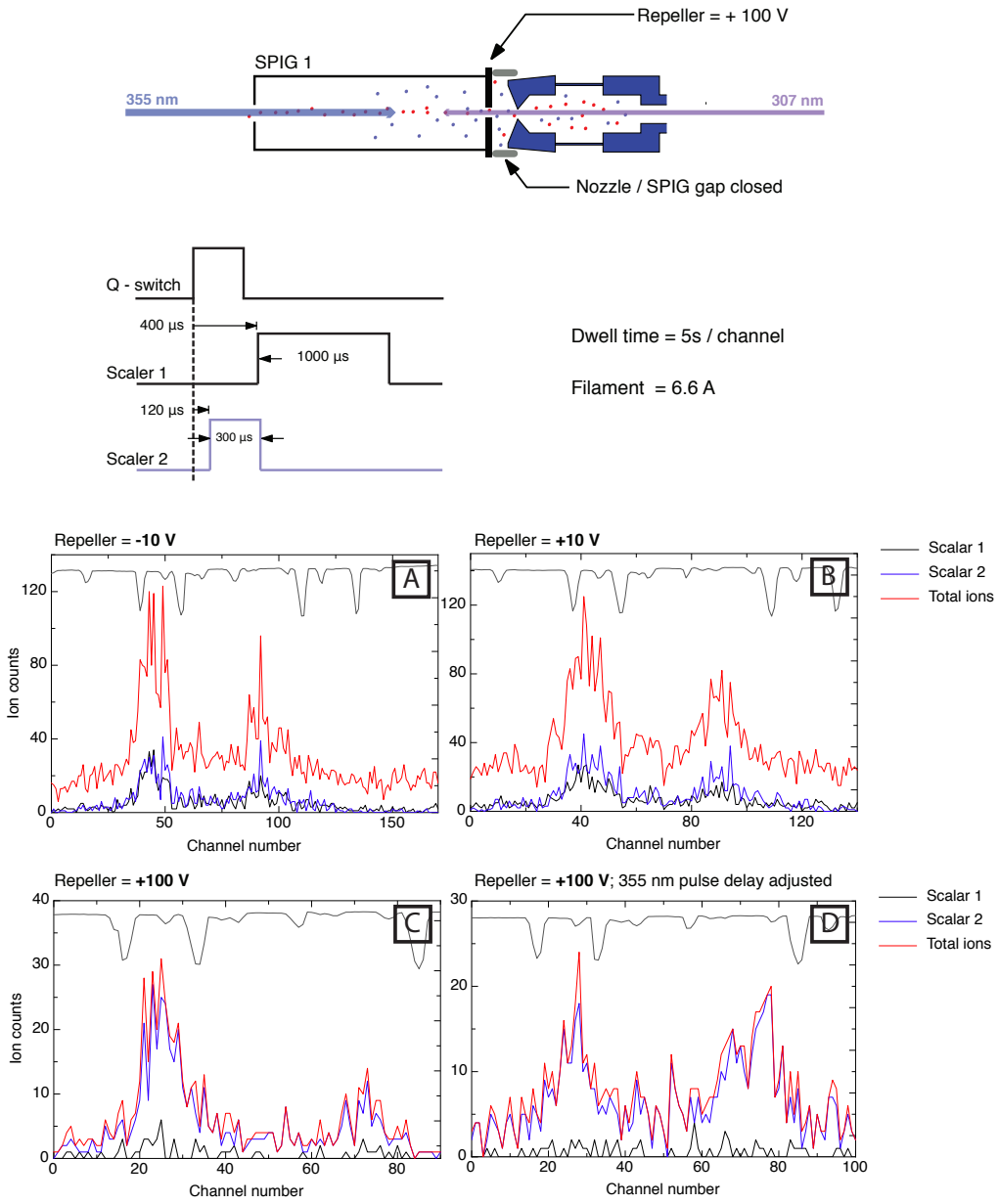

Figure 8.23: Bismuth ion spectra and time structure with all ions created inside the SPIG.

transport greatly enhances the confidence in the assessment of the gas flow dynamics and the worthiness of the suggested technical considerations for the SPIG device. The need for a region of high pressure surrounding the laser interaction region (the first SPIG section) has been directly demonstrated during the off-line Bi ionization test where the SPIG performance was greatly improved once a crude seal between the gas-cell nozzle and the SPIG enclosure was established.

The off-line SPIG tests showed promising results in terms of the ability to suppress ions emerging from the gas cell. During an on-line experiment, this will enable FURIOS to produce isobarically clean ion beams. For the bismuth tests carried out, the ionization efficiency within the SPIG is considerably lower than the 'gas-cell LIS' efficiency. To some extent this may be attributed to the poor gas-jet characteristics within the SPIG. Future tests with the completed SPIG incorporating a suitable seal of the SPIG/gas-cell gap would provide a more reliable comparison for use in estimating the FURIOS performance. It should be noted also that no off-line test can simulate conditions fully representative of on-line running. When the cyclotron beam is incident on a target within the gas cell, the conditions within the cell change dramatically on account of the inherent plasma. Additionally, it is expected that the relative SPIG/gas-cell ionization efficiencies will vary greatly from one element to the next on account of differences in chemical reactivity, ion survival and wall-sticking probability. A better reproduction of the time structure observations is therefore expected during on-line running and for some different elements.

8.6 Future work

Since these measurements, a new two step ionization scheme has been developed for bismuth for RIS using the high repetition rate Ti:Sa laser system. The new scheme compensates for the lower laser power per pulse compared with the 50 Hz system by employing a second excitation step to a high-lying Rydberg state. The spectra obtained were of sufficiently high resolution to resolve all six peaks in the HFS of ^{209}Bi. The gas-jet observation system has been transferred to a new off-line ion-guide setup capable of a closer replication of the IGISOL operating conditions with the intention of carrying out further gas-jet observation work

and jet-profile measurements using a needle-based beam scanner system. For ionization within the SPIG, improving the neutral fraction emerging from the gas cell and maintaining this fraction during on-line operation in the presence of the plasma induced by the driver beam.

References

[1] H. Geiger and E. Marsden. *Proceedings of the Royal Society*, A(82):495, 1909.

[2] E. Rutherford. *The L. E. D. Philosophical Magazine and Journal of Science*, 6(37):581, 1919.

[3] P. Dirac. *Quantum Mechanics*. Oxford, 3rd edition, 1947.

[4] J. Chadwick. *Proc. Roy. Soc.*, A(136), 1932.

[5] I. Curie and F. Joliot. *Compt. Rend.*, 198:254, 1934.

[6] V.N. Fedoseyev *et al. Hyp. Int.*, 127:409, 2000.

[7] J. Billowes and P. Campbell. *J. Phys. G*, 21:707, 1995.

[8] A .E . Barzakh *et al. Nucl. Inst. Meth. Phys. Res. B*, 69:517, 1992.

[9] V.N. Fedoseyev *et al. Nucl. Inst. Meth. Phys. Res. B*, 126:88, 1997.

[10] A. Mueller. An overview of radioactive beam facilities. *EPAC*, 2000.

[11] D. Morrissey and B. Sherrill. *Phil. Trans. R. Soc. London*, 356:1744, 1985.

[12] http://www.targisol.csic.es/, 2006.

[13] I. Langmuir and K. Kingdon. *Proc. Roy. Soc.*, 107:61, 1925.

[14] M. Saha. *Phil. Mag.*, 40:472, 1920.

[15] N. Stone *et al.* to be published.

[16] U. Köster. PhD thesis, Technischen Universität München, 1999.

[17] V.S. Letokhov. *Laser photoionization spectroscopy.* Academic Press, 1987.

[18] J. Äystö. *Nucl. Phys. A*, 693:477, 2001.

[19] J. Huikari. PhD thesis, The University of Jyväskylä, 2003.

[20] P. Kunz. *Eur. Phys. J. D*, 29:2, 2004.

[21] V. Letokhov *et al. Phys Rev. Lett.*, (59):1274, 1987.

[22] P. A. Franken. Phys. Rev. Lett., , 7:118, 1961.

[23] W. Silfvast. *Laser Fundamentals.* Cambridge, 2004.

[24] W.H. King. *Isotope Shifts in Atomic Spectra.* Plenum, 1984.

[25] K. Aufmuth, P. Heilig and A. Steudel. *At. Data Nucl. Data Tables*, 37(3):455, 1987.

[26] R.C. Barrett. *Rep. Prog. Phys.*, 37:1, 1974.

[27] C.W.E. van Eijk and F. Schutte. *Nucl. Phys.*, A151:459, 1970.

[28] A. Bohr and V.F. Weisskopf. *Phys. Rev.*, 77(1):94, 1950.

[29] S. Buttgenbach. *Hyp. Int.*, 20:1, 1984.

[30] V.N. Fedosseev *et al. Nuc. Inst. Meths. Phys. Res. B*, 204:353, 2003.

[31] D. Grancharova and E. Chevallay. *Proc. Conf. Balkan Physical Union*, 2003.

[32] T. Hänsch. *Appl. Opt*, 11:895, 1972.

[33] P. Dyer *et al. J. App. Phys.*, 58:2431, 1983.

[34] V. I. *et al* Mishin. *Opt. Comms.*, 61(61):383, 1987.

[35] K. Blaum *et al. Phys Rev. Lett.*, 92:11, 2004.

[36] D. Habs *et al. Z. Physik A*, 358:2, 1997.

[37] U. Köster. *Radiochim. Acta*, 89:77777, 2001.

[38] K. Kratz. *Z. Phys A.*, 325:489, 1986.

[39] Y. Jading *et al. Nuc. Inst. Meths. Phys. Res. B*, 76:126, 1997.

[40] http://cfa-www.harvard.edu/amdata/ampdata/kurucz23/sekur.html, 1995.

[41] E. Saloman. *Spectrochimica Acta B*, 45:37, 1990.

[42] E. Saloman. *Spectrochimica Acta B*, 47:517, 1992.

[43] L. Beaty H. Loock and B. Simard. *Phy. Rev. A*, 59:873, 1999.

[44] U. Krönert *et al. Appl. Phys. A*, 44:339, 1987.

[45] W. Zhao *et al. App. Phys. B*, 52:299, 1991.

[46] O. Reshetnikova and E. Skorohod. *Optics and Spectroscopy*, 87, 1999.

[47] I. D. Moore *et al. Hyperfine Interactions*, to be published.

[48] R. Neugart. *Eur. Phys. J. A*, 15:35, 2002.

[49] J. Lee *et al. Nuc. Inst. Meths. Phys. Res. B*, 34:252, 1988.

[50] U. Krönert *et al. Nucl. Inst. Meth. Phys. Res. A*, 300:522, 1991.

[51] U. Köster and V. N Fedoseyev. *Hyperfine Interactions*, (127):417, 2000.

[52] A. Barzakh *et al. Nuc. Inst. Meths. Phys. Res. B*, 69:517, 1992.

[53] R. Kirchner. *Nucl. Instr. Meth. B*, 70:186–199, 1992.

[54] V Mishin *et al. Nucl. Instr. Meth. B*, 73(550), 1993.

[55] Y. Jading *et al. Nucl. Instr. Meth. B*, 126:76, 1997.

[56] V. Sebastian *et al. ENA98*, page 126.

[57] T. Kautzsch *et al. Phys. Rev. C*, 54:R2811–R2814, 1996.

[58] R. B. Firestone and V. S. Shirley. *Table of Isotopes*, volume II. John Wiley & Sons, eighth edition, 1996.

[59] CERN Program Library MINIM / MINUIT.

[60] N. J. Stone. At. Data Nucl. Data Tables , 90:75, 2005.

[61] A. Andreyev *et al. Proposal to the INTC*, (INTC-P-151), 2002.

[62] B.S. Reehal and R.A Sorensen. *Nucl. Phys. A,* , 161:385, 1971.

[63] I. Talmi. *Nucl. Phys. A,* , 423:189, 1984.

[64] A. Andreyev *et al. Eur. Phys. J. A*, 14:63, 2002.

[65] A. Andreyev *et al. Phys. Rev. C*, 66, 2002.

[66] A. Andreyev *et al. Nature*, 405:430, 2000.

[67] H. De Witte. PhD thesis, IKS, KULeuven, 2004.

[68] M. Pearson. *J. Phys. G: Nucl. Part. Phys.*, 26:1829, 2000.

[69] ROOT. An object orientated data analysis framework. *Linux Journal*, 51, 1998.

[70] J. Van Roosbroeck. PhD thesis, University of Leuven, 2002.

[71] L. Weissman *et al. Phys. Rev C*, 65, 2002.

[72] M. Seliverstov. Private communication. 2006.

[73] P. Campbell *et al. Phys. Lett. B.*, 346:21, 1995.

[74] R. Title and K. Smith. *Phil. Mag.*, 5:1281, 1960.

[75] P. Raghavan. *At. Data Nucl. Data Tables*, 42:189, 1989.

[76] S. Alpert *et al. Phy. Rev.*, 125:256, 1962.

[77] W. D. Myers and K. H. Schmidt. *Nucl. Phys. A*, 410:61, 1983.

[78] O. Häusser *et al. Hyp. Int.*, page 196, 2005.

[79] A. Bohr and B. R. Mottelson. *Nuclear Structure*, volume II. World Scientific Publishing, 1998.

[80] C. Ekström *et al. Hyperfine Interactions*, 1:437, 1976.

[81] R. Neugart. *Phys. Rev. Lett.*, 55:15, 1985.

[82] A. Arima *et al. Mesons in nuclei.* Rho and Wilkinson, 1979.

[83] W.D. Myers and K.H Schmidt. *Nucl. Phys.*, A410:61, 1983.

[84] M. Bender. *Phys. Rev C*, 69(064303), 2004.

[85] V. Hellemans *et al. Phys. Rev. C*, 71(034308), 2005.

[86] A. Arima and F. Iachello. *The interacting boson model.* Cambridge University Press, 1987.

[87] R. K. Yoo *et al. J. Phys. B*, 28:1743, 1995.

[88] R. Wood *et al. Phys Rev. Lett.*, 79:1571, 1997.

[89] Y. Kudryavtsev *et al. Nuc. Inst. Meths. Phys. Res. B*, 114:350, 1996.

[90] I. D. Moore *et al. J. Phys. G: Nucl. Part. Phys.*, 31:1499, 2005.

[91] J. Äystö. *Nucl. Phys. A*, 693:477, 2001.

[92] I.D. Moore. PhD thesis, Department of Physics and Astronomy,University of Manchester, 2001.

[93] P. Campbell. PhD thesis, Department of Physics and Astronomy, University of Manchester, 1994.

[94] K. Blaum *et al. Nucl. Inst. Meth. Phys. Res. B*, 204:331, 2003.

[95] K. Wies *et al. Hyp. Int.*, 162:1, 2005.

[96] A. Nieminen *et al. Nucl. Instrum. Methods A*, 469:244, 2001.

[97] K. Flanagan. PhD thesis, Department of Physics and Astronomy, University of Manchester, 2004.

[98] R. Macfarlane and R. Griffioen. *Nucl. Inst. Meth.*, 24:461, 1963.

[99] K. Valli and E. Hyde. *Nucl. Inst. Meth.*, 179:533, 1981.

[100] K. Peräjärvi. PhD thesis, , March 2001.

[101] M. Rasi *et al. Nucl. Inst. Meth.*, 378:251, 1996.

[102] F. Sherman H. Ashkenas. *Rarefied gas dynamics*, volume 2. Academic Press, New York, 1966.

[103] A. Popov. Private communication. 2005.